

ABSTRACT

Title of dissertation: Physics of Breaking Bow Waves: A
Parametric Investigation using a 2D+T
Wave Maker

Eric Maxeiner, Doctor of Philosophy, 2009

Dissertation directed by: Professor James H. Duncan
Department of Mechanical Engineering

A mechanical 2-dimensional wave maker with a flexible surface was used to create waves similar to those formed at the bow of a moving ship. Utilizing the 2D+T approximation, the wave maker was programmed so that its deformable wave board creates a time sequence of shapes that simulate the line of intersection between one side of the hull of a slender ship model moving at constant speed and an imaginary vertical plane oriented normal to the ship model track. Instead of trying to simulate a particular ship hull, however, the wave maker simulates a parametric set of flat plate motions that contain components of typical bow shapes. The resulting surface waves were measured using a cinematic laser-induced fluorescence technique and the resulting wave profiles were analyzed. A tremendous variation of wave shapes was observed. A variety of wave characteristics including the peak contact point height, peak wave height, wave crest speed and plunging jet thickness distribution were measured and related to the corresponding wave maker motion parameters. Despite the complexity of the wave maker motions, it was observed that wave maker ve-

locity and acceleration along the water line were the wave maker parameters with the strongest influence on many of the measured wave characteristics. Additional analysis reveals that the initial acceleration of the wave maker affects some wave characteristics, especially those related to plunging jet behavior, but does not significantly affect the overall size and shape of the wave. It was also observed that the behavior of wave formation and breaking ranged between two distinct modes. The first mode consists of an overdriven wave that contains a pronounced vertical jet along the face of the wave maker. The overdriven wave breaks close to the wave maker, before a wave crest has fully formed. The second mode is a more slowly developing wave that breaks further away from the wave maker. The developing waves do not contain the pronounced vertical jet observed in overdriven waves. The two modes appear to be related to the initial wave maker acceleration and amount of water displaced by the wave maker.

Physics of Breaking Bow Waves: A Parametric Investigation Using a
2D+T Wavemaker

by

Eric Maxeiner

Dissertation submitted to the Faculty of the Graduate School of the
University of Maryland, College Park in partial fulfillment
of the requirements for the degree of
Doctor of Philosophy
2009

Advisory Committee:
Professor James H. Duncan, Chair/Advisor
Professor Elias Balaras
Professor Richard Calabrese
Professor William Fourney
Professor Kenneth Kiger
Dr. Thomas Fu

Acknowledgments

I would like to thank my primary colleague, Dr. Mostafa Shakeri, who was instrumental in making the 2D+T wave maker a reality and provided invaluable guidance and assistance.

I would like to thank the rest of my lab colleagues: Jamie Diorio, Mohammad Tavakolinejad, Dr. Xinan Liu, and Christine Ikeda. Every successful lab requires cooperation amongst its members, regardless of how inter-related their research is. It has been a lot of fun working with you.

I would like to thank my parents for always believing in me and not questioning (too much) why I would give up a comfortable and well-paying job with the Navy to be poor and stressed-out for three years.

I would like to thank my girlfriend Bree for being very patient and understanding throughout this whole process. Now we can get a dog.

And finally, I would like to thank my advisor, Dr. James Duncan, for his guidance and friendship throughout my doctoral studies. He always offered good advice, wouldn't let me produce any work that wasn't excellent and gave me the space to make this project truly my own. I am deeply indebted to him for being able to reach this point.

Table of Contents

List of Tables	v
List of Figures	vi
List of Abbreviations	xii
1 Introduction	1
1.1 Motivation	1
1.2 Historical Perspective	1
1.3 Wave Research	4
1.4 Plunging Jet Characteristics	6
1.5 2D+T Approximation	8
1.6 Thesis Outline	12
2 Experimental Details	14
2.1 Test Facilities	14
2.1.1 Wave Tank	14
2.1.2 Wave Maker	14
2.1.3 Wave Maker Motion Categories	19
2.1.4 Wave Measurements	24
2.2 Image Processing	26
2.3 Post-Processing	27
2.4 Repeatability	27
3 Wave Results	30
3.1 General Observations	30
3.2 Contact Points	31
3.3 Time to Peak Contact Point Height	36
3.4 Peak Surface Height	43
3.4.1 Wave Crest Speed	46
3.5 Breaking Characteristics	47
3.5.1 Breaker Type	47
3.5.2 Breaking Onset	49
3.5.3 Jet Impact Point Location	50
3.6 Effect of Wave Board Acceleration	51
3.7 Breaker Variability	55
4 Plunging Jet Characteristics	61
4.1 Plunging Wave Shape	61
4.2 Jet Tip Trajectory	65

5	Jet Thickness Measurements	70
5.1	Measurement Techniques	70
5.2	Thickness Results	77
5.3	Relations with Wave Maker Parameters	77
5.4	Comparison with Other 2D+T Waves	82
5.5	Comparison with Shoaling Waves	82
5.6	Relationship with Jet Tip Acceleration	85
5.7	Sheet Tapering	85
5.8	Sheet Instability	87
6	Breaking Modes	93
6.1	Observation of Breaking Modes	93
6.2	Mechanics of Breaking Modes	96
6.3	Identification of Breaking Mode	102
6.4	Role of Breaking Mode in Wave Variability	104
7	Conclusions	106
7.1	Summary	106
7.2	Applications and Future Work	107
A	Matlab Codes	110
A.1	Edge Detection	110
A.2	Inverse Transformation	116
A.3	Jet Thickness Calculation	121
B	Spreadsheets	130
B.1	Wave Maker Parameters	130
B.2	Data for Plots	132
C	Wave Profiles	135
C.1	All Profiles	135
D	Fixed Case Comparison	151
	Bibliography	153

List of Tables

2.1	Table of wave maker characteristics for the five categories of wave maker motions, including the range of run times (t_{wm}) and wave board speeds (V_b). B_k and B_w refer to bottom (keel elevation) translation and waterline translation of the wave board, respectively	23
3.1	Equivalent values of φ , as defined in Delhommeau et al. (2009), for wave maker motion categories in the present study.	42
3.2	Table of wave board speeds, and corresponding wave board accelerations, at which breaking onset occurs.	49
4.1	Table of plunging slope values. Slopes >1 indicate a steeper jet while slopes <1 indicate a flatter jet.	65

List of Figures

1.1	Kelvin wave pattern (as drawn by William Froude).	3
1.2	Bow wave characteristics for various model ship hulls and as predicted using thin-ship theory (from Noblesse 2006). Bow wave height, Z_b , is shown in (a) for nine ship hulls and a theoretical line of $2.2/(1 + F_T)$, with F_T being draft Froude number. Hull entrance angle is denoted by α_E . Longitudinal location of bow wave peak, X_b , is shown in (b) for five ship hulls and a theoretical line of $1.1/(1 + F_T)$	6
1.3	Fit of $\sqrt{3} : 1$ aspect-ratio ellipse to observed profiles of plunging breakers (from Bonmarin, 1989)	7
1.4	Comparison of 2-D wave profiles with a 3-D wave. (a) 3-D representation a spilling dispersively focused breaker using 2-D wave profiles (from Duncan et al. 1999) compiled according to 2D+T technique. (b) Overhead view of model test bow wave (from Dong 1997).	10
1.5	3-D representation of a plunging bow wave created by a 2D+T wave maker (from Shakeri, 2009a). Profiles compiled by offsetting each 2-D surface profile by a fixed distance along the vertical axis.	11
1.6	Contact line and wave profile measurements of R/V Athena hull using 2D+T wave maker (lines without data points) as compared with 3-D tank data (lines with data points). From Shakeri (2009b).	12
2.1	Schematic representation of the wave tank at the University of Maryland Hydrodynamics Lab.	15
2.2	Overview of 2D+T experimental procedure. The initial position of the wave board simulates the bow of the ship being lined up with the 2-D plane of the wave maker. The extended position simulates the ship having moved forward a given amount and thus displacing the water with the corresponding hull shape for that position.	16
2.3	(a) Position histories for all four wave maker channels for a typical wave maker profile. Channel positions are the horizontal distance from starting position (vertical wave board). The solid lines indicate the actual profiles and the dashed lines indicate the idealized (infinite acceleration) profiles. (b) Close-up view of a typical initial acceleration for one of the channels.	18

2.4	Profiles of acceleration (a) and velocity (b) for a single wave maker channel (i.e. drive piston) during a typical wave case, with time normalized by run time.	19
2.5	Graphical representations of the wave maker motion categories used in this study.	20
2.6	Equivalent 3-D hull shapes for wave maker motion categories (a) Slap, (b) Full and (c) Fixed, $\alpha = 30^\circ$	22
2.7	Details of optical setup. Longitudinal view (looking down the tank) is shown on the left and an overhead view is shown on the right. . . .	25
2.8	Images of the calibration board (left) and an actual test wave (right). Both images are taken from same camera position and orientation with respect to the tank.	27
2.9	Various features of a typical wave image (Slap, $V_b = 0.98$ m/s).	28
2.10	Water surface profiles taken at 1/16 second intervals for Slap case, $V_b = 0.98$ m/s. The different colors (blue and red) indicate profiles taken from different measurement zones.	29
2.11	Water surface profiles taken 1/16 second intervals from three success of runs (shown as different colors) of the same wave maker motion (Slap, $V_b = 0.87$ m/s).	29
3.1	Time series of a typical wave profile (Slap, $V_b = 0.8$ m/s, $t_{wm} = 0.66$ s). The figures in the left-hand column are unprocessed images from the high-speed movies and the figures on the right are corresponding surface profiles.	33
3.2	Wave images taken at the moment of plunging jet impact. All cases run at approximately the same wave board speed ($0.94 \leq V_b \leq 0.98$ m/s)	34
3.3	Plots of contact point height (normalized by draft) versus time: (a) Slap, (b) Mix 0.2, (c) Mix 0.4, (d) Full, (e) Fixed, $\alpha = 15^\circ$, (f) Fixed, $\alpha = 30^\circ$	37
3.4	Plots of fully normalized contact point height versus non-dimensional time: (a) Slap, (b) Mix 0.2, (c) Mix 0.4, (d) Full, (e) Fixed, $\alpha = 15^\circ$, (f) Fixed, $\alpha = 30^\circ$	38
3.5	Non-dimensional maximum contact heights for various wave maker profiles.	39

3.6	Time to peak contact point, t_{cp} , versus F_b	40
3.7	Equivalent time to peak contact point height versus Froude number using thin-ship theory for three values of φ (from Delhommeau 2009). F_d is the Froude number based on forward hull speed and hull draft. Values of 1.0, 0.5 and 0.0 approximately correspond to Slap, Mix 0.2 and Fixed cases, respectively	43
3.8	Non-dimensional maximum surface heights for various wave maker profiles plotted against F_b	44
3.9	Froude-normalized time histories of peak surface height for various wave maker profiles, all at approximately $V_b = 0.98$ m/s. For clarity, all rotating cases are shown in (a) and Fixed, Slap and Full cases are shown in (b).	46
3.10	Normalized wave crest speed versus F_b for all wave maker motion categories. Data from 5415 hull form tests (Shakeri et al. 2009a) is included.	47
3.11	Non-dimensional peak crest heights for all profiles, identified by breaker type.	48
3.12	Horizontal jet impact point location (Y_{impact}) versus F_b	51
3.13	Normalized horizontal jet impact location (Y_{impact}/B_w) versus (a) F_b and (b) a_b/g	52
3.14	Wave profiles resulting for Mix 0.2, $V_b = 0.94$ m/s run with three different acceleration schemes. High acceleration uses $T_R = 0.4$, normal acceleration uses the standard $T_R = 0.5$ and the low acceleration uses $T_R = 0.6$. Profiles are plotted at the same 1/16 second intervals.	54
3.15	Effect of wave board acceleration for Mix 0.2, $V_b = 0.94$ m/s. (a) Non-dimensional contact point heights plotted versus normalized time and (b) normalized peak wave height trajectory.	54
3.16	Peak contact point heights versus normalized wave board acceleration for cases with varied wave board acceleration parameters.	55
3.17	Time to peak contact point versus normalized wave board acceleration for cases with varied wave board acceleration parameters.	56
3.18	Horizontal location of jet impact point versus normalized wave board acceleration for cases with varied wave board acceleration parameters.	57

3.19	Wave images of two separate runs of Full, $V_b = 0.98$ m/s. Run 1 results in a plunging breaker whereas Run 2 in a spilling breaker, even though both runs have identical wave maker motions.	59
3.20	Wave profiles from three separate runs (shown as different colors) of Full, $V_b = 0.98$ m/s. One run (blue) develops a plunging breaker while the other two runs (green and red) develop spilling breakers. . .	60
4.1	Measured geometric characteristics of a plunging breaker.	62
4.2	Plunging length versus wave board Froude number.	62
4.3	Plunging length versus wave board acceleration.	63
4.4	Plunging length versus wave board acceleration for varied acceleration cases.	63
4.5	Plunging slope versus wave board acceleration.	64
4.6	Jet tip tracking for two Slap cases, $V_b = 0.98$ m/s and 0.87 m/s. The symbols represent measured jet tip locations and the solid lines are second order curve fits.	66
4.7	Average jet tip vertical acceleration (normalized by gravity) versus wave board Froude number.	67
4.8	Average horizontal jet tip velocity versus wave board Froude number.	68
4.9	Average horizontal jet tip velocity minus crest speed versus wave board Froude number.	69
5.1	Example application of Snell's law of refraction to measure the thickness of a 2-dimensional slab of transparent material. Locations of Z_0 and Z_1 can be measured from the camera image and used to calculate the location of Z_2	71
5.2	Representation of refraction through a cylinder. A ray of light (yellow line) originates at a point on the inside edge (P_{in}), refracts as it passes through a point on the outside edge (P_{out}) and continues to the camera.	73
5.3	Glass cylinder setups used for development and validation of jet thickness measurement techniques.	75

5.4	Cylinder thickness results for (a) table setup, 0.25 inch wall thickness and (b) in-tank setup, 0.50 inch wall thickness. The upper plots show the measured and calculated edge locations and the bottom row shows the calculated thickness values. Red dashed line on thickness plots indicates the known thickness of the cylinder. The x and y coordinates are with respect to an arbitrary origin.	76
5.5	Wave thickness measurements results for two cases: (a) Full, $V_b = 1.05$ m/s and (b) Fixed, 30° , $V_b = 0.94$ m/s. The upper plots show the measured and calculated edge locations and the bottom row shows the calculated thickness values. The x and y coordinates are with respect to the test origin.	78
5.6	Average jet thickness versus wave board Froude number.	80
5.7	Average jet thickness versus wave board acceleration.	80
5.8	Average jet thickness versus wave board acceleration. Note: (*) indicates cases with varied wave board accelerations.	81
5.9	Average jet thickness versus wave board acceleration, including data from 5415 hull wave maker motion.	83
5.10	Comparison of jet thickness calculations for (a) shoaling wave (from Miller 1976) and (b) the present study (Full, $V_b = 1.05$ m/s). The x and y coordinates are with respect to an arbitrary origin for (a) and to the test origin for (b).	84
5.11	Average vertical jet tip acceleration versus average jet thickness.	86
5.12	Thickness profiles for Slap ($V_b = 0.98$ m/s), Full ($V_b = 1.05$ m/s) and Fixed ($V_b = 0.94$ m/s) compared with corresponding vertical falling sheet (dashed lines of same color). For the 2D+T wave curves, the vertical distance is taken as the vertical coordinate of the bottom edge of the jet.	88
5.13	Wave images at moment of jet impact for waves analyzed in Figure 5.12. (a) Slap ($V_b = 0.98$ m/s), (b) Full ($V_b = 1.05$ m/s) and (c) Fixed ($V_b = 0.94$ m/s).	89
5.14	Wave image of Fixed case (30° , $F_b=0.317$) showing transverse striations.	91
5.15	Sketch of (a) symmetric and (b) antisymmetric waves on a sheet of thin fluid (from Taylor, 1959).	91

6.1	Contour plots of water surface: (a) Slap, $V_b = 0.98$ m/s, (b) Full, $V_b = 0.98$ m/s. Contour lines are in units of cm (vertical elevation). Solid white line represents the transverse location of the contact point and the yellow dashed line represents the location of the waterline translation of the wave maker. The vertical axis has been transformed into a dimensional value by using an arbitrary forward velocity of 100 in/s (recall: $x = x_0 + Ut$).	97
6.2	Illustration of breaking modes: (a) overdriven (Slap, $V_b = 0.94$ m/s) and (b) developing (Full, $V_b = 0.98$ m/s). $t^* = t/t_{wm}$. Red arrows indicate dominant flow directions.	98
6.3	Surface profiles of a dispersively focused plunging breaker at intervals of ≈ 0.04 seconds (taken from Bonmarin 1989)	100
6.4	Illustration of overdriven breaking mode with Fixed, 30° ($V_b = 0.97$ m/s). $t^* = t/t_{wm}$	101
6.5	Illustration of breaking modes with mix cases: (a) Mix 0.2, overdriven ($V_b = 0.99$ m/s) and (b) Mix 0.4, developing ($V_b = 0.97$ m/s). $t^* = t/t_{wm}$	103
6.6	Back drop ($\frac{Z_p - Z_c}{Z_p}$) versus vertical jet slope.	104
D.1	Comparison of Fixed cases at different angles of attack. Both cases tested at $V_b = 0.94$ m/s ($t_{wm} = 0.65$ s).	152

List of Abbreviations

a_b	average wave board acceleration
a_j	plunging jet tip vertical acceleration
B_w	horizontal wave maker translation distance along static waterline
B_k	horizontal wave maker translation distance along keel elevation
d	wave maker keel depth (equivalent to model draft)
F_b	wave board Froude number, $\frac{V_b}{\sqrt{gd}}$
h	sheet thickness
t_{wm}	wave maker run time
t_{cp}	time to peal contact point height
T_R	rounding period, as portion of t_{wm} , used for wave maker acceleration
t^*	normalized time, t/t_{wm}
V_b	wave board speed
V_{crest}	wave crest speed
V_{jet}	horizontal velocity of the plunging jet tip
Y_{impact}	horizontal location of plunging jet impact point
Z_c	height of contact point
Z_p	peak surface height of a given surface profile, excluding splash
α	angle of attack (degrees) for Fixed cases
α_0	initial angle of wave board (prior to motion)
α_{end}	final angle of wave board (after completion of motion)
φ	non-dimensional bow shape factor used in Delhommeau et al. (2009)
θ_i	angle of incidence (used for refraction calculations)

Chapter 1

Introduction

1.1 Motivation

Breaking bow waves are important to engineers for many reasons. For ship designers, bow waves are a major source of resistance and the breaking induces splashing and entrains air bubbles, resulting in a white-water wake. This wake can be a significant source of radar signature for naval craft (Peltzer 1984). The air bubbles also create noise in the water which is detectable using underwater acoustics. Current ships are designed to have such low radar, infra-red and acoustic signatures that the breaking waves are often more detectable than the ship itself. Ship waves are also a persistent problem for harbors and near-shore ferries as significant damage can be produced by large, steep waves. Additionally, the breaking mechanisms in bow waves may occur other types of waves, such as shoaling waves. This study seeks to investigate the mechanics of breaking bow waves to better understand the relationship between bow shape and the behavior of the resulting wave.

1.2 Historical Perspective

Ship design is a discipline with thousands of years of history and tradition. Despite this, it has only been in the last 150 years, beginning with William Froude's

monumental work in the 1860's, that ship hydrodynamics have been properly studied. This is not to say ships were crudely designed up until this point. Throughout the history of mankind, boats and ships have been used for vital tasks such as fishing, military operations, and transportation of both people and cargo. Ships must also perform these tasks in an extremely harsh and unforgiving environment. If people are given thousands of years of trial and error under such pressure, it should be fully expected that highly optimized designs will be produced. As a result, ship designs have been refined, vast armadas have shaped political history, large populations have been sustained and moved across oceans, and unknown continents were discovered long before any one ever heard of a Froude number.

For a ship to move forward, it must move considerable amounts of water out of its way. This may come from pushing the water below it or around it. A submarine is able to push this water all around its hull and does not have to contend with the free surface. Typical displacement ships, on the other hand, must push most of the water to the sides and thus generate surface waves.

The two primary components of ship resistance are friction and wavemaking, which can be thought of as shear and normal forces. Friction results from the development of a viscous boundary layer around the hull and can successfully be modeled as flow over a flat plate with area equal to that of the ship's wetted surface. Wave-making resistance results primarily from the pressure the water exerts on the hull as the ship tries to push it aside. These waves transport energy away from the ship (i.e. energy loss). William Froude was the first to appreciate the separate components of ship resistance and thus advocated the use of towing tanks to determine the resis-

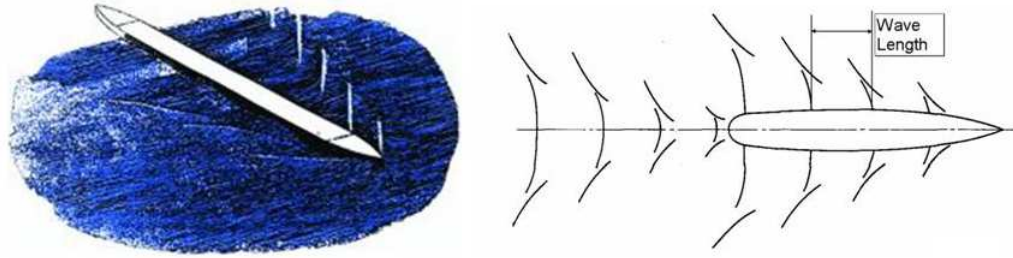


Figure 1.1: Kelvin wave pattern (as drawn by William Froude).

tance of ships. Froude's innovations roughly coincided with the fundamental studies of linear and nonlinear water waves by Stokes (1847), only a decade earlier. In 1887, Lord Kelvin (William Thomson) derived the pattern of waves created by a moving infinitesimal disturbance, known as the Kelvin wave pattern, shown in Figure 1.1. The Kelvin wave pattern is comprised of divergent (roughly perpendicular to direction of motion) and transverse (following the motion) waves. A decade later, J.H. Michell (1898) developed the first analytical expression for wave resistance using a technique commonly known as thin-ship theory. This technique models the ship as a straight line of pressure sources moving through a calm, inviscid fluid. Additional developments by Stokes, Osborne Reynolds and Lord Rayleigh in the 1870's more or less completed the basic linear theory of ship waves that is still used today. Comprehensive reviews of the various techniques used for estimating ship resistance, particularly wavemaking resistance, can be found in Wehausen (1973) and Larsson & Baba (1996).

Wave breaking has been a particularly difficult phenomenon to model because this flow is nonlinear, turbulent and contains both air and water. The advent of

computers in the mid to late 1900s allowed for the development of computational fluid dynamics and the ability to simulate waves numerically. At the same time, more powerful experimental methods were appearing such as PIV (Particle Image Velocimetry) and high-speed photography, among many others. As a result, scientists have become better equipped to deal with the problem of nonlinearity in the past 30 years and there has been renewed interest in waves breaking.

1.3 Wave Research

Wave research has benefited from well-developed potential flow theories. Wave breaking, however, is a highly complex fluid motion that cannot be adequately modeled with potential flow. There are no analytical theories available to describe the flow and thus researchers have typically resorted to numerical methods (see Chan & Street 1970, Longuet-Higgins and Cokelet 1976, New et al. 1985 and Dommermuth et al. 1988).

While most experimental work on wave breaking has focused on spilling waves (see Duncan 1981 & 1983, Battjes and Sakai 1981 and Lin & Rockwell 1994 & 1995), there have been several studies addressing plunging breakers. An experimental study was conducted by Skyner et al. (1990) in which the flow field of a plunging breaker was measured using PIV and results were compared to a fully non-linear time-stepping model. Overall comparison between the model and experiments was found to be good except for the detail around the jet tip and the timing of the jet formation and breaking. Bonmarin (1989) performed a comprehensive study of the geometry

of deep-water breaking waves using dispersively focused waves. Both spilling and plunging waves were considered and particular attention was paid to the shape evolution and the splash behavior. Rapp & Melville (1990) investigated details of the dynamics of turbulent breakers mechanically generated in deep water. They measured several effects of breaking events such as the loss of excess momentum flux and the production of surface currents. The results show a loss of momentum flux of 10% for spilling breakers and 25% for plunging breakers.

A number of experimental studies on bow waves have been performed at the towing tanks of David Taylor Model Basin (see Dong et al. 1997 and Roth et al. 1999) and the Tokyo University Tank (see Inui 1981 and Miyata & Inui 1984). These studies have often employed surface visualization techniques (aluminum powder and tracer particles) to characterize wave structures and flow features.

Waniewski et al. (1997, 2001 & 2002) simulated a bow wave by placing a deflecting plate in a supercritical free-surface shallow water flume. Surface profiles of the resulting waves were measured and used to investigate scaling and dependence on geometric parameters. In general, the various profiles, regardless of model scale, were similar near the leading edge of the plate but deviate significantly thereafter.

A series of papers by Noblesse et al. (2006 & 2008) and Delhommeau et al. (2009) have attempted to approximate bow wave characteristics using thin-ship theory. Using simple analytical expressions and focusing primarily on entrance angle and ship Froude number for wedge-shaped hulls, a number of simple relations were developed to calculate the height, location and steepness of bow waves. For these studies, the bow wave is defined as the shape of the contact line along the

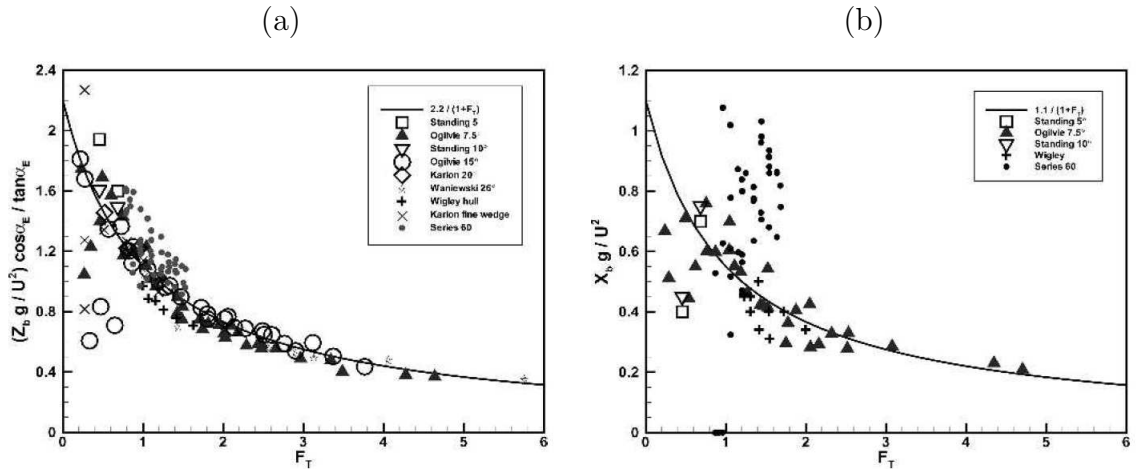


Figure 1.2: Bow wave characteristics for various model ship hulls and as predicted using thin-ship theory (from Noblesse 2006). Bow wave height, Z_b , is shown in (a) for nine ship hulls and a theoretical line of $2.2/(1 + F_T)$, with F_T being draft Froude number. Hull entrance angle is denoted by α_E . Longitudinal location of bow wave peak, X_b , is shown in (b) for five ship hulls and a theoretical line of $1.1/(1 + F_T)$.

hull and does not examine wave characteristics away from the hull. Semi-empirical expressions based solely on Froude number reasonably predict bow wave heights but are less successful in predicting the location of the wave peak (Figure 1.2).

1.4 Plunging Jet Characteristics

The shape and trajectory of a plunging breaker has only been studied occasionally and studies that have done so have typically examined jets of freely propagating breaking waves rather than breaking bow waves. New (1983) examined numerically generated plunging breakers and identified the shape of the cavity to be remarkably well approximated by a $\sqrt{3} : 1$ aspect-ratio ellipse. This study also included a fit to

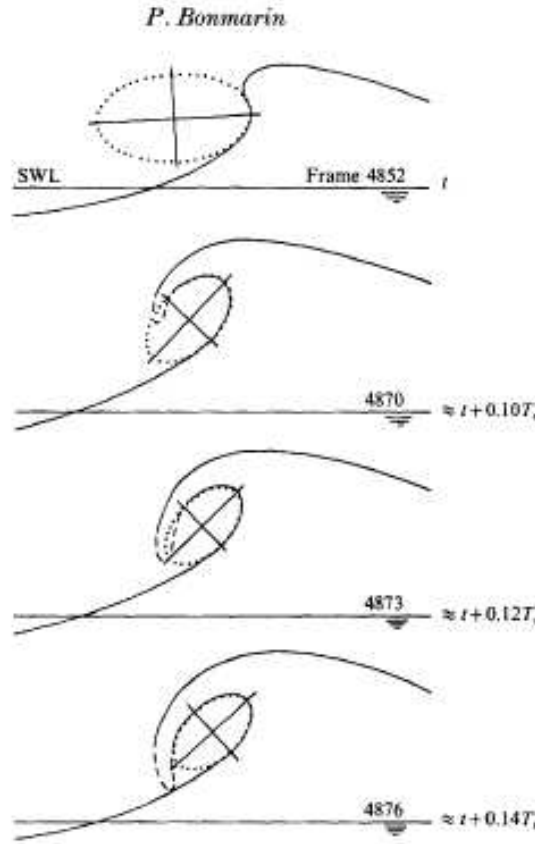


Figure 1.3: Fit of $\sqrt{3} : 1$ aspect-ratio ellipse to observed profiles of plunging breakers (from Bonmarin, 1989)

plunging breakers generated in shallow water from Miller (1976). Bonmarin (1989) confirmed this geometric feature using a set of dispersively focused plunging breakers (Figure 1.3). In all studies, the orientation, location and scale of the ellipse were arbitrarily fitted to the wave i.e. after the wave shape was known. Nonetheless, the finding suggests an intriguing self-similarity.

The initial stages of jet development were examined by King and Needham (1994) by modeling the flow field induced by a vertical plate accelerating through

a stationary fluid free surface. Using a rigorous mathematical analysis, a solution is obtained containing a vertical jet at the intersection of the plate and the free surface. The results were consistent with observations.

Several authors have examined the breakup of the jet in plunging breakers. Longuet-Higgins (1995) proposed an inviscid mechanism to analytically describe the breakup of the plunging jet. He saw the flow to be necessarily time dependent, in contrast to previous steady plunging jet models by Dias and Tuck (1993) and Jenkins (1994). The theory predicts that as the jet forms and stretches, perturbations form on the surface and grow in amplitude until the jet is broken up into independent strips and eventually droplets. Similar surface disturbances were noted in the experiments of Waniewski et al. (2002).

Considerable research has focused on the physics of liquid sheets, largely for industrial applications. A thorough overview of this area can be found in Lin (2003). Certain types of thin liquid sheets develop instabilities which may be similar to the striations observed in some plunging wave experiments and these instabilities can eventually lead to sheet breakup (Huang 1970).

1.5 2D+T Approximation

The 2D+T (Two Dimensions plus Time) approximation is a method for simplifying a three-dimensional system using a two-dimensional model. For ship waves, three-dimensional bow flow can be approximated by a two-dimensional, time evolving flow in which the hull is replaced by a deforming wall which at any time t ($t = 0$

is the moment of passage of the stem at the mean water level) takes on the shape of the cross section of one side of the hull at the streamwise (x) location corresponding to $x = Ut$ where U is the equivalent speed of the three-dimensional ship model. This method is applicable only to ships with fine bows moving at constant forward speed and only divergent wave components are produced. The flow is unaware of any longitudinal effects such as the stagnation point at the bow that would result in elevated water upstream of the hull. The impact of the stagnation point on upstream elevation is substantial for blunt-bow ships such as tankers; however, for narrow bows, the effect is relatively weak and thus is not a major source of error. Previous studies (Tulin & Wu 1997 and Shakeri et al. 2009a) have accounted for this with a small longitudinal shift of the resulting wave pattern.

Tulin and Wu (1997) numerically calculated the divergent waves generated by a Wigley-like hull using the 2D+T approximation and compared results with a fully non-linear 3-D solver (RAPID). Because of the lower computational cost, the 2D+T approximation allowed high resolution calculations of bow wave characteristics, sufficient to capture breaking, post-breaking and jet development in plunging breakers.

The 2D+T approximation can be used to represent any set of 2-D profiles as a 3-D wave field. Duncan et al. (1999) conducted a set of experiments to study short wavelength spilling breakers. A traditional plunging-type wave maker was used to create a series of waves which converged and broke via dispersive focusing. The resulting waves were measured as 2-D surface profiles. When the 2-D profiles are plotted by offsetting each successive wave profile upward and horizontally by

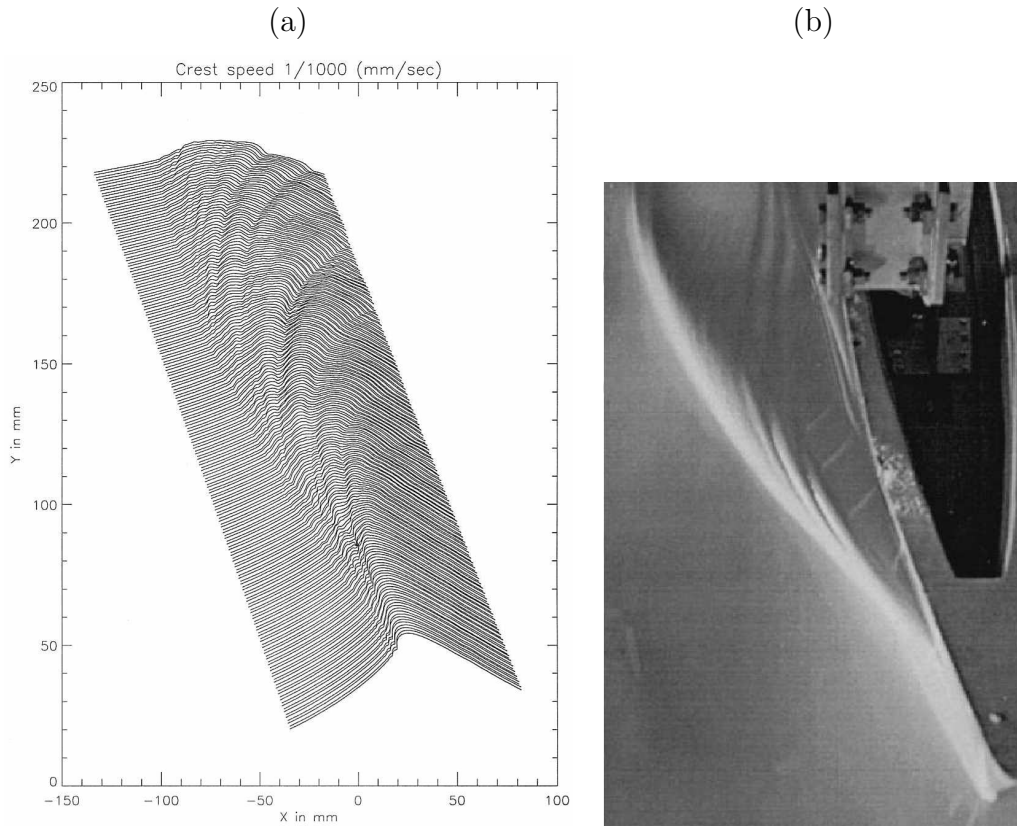


Figure 1.4: Comparison of 2-D wave profiles with a 3-D wave. (a) 3-D representation a spilling dispersively focused breaker using 2-D wave profiles (from Duncan et al. 1999) compiled according to 2D+T technique. (b) Overhead view of model test bow wave (from Dong 1997).

fixed distances (Figure 1.4), an equivalent 3-D wave field is produced in which many features in the surface pattern are similar to those found in 3-D tests of ship waves, such as Dong et al. (1997), which is also shown in the figure.

The success of the Duncan et al. (1999) study led to the construction of a 2D+T wave maker in the Hydrodynamics Laboratory at the University of Maryland. Using this wave maker, Shakeri (2005) and Shakeri et al. (2009a) simulated waves from a Navy destroyer hull (Model 5415 from NSWC Carderock). Using a similar

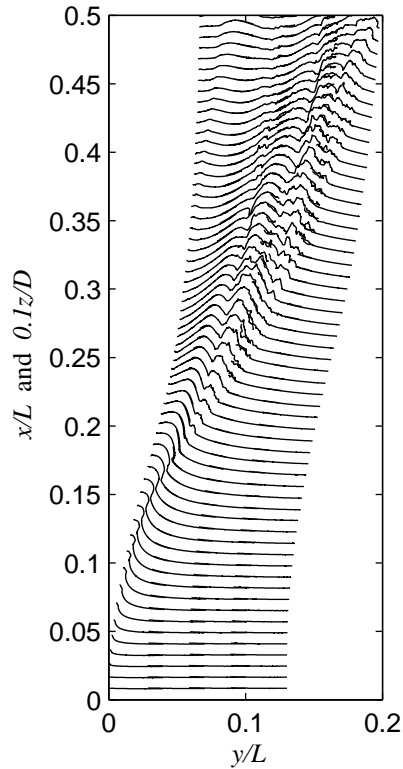


Figure 1.5: 3-D representation of a plunging bow wave created by a 2D+T wave maker (from Shakeri, 2009a). Profiles compiled by offsetting each 2-D surface profile by a fixed distance along the vertical axis.

plotting technique as Figure 1.4, profiles from a plunging breaker were plotted in a 3-D representation in Figure 1.5. In addition, comparison of the maximum height of the water contact line in the bow region with data from 3-D model tests and the theoretical considerations of Noblesse et al. (2006) were presented.

Comparisons with 3-D experiments were made in Shakeri et al. (2009b). The 2D-T wave maker was used to simulate bow waves produced by the R/V Athena (Model 5365 from NSWC Carderock) which were then compared with wave profiles from previous towing tank tests. The shape and maximum height of the contact

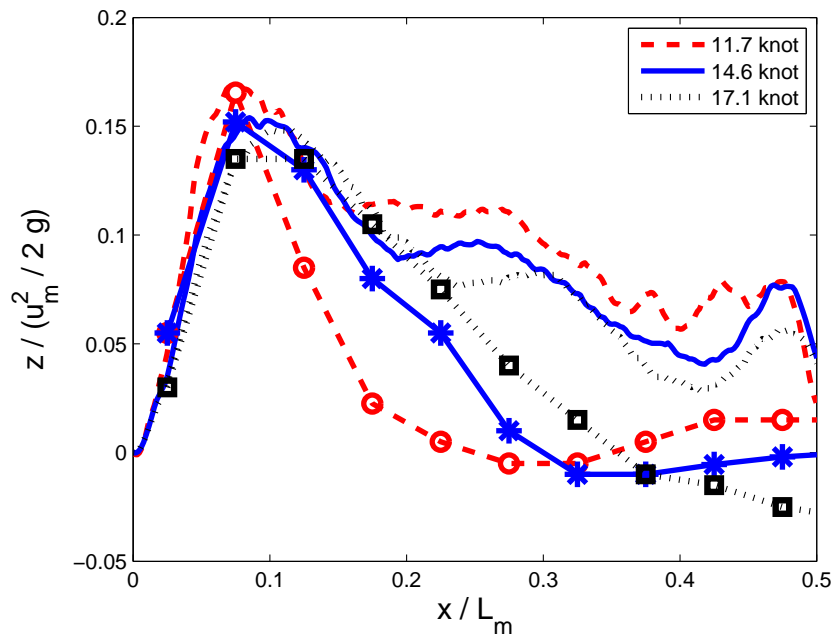


Figure 1.6: Contact line and wave profile measurements of R/V Athena hull using 2D+T wave maker (lines without data points) as compared with 3-D tank data (lines with data points). From Shakeri (2009b).

line are very similar for 2D+T and 3D data sets but the profiles tend to diverge downstream of the contact point (see Figure 1.6). As mentioned previously, a small longitudinal shift in the data was needed to account for the stagnation point of the 3-D model. The similarity of the wave profiles between the two sets of data improved with increasing Froude numbers, which is generally to be expected for the 2D+T approximation.

1.6 Thesis Outline

This thesis is divided into six sections, including the Introduction (Chapter 1). Experimental details, including descriptions of the wave maker and surface

profile measurement techniques, are presented in Chapter 2. Chapter 3 presents the experimental results of the wave generation and measurement. Relationships between wave maker parameters and basic wave geometric characteristics are also discussed. Chapter 4 analyzes various characteristics of the plunging jets observed in this study. Chapter 5 presents the methodology and results of the plunging jet thickness measurements. Chapter 6 discusses the two types of breaking waves, referred to as overdriven and developing, observed throughout this study and explores the underlying mechanics of each type. And finally, Chapter 7 presents the overall conclusions of the study, applications of the analysis and suggested areas of future study.

Chapter 2

Experimental Details

2.1 Test Facilities

2.1.1 Wave Tank

All testing for this study took place in the large wave tank of the University of Maryland Hydrodynamics Lab. The tank is 14.80 m long, 1.15 m wide, and 2.20 m deep, see Figure 2.1.

An instrument carriage is mounted on top of the tank. The carriage is driven by towing cables which in turn are powered by a servo motor. The carriage rides on hydrostatic oil bearings to reduce vibrations. A position sensor that runs the entire length of the test section is used to monitor the position of the carriage at any time. The carriage motion is controlled by a computer-based feedback system in order to produce highly controllable and repeatable motions.

2.1.2 Wave Maker

A schematic drawing of the 2D+T wave maker is shown in Figure 2.2. The wave maker is powered by four servomotors which, through gear reducers, drive four vertically oriented shafts. The vertical shafts in turn drive four horizontal drive pistons by way of four rack-and-pinion assemblies. The main component of the

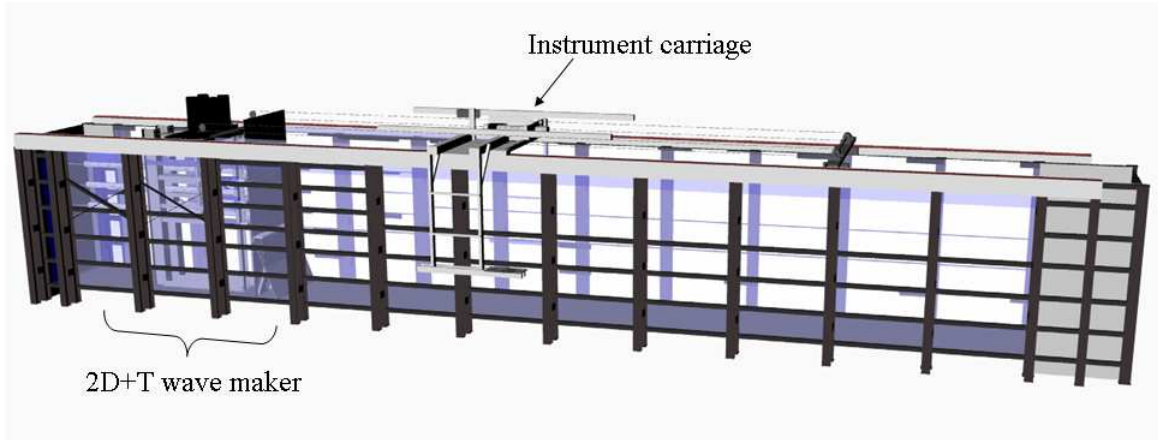


Figure 2.1: Schematic representation of the wave tank at the University of Maryland Hydrodynamics Lab.

2D+T wave maker is a flexible stainless steel board, hereby referred to as the wave board. The wave board is attached to the horizontal drive pistons via hinged drive plates. Manipulating the interrelated positions and velocities of each drive piston forces the wave board to be bend and translate to match a desired hull shape. Data from four position sensors, one for each drive piston, provide feedback for a computer controlled feedback system. The feedback system adjusts the velocity of each drive piston in real time to achieve the desired wave board motion.

The keel depth of the 2D+T wave maker is established by bending the wave board over a fixed horizontal surface, called the keel bar, that spans the width of the tank. The keel depth serves as the effective draft, d , for the model. For all tests in this study, the mean water depth was fixed at 0.892 m above the top surface of the keel bar for a total water depth of 1.70 m.

As shown in Figure 2.2, the wave board is extended and bent at each time step,

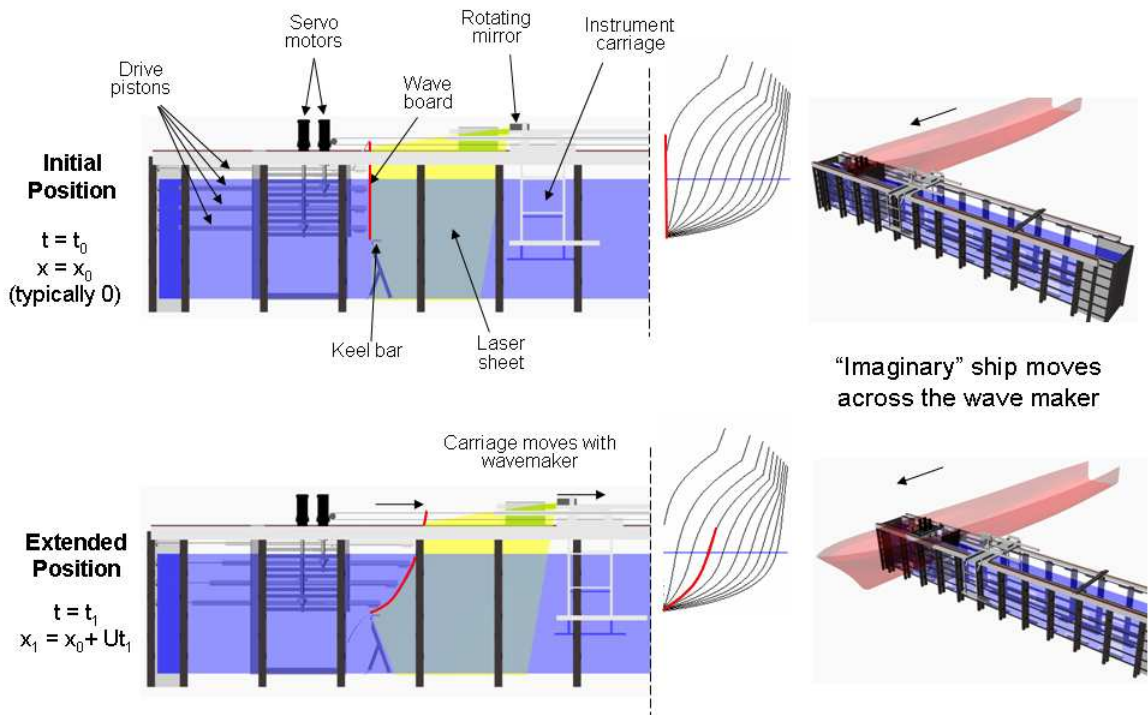


Figure 2.2: Overview of 2D+T experimental procedure. The initial position of the wave board simulates the bow of the ship being lined up with the 2-D plane of the wave maker. The extended position simulates the ship having moved forward a given amount and thus displacing the water with the corresponding hull shape for that position.

t , to mimic the corresponding half hull shape at a given longitudinal location, given by $x = Ut$. Typically, a test simulates half of a ship model from stem to mid-ship. The portion of the hull aft of mid-ship is assumed to be effectively parallel. Even if this section is not parallel on the actual ship, it likely has negligible influence on the bow waves and can be safely ignored.

A set of profiles of position versus time for the four wave maker drive channels for one of the wave maker motions used in this study are given in Figure 2.3a. The profiles are intended to approximate motion consisting of two stationary positions

connected by a zone of constant velocity. However, because the wave maker is a mechanical device, discontinuous velocities (i.e. infinite accelerations) are not possible and overly high accelerations may cause errors or even damage to the system. For this reason, a rounding scheme was used for the position profiles at the beginning and ends of the motion to approximate instantaneous changes in velocity. A third-order polynomial fit was used for this rounding in which acceleration increases linearly from zero to a peak value then back to zero (see Figure 2.3b). The time origin ($t = 0$) is based on the idealized, i.e. discontinuous velocity, profiles. The rounding period (T_R) is defined as a fixed portion of the wave maker run time (t_{wm}) and was used to standardize the acceleration across all cases. The acceleration and deceleration peaks are located at $t = 0$ and t_{wm} , respectively (see Figure 2.4). For $T_R = 0.5$, the acceleration begins at $t = -0.25t_{wm}$ and reaches full velocity $t = 0.25t_{wm}$ with the peak acceleration taking place at $t = 0$. The inverse then occurs for the end of the run ($t = 0.75t_{wm}$ and $1.25t_{wm}$). Unless specified otherwise, the value of T_R for all wave maker motions was 0.5. This acceleration scheme was judged to provide the smoothest wave maker motion with the least deviation from the idealized profile as compared with a number of other schemes that were examined. As can be seen in Figure 2.3, the rounding scheme does not significantly change the motion profile as the rounded profile (solid line) only visibly deviates from the idealized profile (dashed line) for a very brief period.

Figure 2.4 shows the velocity and acceleration profiles for one wave maker channel for a typical wave case. The “plateau” in the velocity plot (Figure 2.4b) is the velocity the wave maker would be at for the entire motion in the idealized profile.

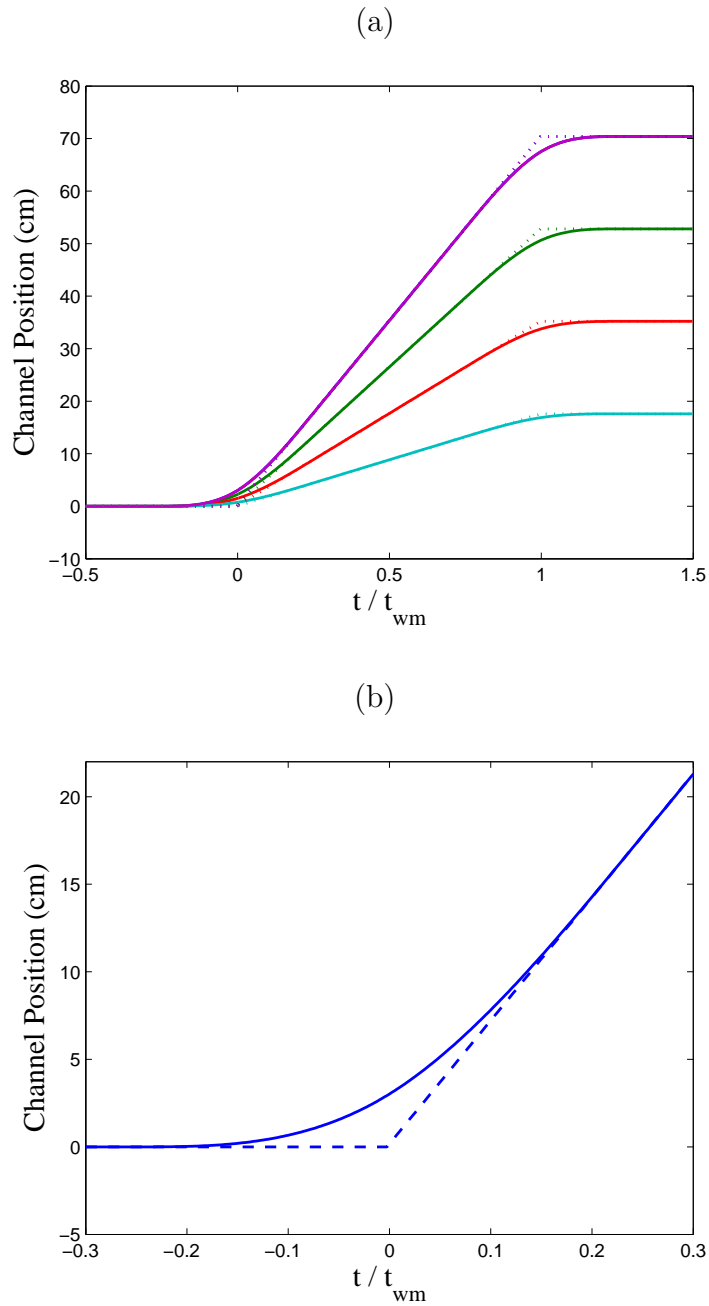


Figure 2.3: (a) Position histories for all four wave maker channels for a typical wave maker profile. Channel positions are the horizontal distance from starting position (vertical wave board). The solid lines indicate the actual profiles and the dashed lines indicate the idealized (infinite acceleration) profiles. (b) Close-up view of a typical initial acceleration for one of the channels.

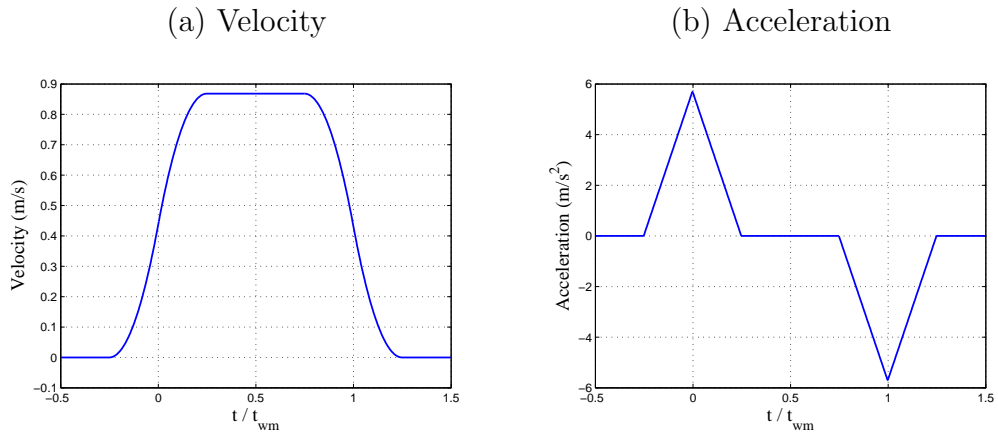


Figure 2.4: Profiles of acceleration (a) and velocity (b) for a single wave maker channel (i.e. drive piston) during a typical wave case, with time normalized by run time.

This velocity is referred to as the characteristic velocity. Wave board velocities are always taken in the horizontal direction (parallel to undisturbed water surface) regardless of board orientation.

2.1.3 Wave Maker Motion Categories

The goal of this study is to determine the relationship between generic, quantifiable wave maker motions and the resulting breaking waves. For this, a series of motions was used in which the wave board, with the exception of the region close to the keel bar, maintained the shape of a flat plate. There are five categories of motions used in this study (Figure 2.5). The first is rotation about a fixed point (called “Slap”), for which the position of the keel is fixed. The second is horizontal translation with the wave board held at a fixed angle of attack (called “Fixed”).

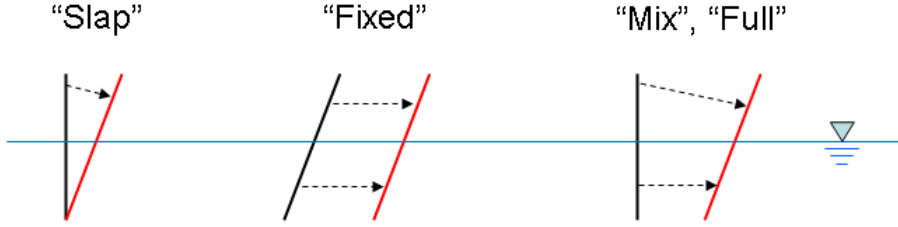


Figure 2.5: Graphical representations of the wave maker motion categories used in this study.

The angle of attack (α) is measured from vertical. There are three categories with simultaneous rotation and translation: “Mix 0.2”, “Mix 0.4” and “Full”. The rotation in the these cases is the same as in the Slap cases but with a translating bottom that acts as a translating center of rotation. Bottom translation is denoted by B_k , which refers to the beam at the keel depth. The term “Full” is used because it incorporated the largest translation the wave maker would allow (1.166 m at the waterline). The Mix cases have shorter translations than the Full case, effectively making them intermediate cases between the Slap and the Full cases (i.e. a “mix” between the Slap and the Full). The Mix 0.2 has a B_k value of ≈ 0.2 m and the Mix 0.4 case has a B_k value of ≈ 0.4 m. In this sense, the Slap, Mix and Full cases can all be thought of as being part of the same family of motions (rotating) and the Fixed cases are part of a second family (translation only).

The combinations of rotation and translation simulate fundamental components of bow shapes. The 3-D hull shapes that the Slap, Full and Fixed categories

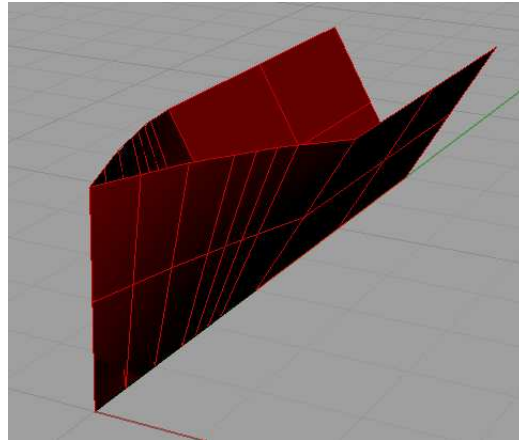
would represent are shown in Figure 2.6. Note that the Slap and Full motions create a ship-like shape. The Mix cases are also ship-like and the Fixed cases simply lack a forward stem. Again, it is important to point out that even though the wave maker motions are simple, quantifiable combinations of translation, rotation and angle of attack, they do indeed approximate ship-like shapes. Also, because of the generic nature of the wave maker motions, there is no particular full-scale ship dimension and thus no model size or scaling factor. The results of this study should therefore be more universally applicable than from simply simulating a particular hull.

Three important parameters that will be discussed throughout this report are wave board speed (V_b), wave board Froude number (F_b) and wave board acceleration (a_b). Wave board speed is defined as the characteristic velocity (the “plateau” in Figure 2.4) of the wave board along the static waterline. For the Fixed cases, the characteristic velocity is the same at any height on the wave board while the rotating cases have different characteristic velocities at different elevations. The wave board Froude number, F_b , is the Froude number using V_b as velocity and draft (d , 0.892 m for all cases) as the characteristic length. The wave board acceleration, a_b , is defined as the average acceleration along the static waterline during the initial acceleration (ramp-up) period. For the motions in this study, the acceleration profile is triangular (see Figure 2.4) and thus the average acceleration is simply half of the peak acceleration. These parameters may be calculated as follows:

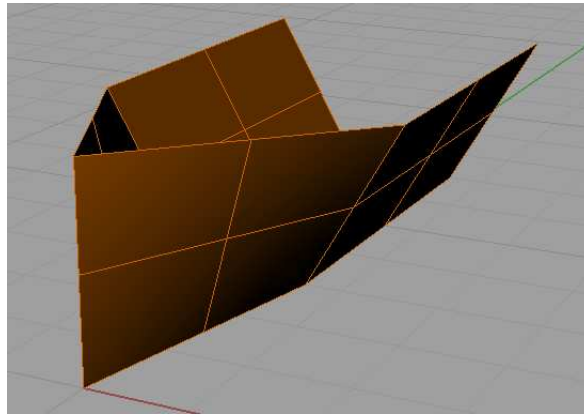
$$V_b = \frac{t_{wm}}{B_w}, \quad (2.1)$$

$$F_b = \frac{V_b}{\sqrt{gd}}, \quad (2.2)$$

(a) Slap



(b) Full



(c) Fixed, 30°

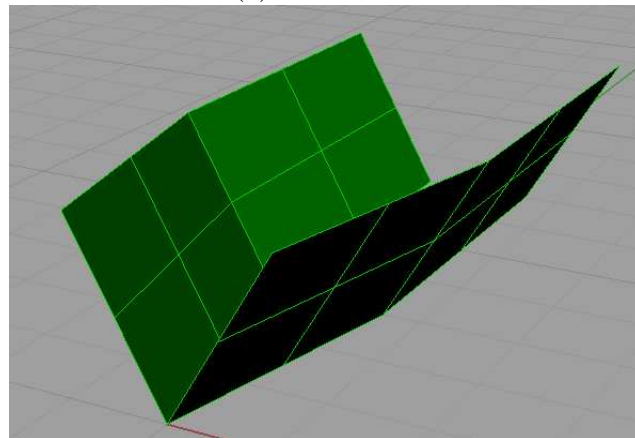


Figure 2.6: Equivalent 3-D hull shapes for wave maker motion categories (a) Slap, (b) Full and (c) Fixed, $\alpha = 30^\circ$.

Category	α_0 (degrees)	α_{end} (degrees)	B_k (m)	B_w (m)	t_{wm} (s)	V_b (m/s)
Slap	0	30	0	0.528	0.54 - 0.96	0.55 - 0.98
Mix 0.2	0	30	0.212	0.740	0.75 - 1.11	0.67 - 0.99
Mix 0.4	0	30	0.425	0.953	0.98 - 1.245	0.77 - 0.97
Full	0	30	0.637	1.166	1.11 - 1.35	0.86 - 1.05
Fixed	15, 20, 25, 30	same as α_0	0.610	0.610	0.65 - 1.17	0.52 - 0.94

Table 2.1: Table of wave maker characteristics for the five categories of wave maker motions, including the range of run times (t_{wm}) and wave board speeds (V_b). B_k and B_w refer to bottom (keel elevation) translation and waterline translation of the wave board, respectively

$$a_b = \frac{V_b}{T_R t_{wm}}, \quad (2.3)$$

where B_w is the total wave maker translation along the static waterline and is equivalent to half the waterline beam of the equivalent 3-D hull. Because draft is held constant for all cases, $\frac{1}{\sqrt{gd}} = 0.338$ s/m and thus F_b and V_b (in m/s) can be related using: $F_b = 0.338V_b$.

Table 2.1 lists the five wave maker categories and the ranges of the key wave maker parameters within each category. A detailed listing of the test cases is included in Appendix B. The run times, and subsequently the wave maker velocities, were chosen to span the range of breaking inception up to the fastest speeds the wave maker could reproduce without significant position errors or excessive stress to the system. This upper speed limit was not a significant restriction as strong plungers could be produced easily for all motion categories within the limits of the system.

The wave maker motions in this study can be completely defined using six independent variables. Although other combinations could be used, one complete set is: wave maker run time (t_{wm}), rounding period for the acceleration/deceleration (T_R), waterline translation (B_w), bottom translation (B_k), initial plate angle (α_0) and wave maker draft (d). As mentioned previously, d was constant for all tests and T_R is equal to 0.5 unless otherwise specified.

2.1.4 Wave Measurements

A Laser Induced Fluorescence (LIF) system was implemented to measure the temporal history of the water surface profiles of the waves generated by the wave maker. A single laser beam (Argon ion, ~ 7 watts) is focused and directed horizontally along the center of the top of the tank (Figure 2.7). The beam then intersects a rotating mirror assembly, which is mounted on the instrument carriage. The mirror is a 12-sided polygon rotating at about 12,000 rpm, which reflects the beam into very rapidly rotating “scans”. This effectively transforms the beam into a narrow laser sheet oriented along the centerline of the tank which intersects and illuminates the water surface.

The intersection of the light sheet and the water surface is photographed by a high-speed digital camera mounted on one side of the instrument carriage. The camera is a Phantom 9 (Vision Research Inc), which takes 1632 x 1200 pixel images at 256 frames/second. The camera views the intersection of the laser light sheet and the water surface through a flat mirror mounted on the opposite side of the carriage.

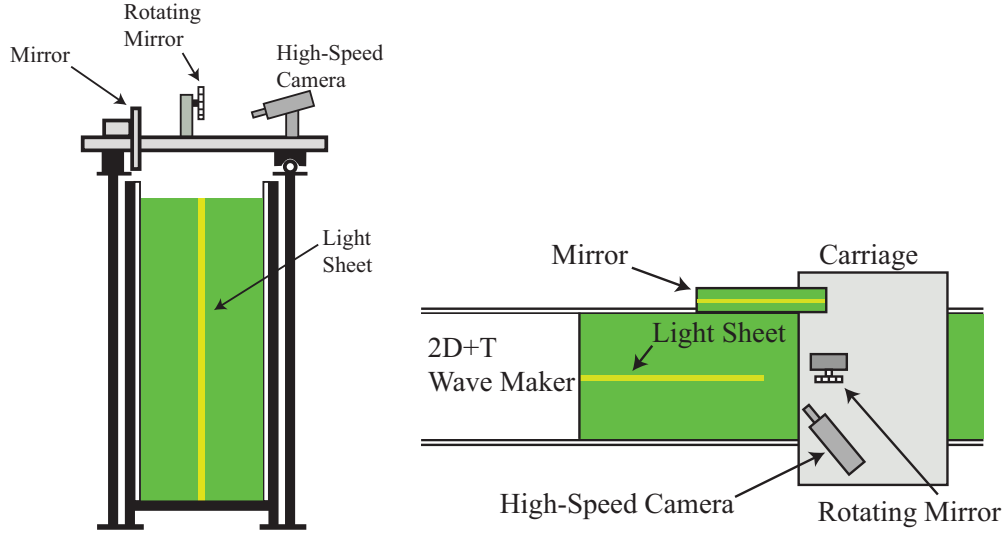


Figure 2.7: Details of optical setup. Longitudinal view (looking down the tank) is shown on the left and an overhead view is shown on the right.

This mirror is used to provide an unobstructed view at a reasonable viewing angle of the intersection of the laser light sheet and the water surface while the camera is mounted on top of the carriage. During recording of each movie, the wave maker motion and the carriage motion are all synchronized by a central computer.

The typical field of view for this setup is on the order of 85 cm (horizontal) x 60 cm (vertical). This yields a resolution of about 2 pix/mm. Because the wave field is often longer than the field of view, multiple movies are recorded of the same wave case, but done so at staggered starting positions known as “zones” with slightly overlapping fields of view. The waves created with this setup are very repeatable and therefore the successive zones can be overlaid to give a composite view of the wave with a larger effective field of view without sacrificing resolution. In general, two zones were sufficient to view all desired wave characteristics. Three movies were

typically recorded at each zone.

2.2 Image Processing

The intersection of the water surface and the laser sheet creates a sharp, clearly visible black-to-white edge in the images. A gradient-based algorithm is used to trace this edge in each wave image. This resulting surface profile is in the image coordinate system with units of pixels. In order to transform the surface profile into physical space, an inverse mapping procedure is employed. Before and after every set of tests, images of a large black and white checkerboard, which is oriented in the plane of the laser light sheet in the tank (Figure 2.8), are recorded with the camera in the same position and orientation as when surface profile measurements are taken. The checkerboard is used as a fixed grid in space which can be used to map image coordinates into physical coordinates and thus transform measurements from wave images into real space measurements. The origin of the physical coordinates, hereby referred to as the test origin, is the intersection of the water surface and the wave board when the wave maker is in its initial position. When considering errors in image calibration, edge detection in the images and determining the carriage position when the image is taken, measurement of the water surface is estimated to have an accuracy of ± 1.3 mm in the physical plane (Shakeri et al. 2009b).

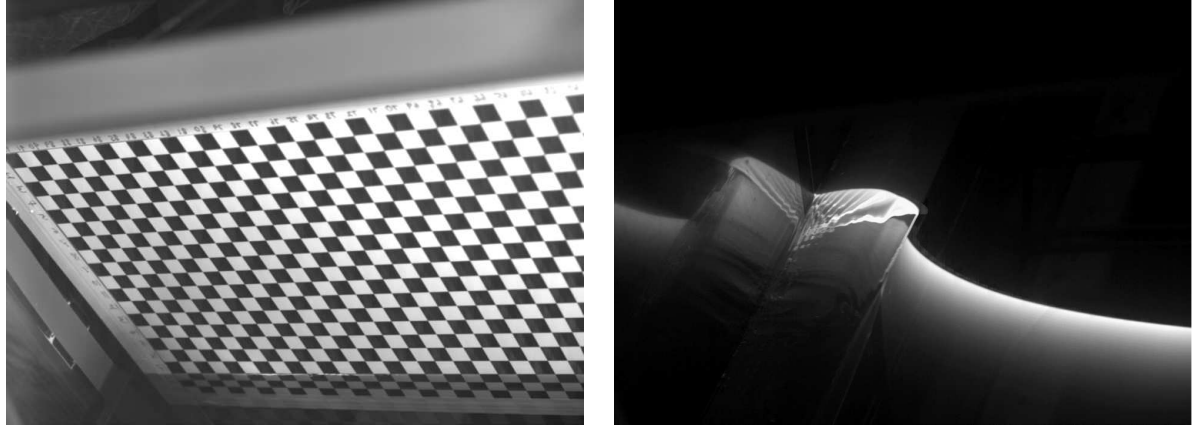


Figure 2.8: Images of the calibration board (left) and an actual test wave (right). Both images are taken from same camera position and orientation with respect to the tank.

2.3 Post-Processing

Figure 2.9 shows a typical wave image with several of the important features pointed out. Locations of the contact point, crest and jet tip will be tracked over time and space. The contact point and jet tip are identified visually from the images whereas the crest location is determined by calculating the point of local maximum height in an individual surface profile.

2.4 Repeatability

In general, both the wave maker and the measurements techniques produced very repeatable results. A plot of surface profiles taken at the same 1/16 second intervals for three successive runs of the same test case is shown in Figure 2.11. The profiles are virtually identical (within 1 mm) except for the regions around

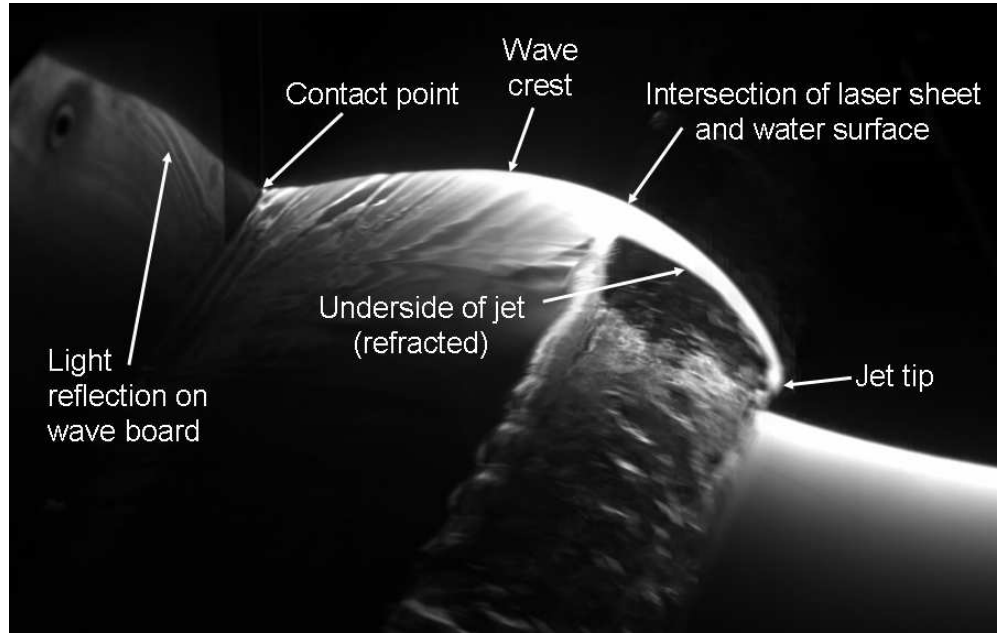


Figure 2.9: Various features of a typical wave image (Slap, $V_b = 0.98$ m/s).

the jet tip and the splash zone where there is only slight deviations due to random fluctuations which appear to be caused by turbulence-induced surface motions. The agreement in the image overlap region between the different zones, which result from separate wave runs of the same case, is also excellent. An example set of surface profiles taken from two zones is shown in Figure 2.10. The different colors indicate profiles taken from different zones. The strong overlap of the two sets of profiles demonstrates both repeatability and accuracy in the experimental techniques.

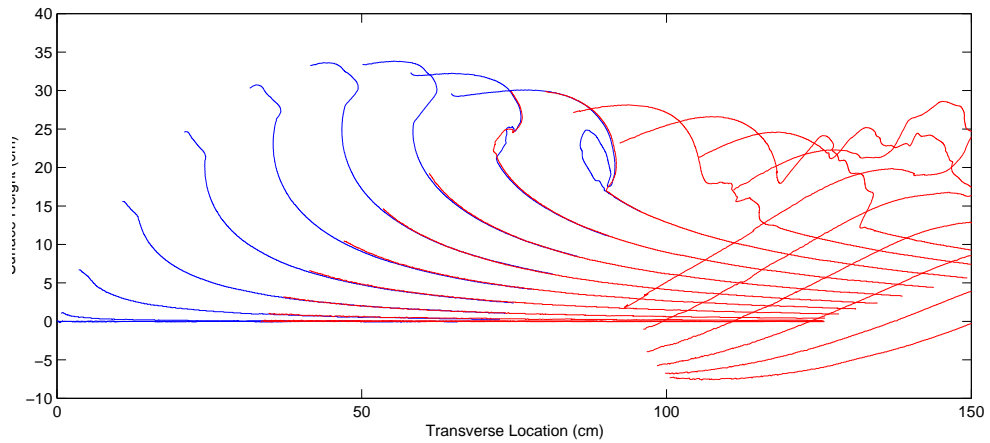


Figure 2.10: Water surface profiles taken at 1/16 second intervals for Slap case, $V_b = 0.98$ m/s. The different colors (blue and red) indicate profiles taken from different measurement zones.

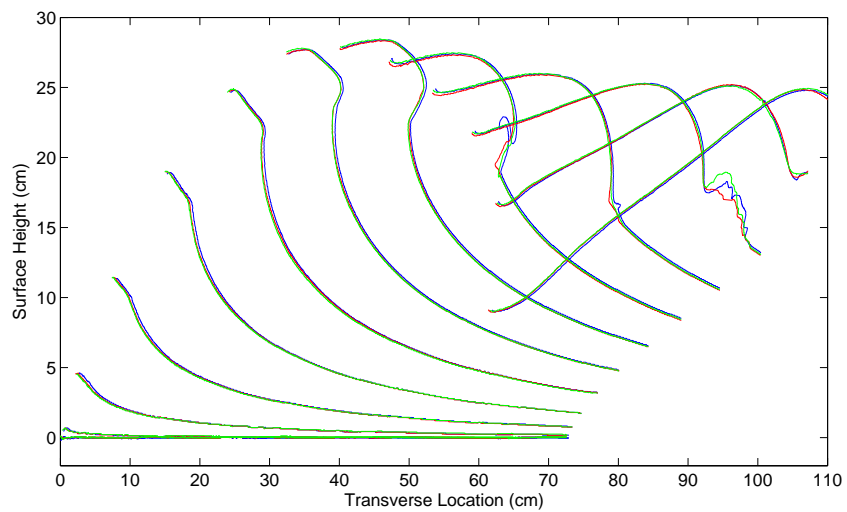


Figure 2.11: Water surface profiles taken 1/16 second intervals from three successive runs (shown as different colors) of the same wave maker motion (Slap, $V_b = 0.87$ m/s).

Chapter 3

Wave Results

3.1 General Observations

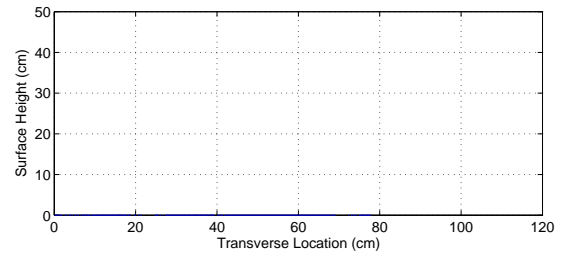
A total of 46 different cases were tested, all within the parameters of Table 2.1 (see Appendix B specific individual case parameters). Time series images and surface profiles, which are in real-space coordinates, for a typical wave case are shown in Figure 3.1. Prior to any motion (a, $t = -0.16$ s), the surface is flat and normalized to zero elevation. As the wave board begins to move forward (b, $t = 0.15$ s), the surface deflects upward in the area near the wave board. This surface deflection often appears as a vertical jet along the wave board. As the wave board continues to move, the surface deflection continues upward (c, $t = 0.34$ s) and begins to form a bulge near the peak of the wave. If the wave board velocity is sufficient, the wave will break and, depending on various wave maker parameters, this bulge will eventually form either a spilling region or plunging jet. After a short time, the wave begins to move away from the wave board and breaks (d, $t = 0.46$ s). This particular wave case is a weak plunger. After the wave breaks, a sizable splash results, dissipating considerable energy as it continues to propagate away from the wave board (e, $t = 0.65$ s). Comparing the corresponding images and surface profiles shows clearly the optical skewness of the images and thus highlights the importance of the inverse transformation process discussed in Section 2.2.

The various wave maker motions produced very different looking waves. Figure 3.2 shows images taken at the moment of jet impact of six different cases. All cases were run within a relatively narrow range of wave board speeds (between 0.94 and 0.99 m/s) and all developed clearly defined plunging jets. The resulting waves have very different overall shapes despite being produced by similar wave board speeds. In general, the Slap and Fixed cases tend to break close to the wave board whereas the Full cases take longer to develop and break further from the wave board. The wave shapes observed in the Mix cases tend to be in between the Slap and Full cases. For the Fixed cases, the shape of the breaker is highly dependent on the angle of the wave board. Both Fixed cases were run at the same wave board speed but the steeper angle of attack (30° vs. 15°) throws the water much further away from the wave maker and results in a longer, flatter plunging jet.

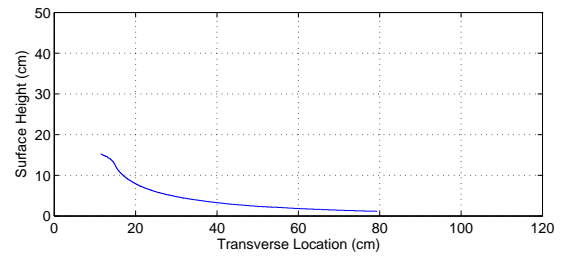
3.2 Contact Points

The position of the contact point, which is the intersection of the water surface and the wave board, was tracked in time for each case. All positions are with respect to the test origin, which is the location of the contact point when the water is undisturbed and the wave maker is in its initial position. Contact point heights, Z_c , for most cases are plotted against time in Figure 3.3. In each plot, the maximum contact point height increases with increasing V_b . Even though the maximum height values are different, the peaks all tend to line up at approximately the same point in time for all cases (≈ 0.37 s). This will be further discussed in the next section.

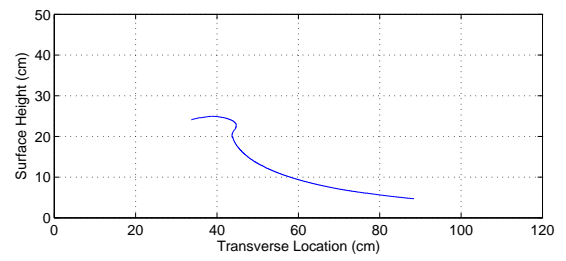
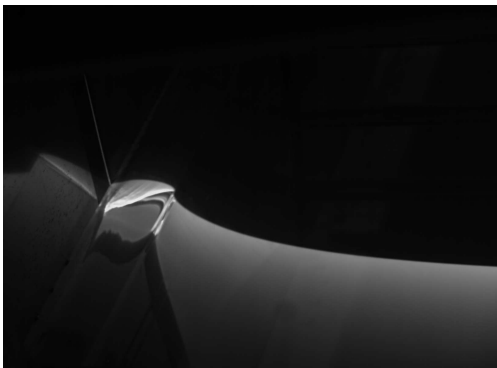
(a) $t = -0.16$ s



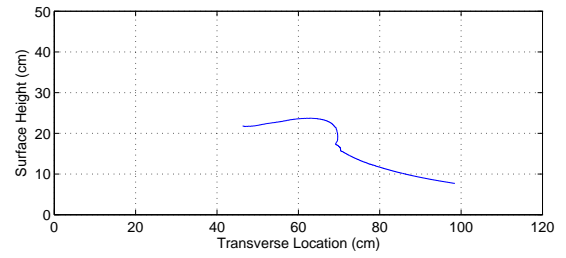
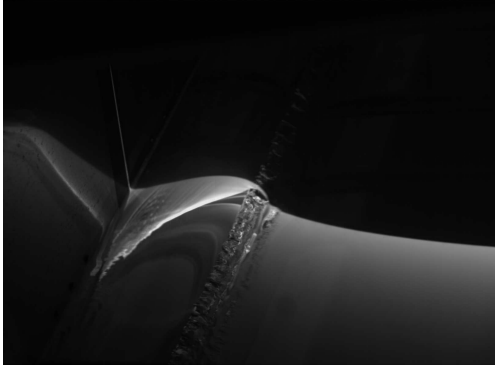
(b) $t = 0.15$ s



(c) $t = 0.34$ s



(d) $t = 0.46$ s



(e) $t = 0.65$ s

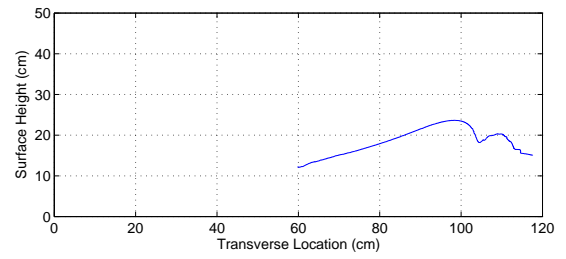
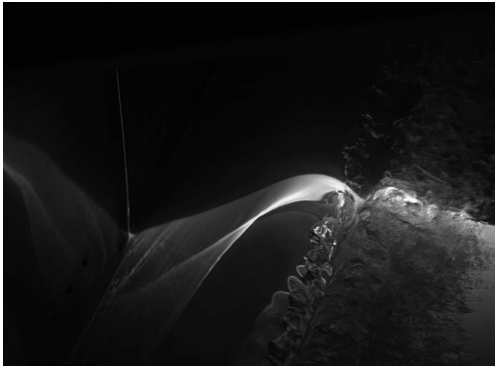
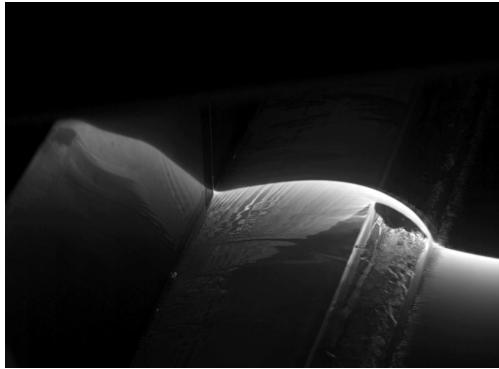
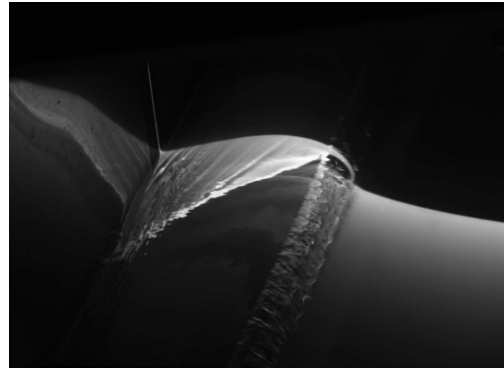


Figure 3.1: Time series of a typical wave profile (Slap, $V_b = 0.8$ m/s, $t_{wm} = 0.66$ s). The figures in the left-hand column are unprocessed images from the high-speed movies and the figures on the right are corresponding surface profiles.

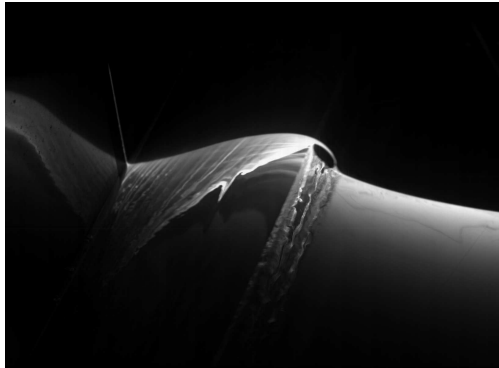
(a) Slap



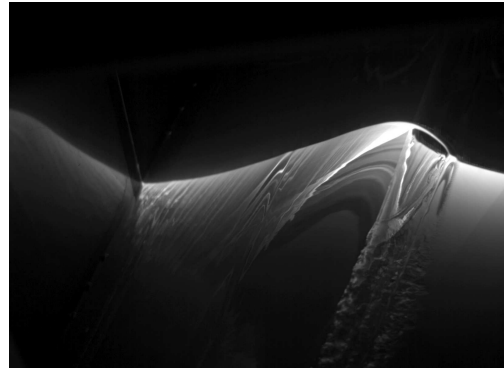
(b) Mix 0.2



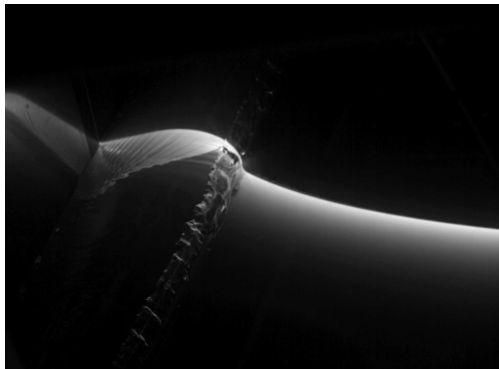
(c) Mix 0.4



(d) Full



(e) Fixed, 15°



(f) Fixed, 30°

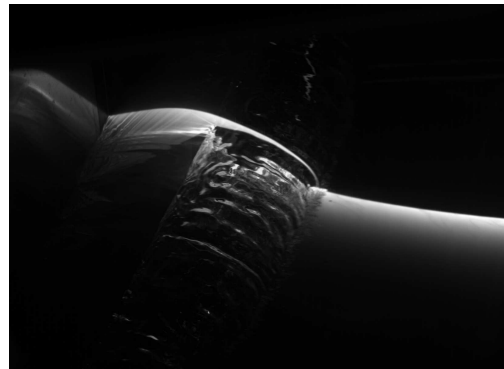


Figure 3.2: Wave images taken at the moment of plunging jet impact. All cases run at approximately the same wave board speed ($0.94 \leq V_b \leq 0.98$ m/s)

A number of normalization schemes were considered for collapsing the contact point height versus time data for all cases. Froude scaling (i.e. using V_b) proved to be sufficient in normalizing all the peaks within a particular wave maker motion but did not work well between the motion categories. Normalization using wave board acceleration, a_b , when combined with Froude scaling, is capable of normalizing the peaks both within a particular motion and across the categories. All normalization schemes required empirical coefficients and powers to be successful. The best normalization scheme was judged to be a formula containing draft, Froude number, wave board acceleration and gravity:

$$(Z_c)_{normalized} = A_1 \left(\frac{Z_c}{d}\right) (F_b^{A_2}) \left(\frac{a_b}{g}\right)^{A_3}, \quad (3.1)$$

where A_1 , A_2 and A_3 are empirical coefficients. Froude scaling is accounted for with A_2 and the acceleration scaling is accounted for with A_3 . These coefficients were empirically derived so that all normalized peak contact points for all profiles would be as consistent as possible. Then A_1 was determined to set all values at approximately 1. For this, A_1 , A_2 and A_3 are equal to 0.52, -1.33 and -0.15, respectively. The values of the coefficients indicates that Froude scaling is dominant over acceleration scaling, though both are required. Figure 3.4 plots the contact points using this normalization scheme. The time axis is non-dimensionalized using gravity and draft, for which both values are constant for all tests. For each motion category, the contact points follow a self-similar trajectory. Each speed has a common rise path but higher speed cases depart from this path at a higher elevation before dropping with a similar shape as the lower speed cases. In general, the Slap and the Fixed

cases have nearly identical trajectories. The Full case data, on the other hand, have a very different shape with a distinctive second peak near the end of the wave maker motion. Because the Full motion lasts a longer time - about twice as long for a given wave board speed as other wave maker motions - the peak contact point occurs relatively early in the run. As a result, the wave board is still moving and pushing water well after the wave has begun to move away. The water level behind the wave remains elevated and a secondary wave forms at the end of the run, which is visible as a second peak in the contact trajectory. The shorter Mix 0.2 case appears similar to the Slap case while the Mix 0.4 case demonstrates a slight second peak, similar to the Full case.

Because the normalization scheme used in Figure 3.4 suggests a strong correlation with F_b , the peak contact points (normalized by d) were re-plotted against only F_b (see Figure 3.5). As expected, a strong linear relationship is observed. A straight-line curve fit (using least-squares method) of this plot has an x-intercept value of about 0.068, which corresponds to a wave board speed of about 20 cm/s. This is quite close to the minimum phase speed of 23.2 cm/s for a linear gravity-capillary wave in clean water (Lamb, 1932). Therefore, no steady waves would be created at wave board speeds less than this minimum phase speed.

3.3 Time to Peak Contact Point Height

An important component of the contact profile is the point in time when the peak contact height is achieved, as measured from $t = 0$ (profile start). The time

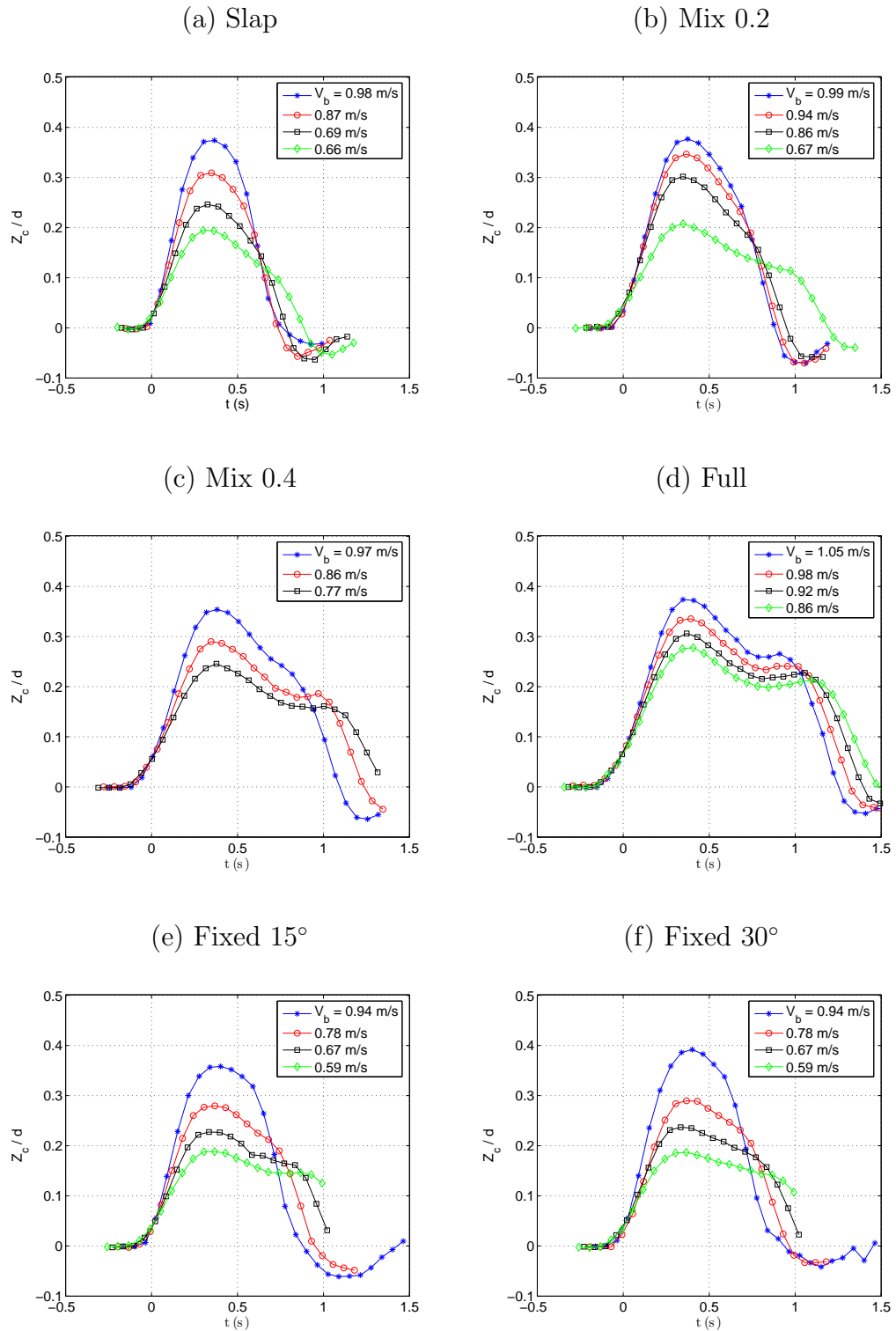


Figure 3.3: Plots of contact point height (normalized by draft) versus time: (a) Slap, (b) Mix 0.2, (c) Mix 0.4, (d) Full, (e) Fixed, $\alpha = 15^\circ$, (f) Fixed, $\alpha = 30^\circ$.

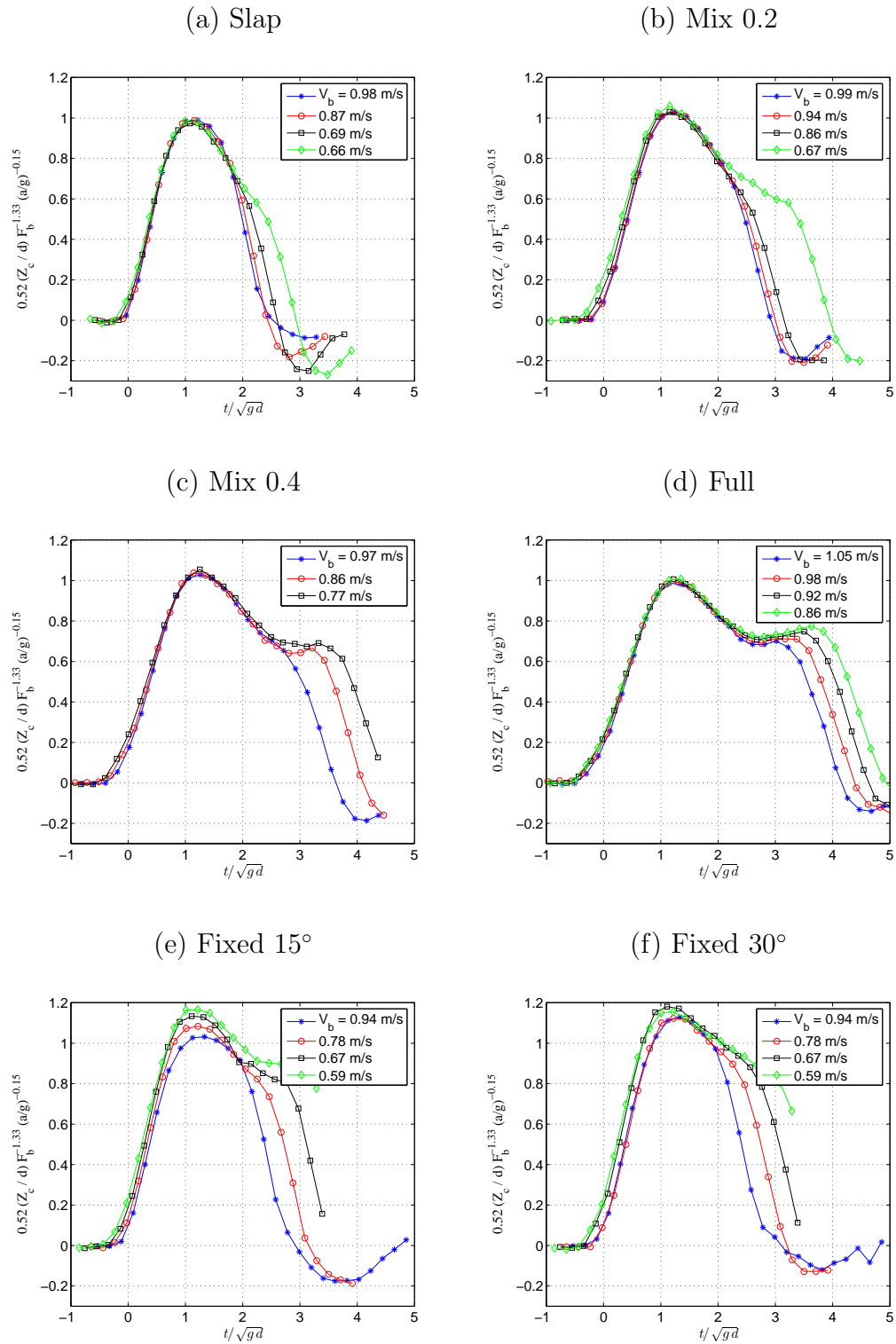


Figure 3.4: Plots of fully normalized contact point height versus non-dimensional time: (a) Slap, (b) Mix 0.2, (c) Mix 0.4, (d) Full, (e) Fixed, $\alpha = 15^\circ$, (f) Fixed, $\alpha = 30^\circ$.

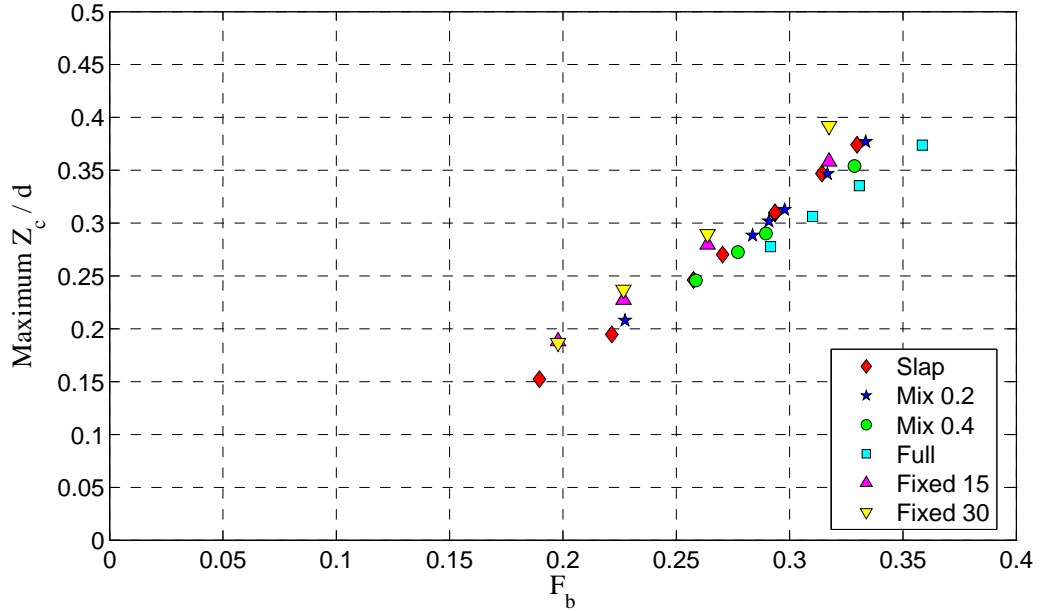


Figure 3.5: Non-dimensional maximum contact heights for various wave maker profiles.

to peak contact point height is given by t_{cp} . At the moment of peak contact point height, the wave detaches from the wave board and begins to move away from it. Interestingly, there is little variation in the time at which the peak contact point height occurs. Figure 3.6 plots the t_{cp} versus F_b . In general, all peak contact point heights occur between $t = 0.300$ and 0.429 seconds with an average of 0.367 (variability of $\pm 18\%$), even though the variation of run time (t_{wm}) is between 0.542 and 1.350 seconds across the various profiles. The Fixed cases tend to have greater peak contact point height times, with an average value of 0.393 seconds. The remaining cases (rotating) have a t_{cp} range of 0.300 to 0.407 seconds and an average t_{cp} of 0.354 seconds. This equates to a variability of $\pm 15\%$, which is compared to a $\pm 100\%$ variability in wave maker parameters like t_{wm} and a_b . It is important

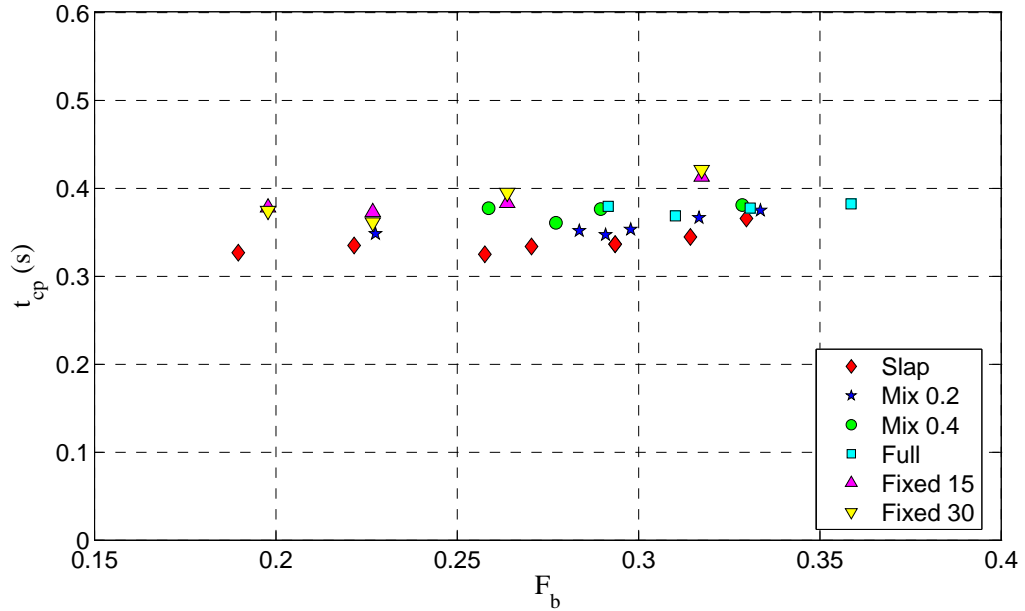


Figure 3.6: Time to peak contact point, t_{cp} , versus F_b .

to keep in mind that these contact point peaks occur at very different vertical and horizontal locations (with respect to the test origin) and result from a wide variety of wave board velocities and accelerations, yet do so at a remarkably consistent time.

The peak contact point height times from previous 2D+T studies were also measured. These tests had different drafts and water depths than the present study (0.892 m and 1.70 m, respectively). The 5415 hull form tests (Shakeri et al. 2009a), with a draft of 0.91 m and a water depth of 1.83 m, had an average time of 0.55 seconds, $\pm 7\%$. The Athena tests (Shakeri et al. 2009b), with a draft of 0.62 m and a water depth of 1.53 m, had an average time of 0.36 seconds, $\pm 3\%$. Both sets of tests produced fairly uniform times, similar to the behavior observed in the present study, but the actual values do not appear to correspond in any way with the draft

or the water depth. It should be noted that these two studies have very different wave maker shapes and motion profiles compared to the present study. Nonetheless, a noticeable consistency in the time to peak contact point height is observed within each of three studies.

Delhommeau et al. (2009) performed bow wave calculations for a parametric set of bow shapes using thin-ship theory. Several parameters were considered including entrance angle, rake and flare. As part of this, the longitudinal location of the contact point peak (referred to as bow wave peak in that study) was calculated and thus for comparison with the present work the peak contact point height time can be deduced using $t = x/U$. All 2D+T approximations assume zero rake (vertical stem). The Delhommeau et al. study uses a variable, φ , which is a parameter based on the entrance angle and flare of the hull and is defined as follows:

$$\varphi = \frac{\tan(\alpha) - \tan(\alpha')}{\tan(\alpha) + \tan(\alpha')}, \quad (3.2)$$

where α is the waterline entrance angle of the hull and α' is the bottom entrance angle (at keel depth). Using L_m as a notional model length, these angles may be calculated for the motions in the present study using $\alpha = B_w/L_m$ and $\alpha' = B_k/L_m$. When calculating φ for the wave maker motions, L_m cancels out and φ ends up being only dependent on B_w and B_k . The equivalent values of φ for the wave maker motions in this study are listed in Table 3.1.

Data from Delhommeau et al. (2009) for zero rake was adapted to calculate a time to peak contact point height for a draft of 0.892 m (keel draft used in the present study). This is plotted versus F_b in Figure 3.7 for three values φ , 0, 0.5 and 1.0,

Motion	φ
Slap	1.0
Mix 0.2	0.55
Mix 0.4	0.38
Full	0.29
Fixed	0.0

Table 3.1: Equivalent values of φ , as defined in Delhommeau et al. (2009), for wave maker motion categories in the present study.

that approximately correspond to the Slap, Mix 0.2 and Fixed cases, respectively. For each value of φ , t_{cp} is essentially constant once an adequate Froude number is reached (note: Froude number here uses forward ship speed and draft). For the present study, only cases with breaking were examined and therefore all cases are likely considered high speed. Thus, it is possible that all speeds examined were sufficiently high enough to yield a consistent time like was shown by the thin-ship theory calculations. A second observation is that although the actual times do not correspond to those observed in the present study, it is interesting to note that $\varphi = 1$ had the lowest time and $\varphi = 0$ had the highest. This was also observed in the present study (see Figure 3.6), though to a much lesser degree. We see the Fixed cases ($\varphi = 0$) have the highest values of t_{cp} and the rest of the cases approximately agree with the trend of decreasing t_{cp} with increasing value of φ . The 2D+T cases do not model rise of water at the ship stem, which effectively pushes the start of the wave upstream of the bow. Doing so affects the starting location from which the peak location, and subsequently the time to peak contact point height, is measured.

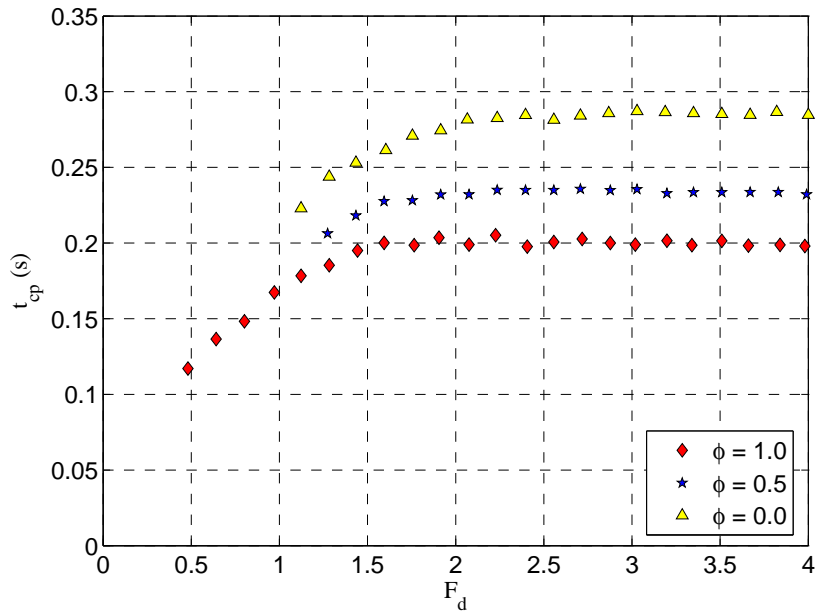


Figure 3.7: Equivalent time to peak contact point height versus Froude number using thin-ship theory for three values of φ (from Delhommeau 2009). F_d is the Froude number based on forward hull speed and hull draft. Values of 1.0, 0.5 and 0.0 approximately correspond to Slap, Mix 0.2 and Fixed cases, respectively

It is not possible to quantify the effect of this on the comparisons but it very likely contributes to the discrepancies.

3.4 Peak Surface Height

Peak surface height (Z_p) is defined as the maximum height of the water surface in a given surface profile, excluding any splash that occurs after the wave breaks. During the early stages of wave development, Z_p is equal to the contact point height (Z_c). After wave detachment, the peak surface height is typically the wave crest height. The maximum value of Z_p over the duration of a given wave can be used

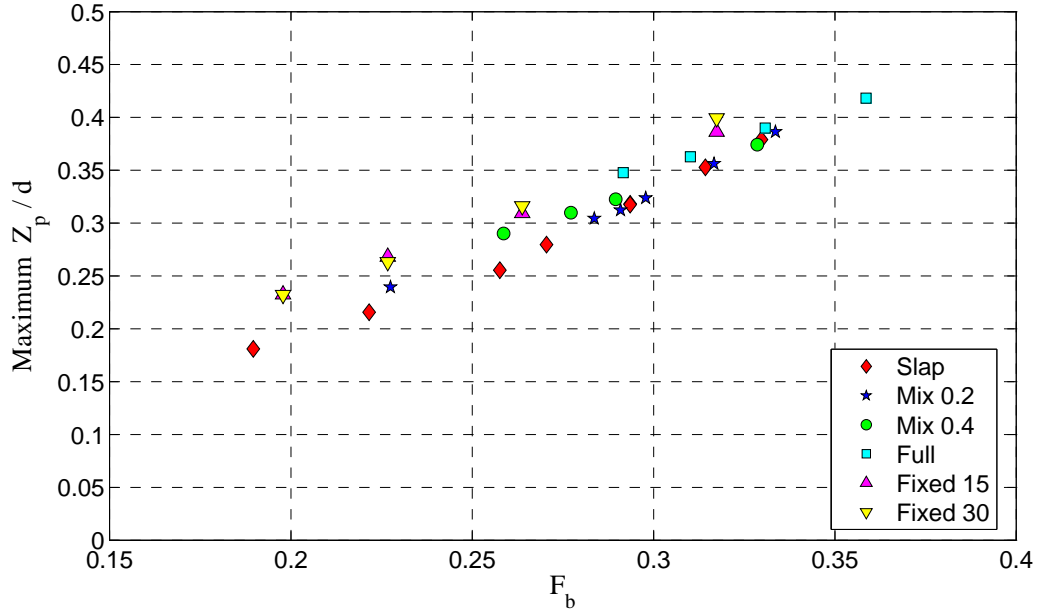


Figure 3.8: Non-dimensional maximum surface heights for various wave maker profiles plotted against F_b .

as a measure of wave height. A plot of maximum Z_p/d versus F_b is shown in Figure 3.8. There is a strong linear relationship between the wave board speed (recall $F_b = 0.338V_b$) and peak wave height, even with the different wave maker motion profiles and very different looking waves that result (see Figure 3.2). This was also observed in previous 2D+T studies (Shakeri et al. 2009a, 2009b) where the wave maker used a single motion profile over a wide range of wave board speeds. A straight-line curve fit (using least-squares method) of this plot has an x-intercept value of $F_b = 0.085$, which corresponds to a wave board speed of about 25 cm/s. As was also observed with the contact point height data in the previous section, this value is close to the minimum phase speed of 23.2 cm/s for gravity-capillary waves.

An unexpected but interesting result of this linear relationship is that the vari-

ation of the angle of attack (α) in the Fixed cases has little effect on the height of the wave, even though the waves have dramatically different shapes (recall Figure 3.2e & f). This is consistent with the idea that wave height squared is proportional to wave energy and that the main input of energy into the wave is derived from the wave board motion and subsequently the velocity of the wave board. However, the actual energy transfer between the wave board and the water is not measured and therefore this is largely speculative without further study. Nonetheless, the angle of attack appears to only alter the horizontal trajectory of the jet particles and a steeper angle (increasing α) simply “stretches” the wave horizontally.

The time histories of the peak surface heights were also examined. In order to compare behavior among the different motion categories, normalized peak surface heights for several cases ($V_b \approx 0.98$ m/s) are plotted against time in Figure 3.9. The data has been normalized in the same manner as the contact points (§3.2). The rotating cases (Slap, Mix and Full) are shown in Figure 3.9a. The Slap case has a pronounced peak and then a steady descent as the wave breaks. The Full case, on the other hand, does not have this same peak but rather continually increases in wave height as it moves further away. The Mix 0.4 case is more similar to the Full case, but with a bit of the peak observed in the Slap and Mix 0.2 cases. There appears to be a steady progression in shape with increasing wave board translation (recall Table 2.1). The Fixed case data is compared with the Slap and Full cases in Figure 3.9b. The Fixed cases both have higher peak values and do not seem to follow the patterns of the rotating cases. It should be noted that the Fixed cases tend to break early and close to the wave board and thus often do not have a clear

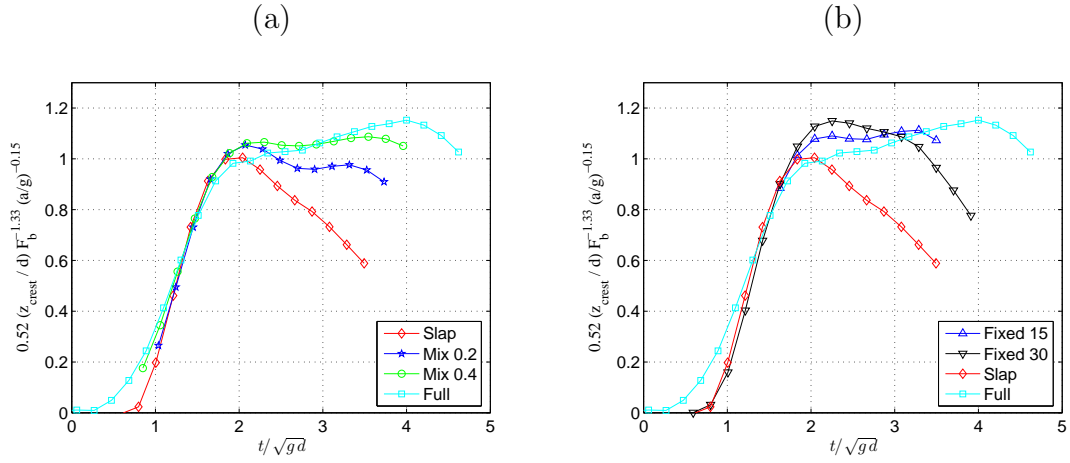


Figure 3.9: Froude-normalized time histories of peak surface height for various wave maker profiles, all at approximately $V_b = 0.98$ m/s. For clarity, all rotating cases are shown in (a) and Fixed, Slap and Full cases are shown in (b).

wave crest as it is typically defined.

3.4.1 Wave Crest Speed

Wave crest speed was measured by tracking the location of the crest of the wave up to the point where wave breaking and any subsequent splash has overtaken wave crest. Figure 3.10 displays the ratio of wave crest speed (V_{crest}) over wave board speed. The values generally decrease from 2.6 to 2.0 as wave board speed is increased. Measurements from the 5415 hull form tests (Shakeri et al. 2009a) are also plotted on this figure. The 5415 crest speeds decrease as the wave board speed is increased, but appear to level off to a consistent value of about 1.7 for F_b values greater than 0.35 (there is only one data point for $F_b = 0.35$ in the present study). For values less than 0.35, the two sets of data appear similar in magnitude and with

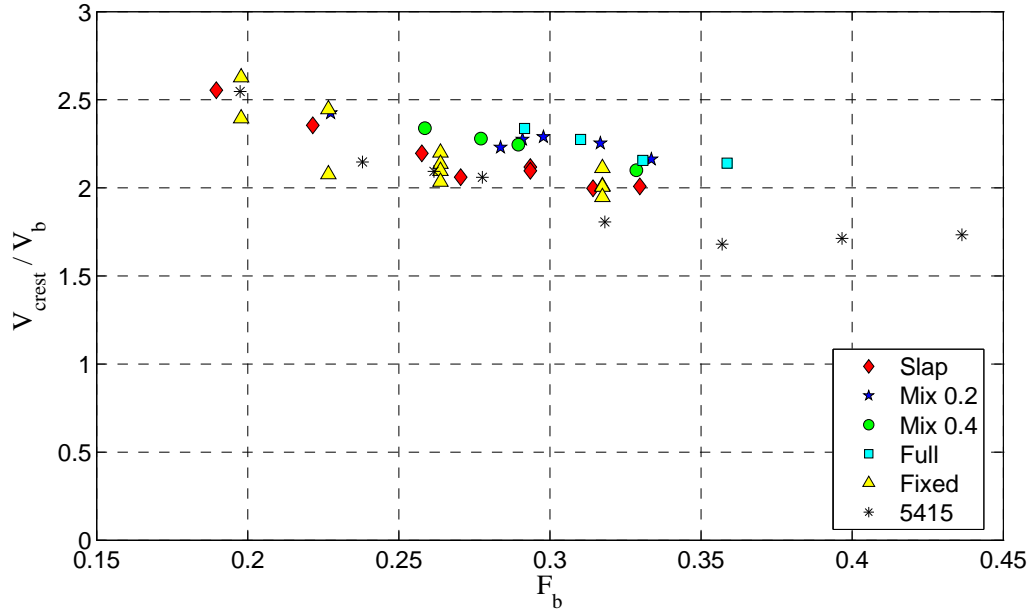


Figure 3.10: Normalized wave crest speed versus F_b for all wave maker motion categories. Data from 5415 hull form tests (Shakeri et al. 2009a) is included.

decreasing trend. It should be noted that the 5415 study used a deeper wave maker depth and slightly deeper water depth, in addition to significantly more complex wave maker motions.

3.5 Breaking Characteristics

3.5.1 Breaker Type

When the data points from Figure 3.8 are replotted using colors to indicate breaker type (spilling, plunging, or a transition between the two), a noticeable delineation appears (see Figure 3.11). Regardless of wave maker motion category, only

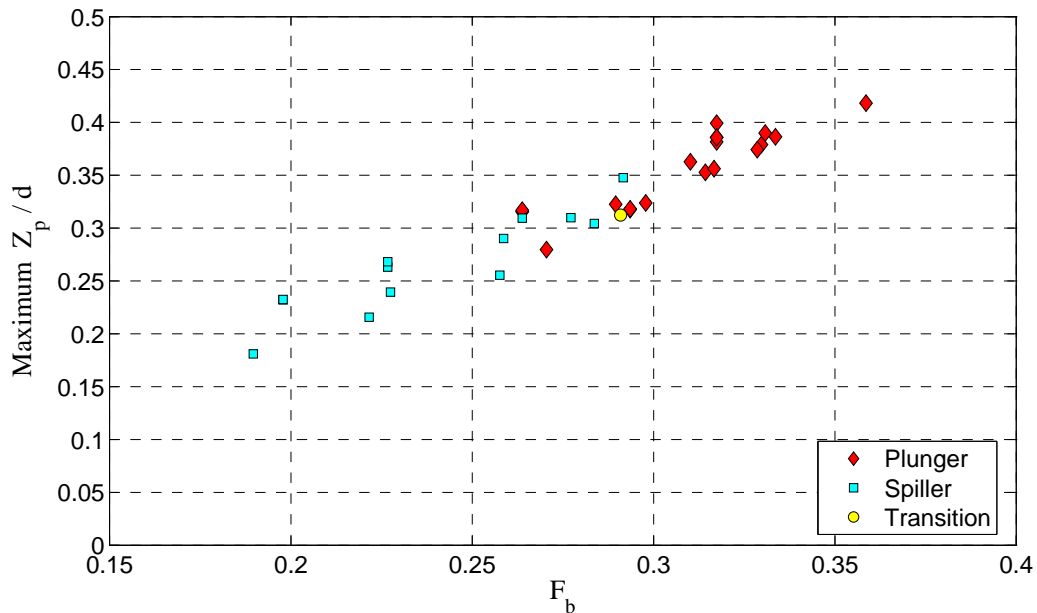


Figure 3.11: Non-dimensional peak crest heights for all profiles, identified by breaker type.

spilling occurs when $F_b < 0.26$ and only plunging occurs when $F_b > 0.29$, with an overlap region in between. Comparing Figure 3.8 and Figure 3.11, it can be seen that each region of breaker type contains the full set of wave maker motion categories. This is particularly interesting in that despite the very different wave maker profiles and very different looking waves in Figure 3.2, the breaker type has a strong correlation with the rather simple parameter of wave board speed, which only contains information about the waterline motion. In other words, with regards to breaker type, the wave maker motion at the water line is much more important than the motion away from the water line.

Category	Waterline Translation B_w (m)	Breaking Onset, V_b (m/s)	Breaking Onset, a_b (m/s²)
Slap	0.528	0.56	1.20
Mix 0.2	0.740	0.67	1.22
Mix 0.4	0.953	0.77	1.22
Full	1.165	0.86	1.28
Fixed 15°	0.610	0.78	2.00
Fixed 30°	0.610	0.67	1.47

Table 3.2: Table of wave board speeds, and corresponding wave board accelerations, at which breaking onset occurs.

3.5.2 Breaking Onset

The breaking onset is defined as the slowest wave board speed for which breaking is observed. The exact point of the breaking onset was not determined except that the lowest wave board speed for each category was chosen to be close to, but just greater than, the onset of breaking. Table 3.2 lists the board speeds, and corresponding wave board accelerations, for which breaking was first observed. For the rotating cases (Slap, Mix and Full), the breaking onset appears to occur at a variable wave board speed relatively consistent wave board acceleration of about 1.2 to 1.3 m/s². The Fixed cases appear to have a decreasing breaking onset speed as the angle of attack is increased. The values of the wave board speed for the Fixed cases are of a similar magnitude as the rotating cases, but the corresponding accelerations are generally higher.

The onset of plunging was not explicitly measured in this study because of the

difficulty in objectively determining the transition between spilling and breaking. Although Figure 3.11 appears to indicate a relatively consistent wave board speed at which plunging first occurs, the test points have too large of a gap in wave board speed between them to make an accurate determination of plunging onset. Nonetheless, it can be noted from Table 3.2 that for the rotating cases, the breaking onset occurs at higher wave board speeds with increasing B_w while the plunging onset (see Figure 3.11) appears to occur at seemingly consistent wave board speed ($F_b \approx 0.29$, or $V_b \approx 0.86$). This suggests that the range of board speeds that produce spilling breakers decreases as wave board translation increases.

3.5.3 Jet Impact Point Location

The location at which the plunging jet tip impacts with the upstream water surface (i.e. forward face of the wave) is defined as the jet impact point. The horizontal location of the jet impact point, Y_{impact} , is plotted against F_b in Figure 3.12. Interestingly, there are different trends in the data for the different wave maker motions. For the short-translation motions (Fixed, Slap and Mix 0.2), there is a monotonically increasing relationship between wave board speed and impact distance. However, for the two motions with longer translations, there is either little variation (Mix 0.4) or a monotonically decreasing (Full) relationship with F_b .

To further illustrate this behavior, plots of Y_{impact} , normalized by the waterline translation, versus wave board velocity and acceleration are shown in Figure 3.13. The plot using wave board acceleration (Figure 3.13b) clearly reveals the

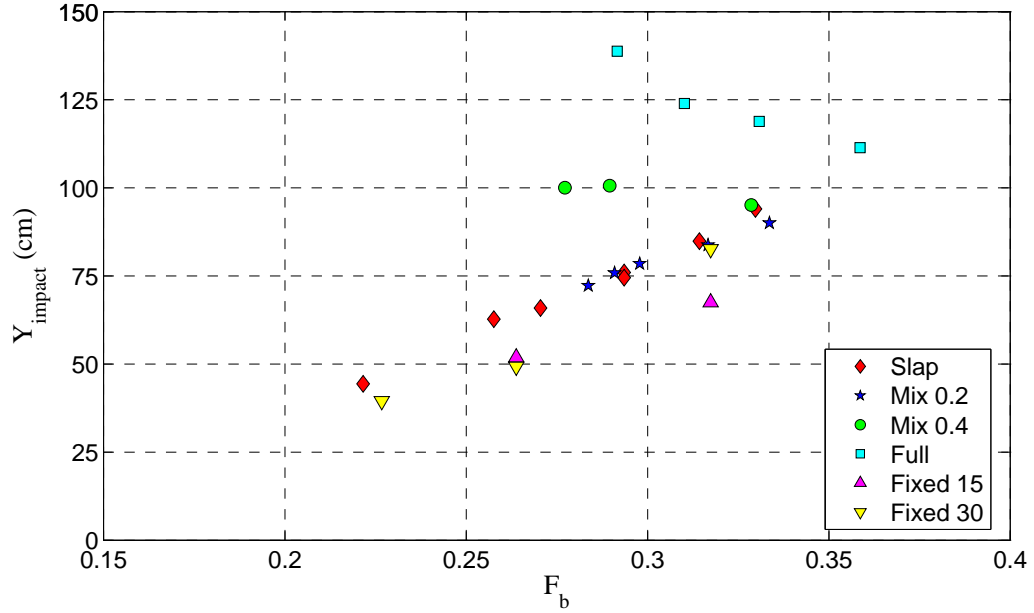


Figure 3.12: Horizontal jet impact point location (Y_{impact}) versus F_b .

two distinct behaviors. The Slap, Mix 0.2 and Fixed case data all have a positive slope with the Slap and Mix 0.2 points forming a fairly tight grouping. The Mix 0.4 and Full cases, however, clearly demonstrate a different behavior with slightly negative slopes.

3.6 Effect of Wave Board Acceleration

As discussed in Section 2.1.2, the standard rounding scheme for the wave maker motions used $T_R = 0.5$. However, in order to investigate the effects of wave board acceleration as an independent variable, i.e. decoupled from wave board speed, the rounding period was varied for a few select cases. Two other rounding periods were used: $T_R = 0.4$ and $T_R = 0.6$. Modifying T_R in this way results in acceleration

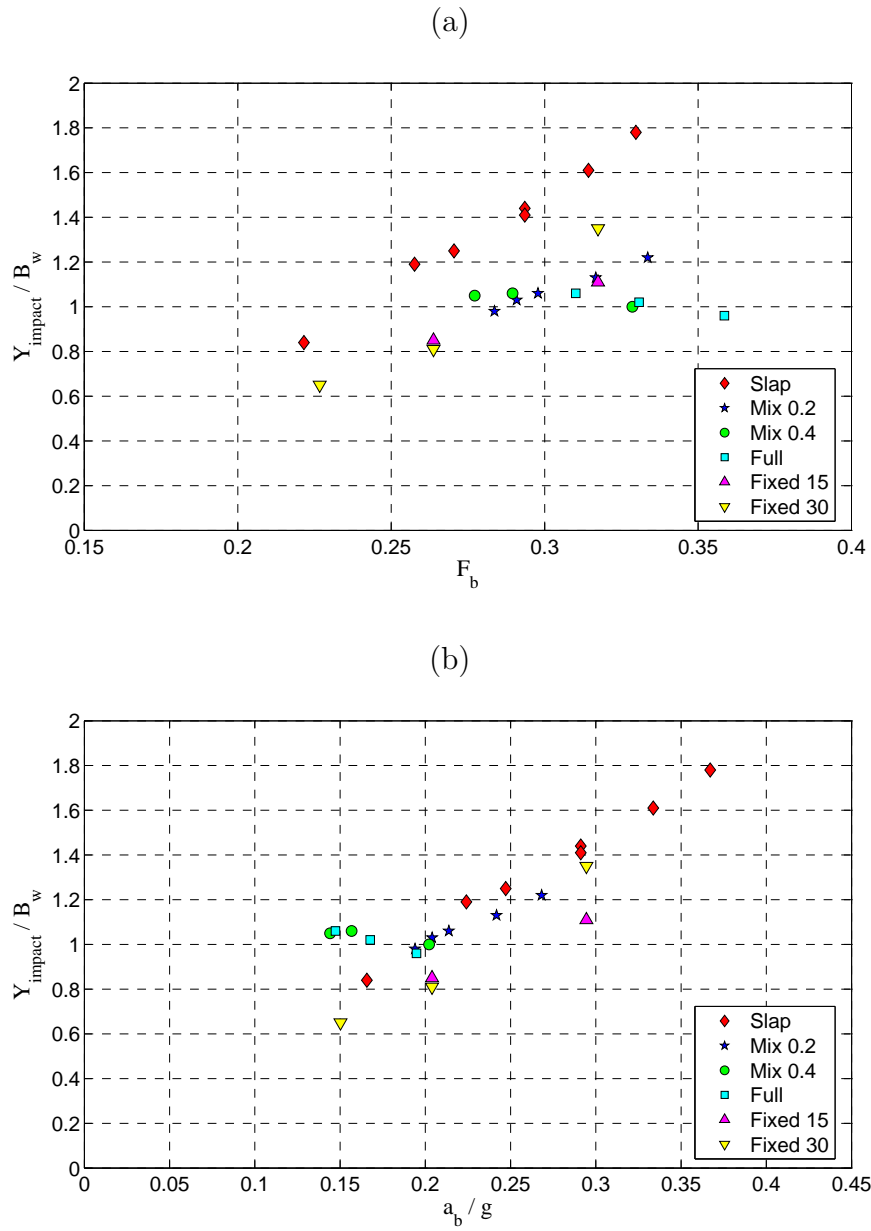


Figure 3.13: Normalized horizontal jet impact location (Y_{impact}/B_w) versus (a) F_b and (b) a_b/g .

values of $1.25a_b^*$ and $0.83a_b^*$ respectively, where a_b^* represents a_b with $T_R = 0.5$. The wave board speed is unchanged for the different accelerations as the rounding period simply affects how quickly the wave board ramps up to the desired speed.

Figure 3.14 shows surface profiles for a Mix 0.2 case ($V_b = 0.94$ m/s) using all three acceleration schemes. Profiles are plotted at the same $1/16$ second intervals. As can be seen from the plot, profiles from the different acceleration schemes deviate during the early stages of the wave (rise along the contact point) but then appear to converge after the wave has detached from the wave board. This is further illustrated in Figure 3.15a, which plots the non-dimensional contact point height versus time and Figure 3.15b, which plots the non-dimensional peak surface height location (i.e. trajectory). In both plots, the three curves are only divergent around the peak contact point location. This behavior was observed among all cases that were tested in this way. Figure 3.16 plots the normalized peak contact point height versus wave board acceleration for the four cases that were tested with varied accelerations. All four cases show a similar increase in peak contact point height with increased wave board acceleration.

While the peak contact point height is clearly affected by the wave board acceleration, the time to reach the peak contact point height (t_{cp}) appears to be relatively unaffected. Figure 3.17 plots t_{cp} against normalized wave board acceleration. As was seen in the Section 3.3, there is almost no variation in t_{cp} .

The effect on impact point location (Y_{impact}) is also plotted in a similar manner in Figure 3.18. Three cases are plotted here (Mix 0.2, $V_b = 0.86$, was not plotted because it did not produce a plunging jet). The data show little variation

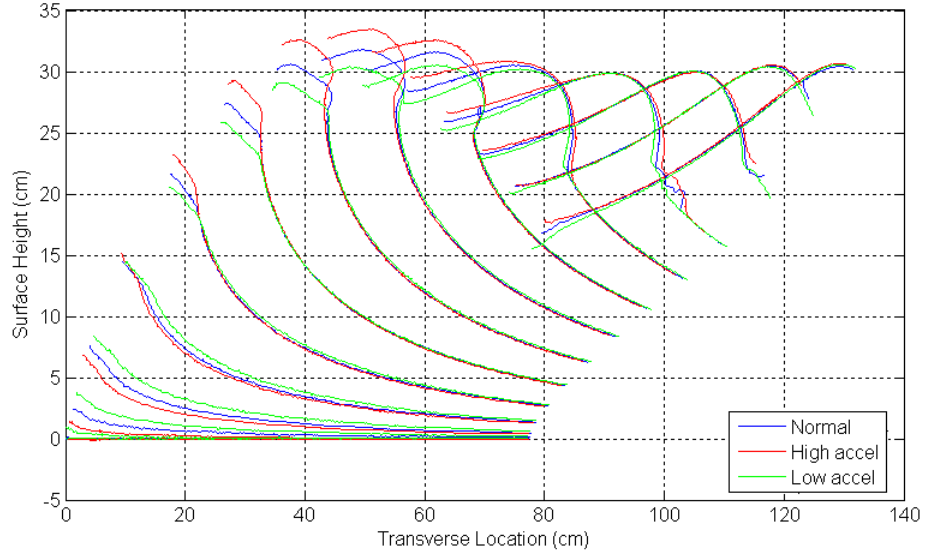


Figure 3.14: Wave profiles resulting for Mix 0.2, $V_b = 0.94$ m/s run with three different acceleration schemes. High acceleration uses $T_R = 0.4$, normal acceleration uses the standard $T_R = 0.5$ and the low acceleration uses $T_R = 0.6$. Profiles are plotted at the same $1/16$ second intervals.

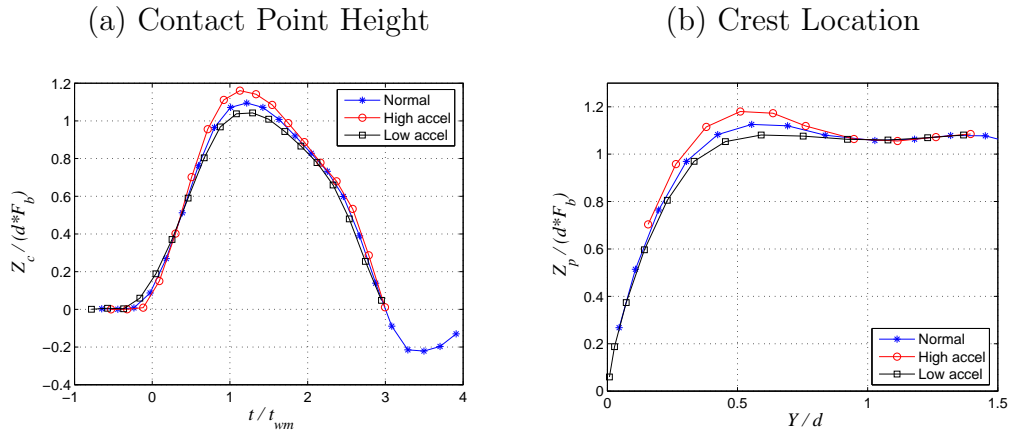


Figure 3.15: Effect of wave board acceleration for Mix 0.2, $V_b = 0.94$ m/s. (a) Non-dimensional contact point heights plotted versus normalized time and (b) normalized peak wave height trajectory.

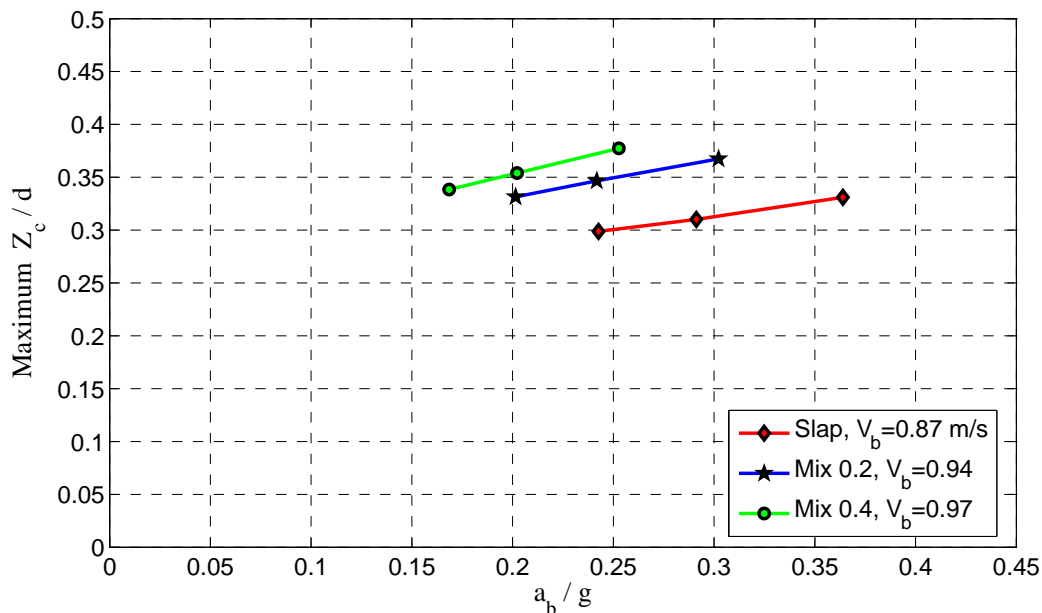


Figure 3.16: Peak contact point heights versus normalized wave board acceleration for cases with varied wave board acceleration parameters.

for the Slap and the Mix 0.2 cases and a decreasing trend for the Mix 0.4 case.

Unlike what was observed for contact point height, there appeared to be no universal influence of wave board acceleration on impact point location.

3.7 Breaker Variability

In general, the waves produced in this study were remarkably consistent and repeatable (recall Section 2.4). However, during testing it was noticed that a few cases occasionally demonstrated some variability. One particular case was the Full profile with $V_b = 0.98$ m/s. Some runs would produce a plunging breaker and other runs would produce a spilling breaker. Figure 3.19 shows three pairs of high-

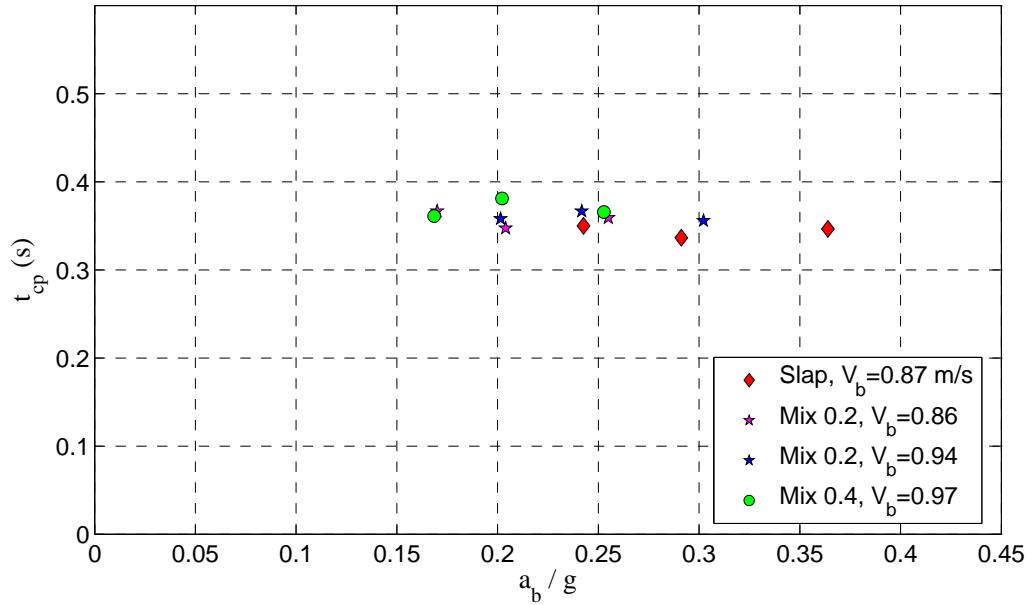


Figure 3.17: Time to peak contact point versus normalized wave board acceleration for cases with varied wave board acceleration parameters.

speed movie frames for two separate runs of this case. The early stages of the waves appeared to be similar ($t = 0.37$ s, images a & b). A little bit later, some waves would develop surface roughness on the forward face of the wave, likely due to the presence of turbulence ($t = 0.52$ s, images c & d). Near the moment of jet impact in the plunging case ($t = 0.62$ s), the wave with this roughness on the front face becomes a spilling breaker (image f) while the other wave develops a clear plunging breaker (image e). Surface profiles of three separate runs of this case plotted at the same 1/16 second intervals (Figure 3.20). In one of the runs, the wave becomes a plunging breaker while in the other two runs the waves become spilling breakers. The early stages the of the wave development appear to be very similar. However, as the wave steepens and approaches breaking, the bulge on the front

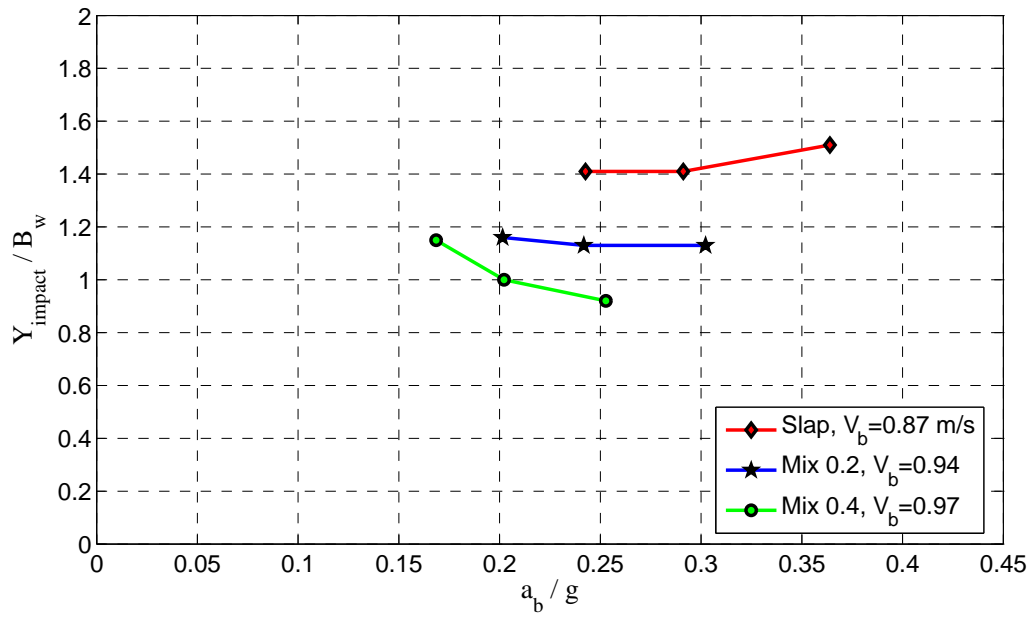
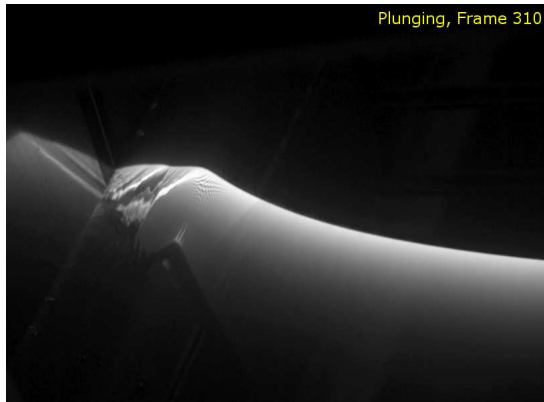


Figure 3.18: Horizontal location of jet impact point versus normalized wave board acceleration for cases with varied wave board acceleration parameters.

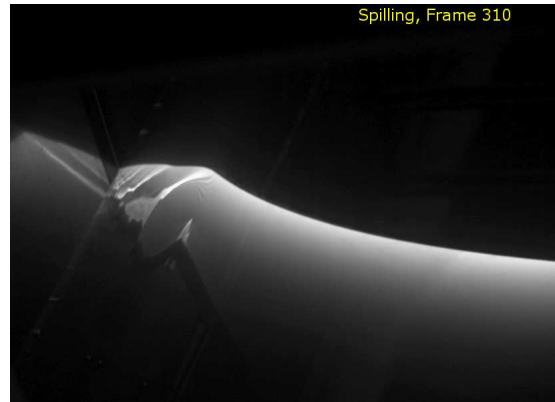
face protrudes further for one of the runs and develops a plunging jet. The surface roughness that develops appears to “trip up” the steepening of the wave and keep it from organizing a plunging jet. This was also observed for two other cases: Full, $V_b = 0.92$ m/s and Mix 0.4, $V_b = 0.86$ m/s. In addition to alternating between plunging and spilling for these cases, the characteristics of the plunging jet, when present, would also tend to be more variable. For example, the impact location (Y_{impact}) for Full, $V_b = 0.92$ m/s, had a variability of ± 9 cm. As a point of comparison, the Slap case with $V_b = 0.98$ m/s, which is a strong plunger, had a Y_{impact} value variability of ± 0.3 cm.

It is interesting that this variability is only observed in the Full and Mix 0.4 cases. Recall that these cases also displayed different behavior with respect to jet impact location. It is hypothesized that these waves may be more sensitive to any slight disturbances on the surface or in the flow field might affect the development of the waves. The wait time between runs was typically about 10 minutes and this was judged to be acceptable for most cases as the repeatability was generally very good. The waves with variability were later re-tested using longer wait times in hopes of achieving more quiescent conditions and thus more consistent behavior. For this, 20 minutes proved to be acceptable. Using this wait time, waves that alternated between spilling and plunging always became consistent plunging waves and more consistent behavior was observed overall. The longer wait time did not have any noticeable effect on any of the Slap, Mix 0.2 or Fixed cases. This increased sensitivity will be discussed further in Chapter 6.

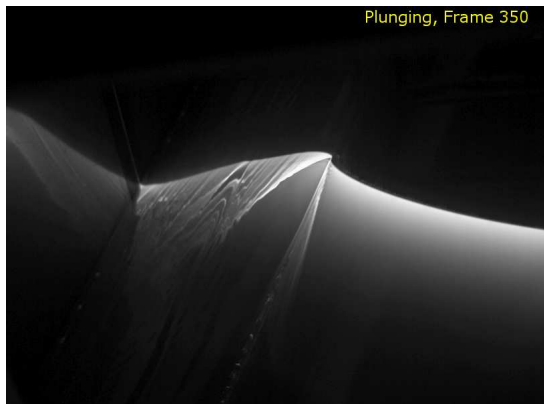
(a) Run 1, $t=0.37$ s



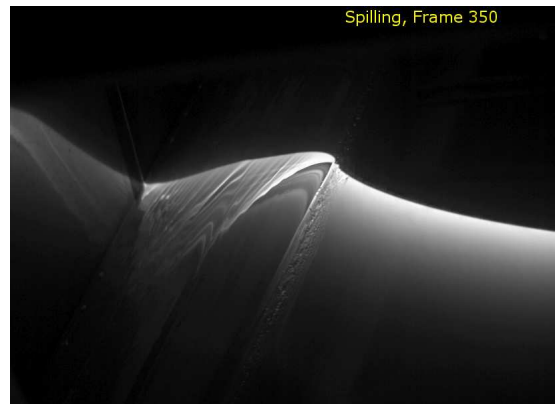
(b) Run 2, $t=0.37$ s



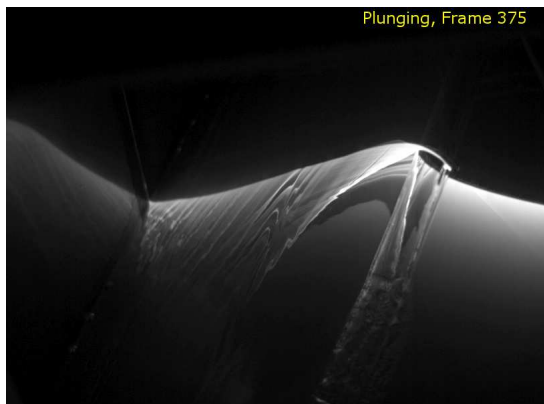
(c) Run 1, $t=0.52$ s



(d) Run 2, $t=0.52$ s



(e) Run 1, $t=0.62$ s



(f) Run 2, $t=0.62$ s

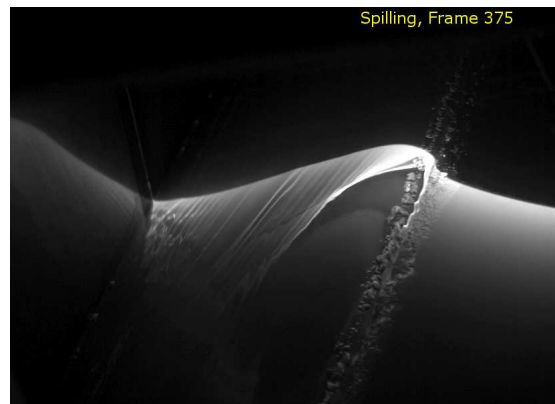


Figure 3.19: Wave images of two separate runs of Full, $V_b = 0.98$ m/s. Run 1 results in a plunging breaker whereas Run 2 in a spilling breaker, even though both runs have identical wave maker motions.

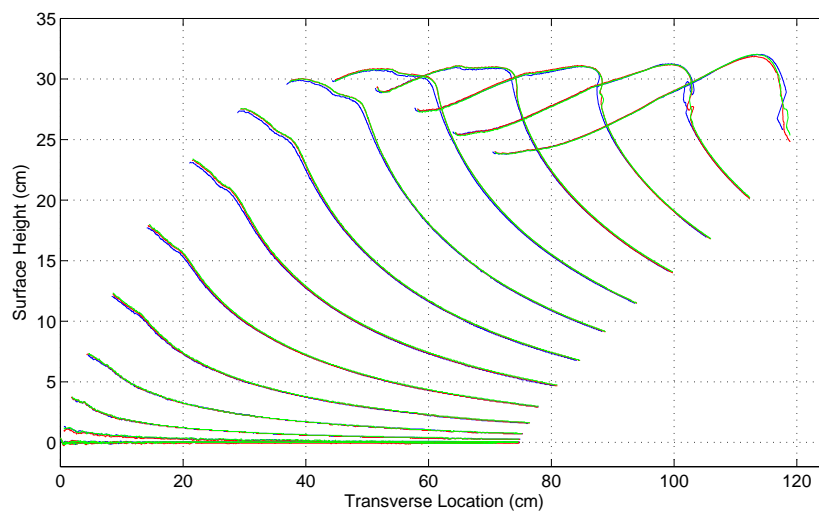


Figure 3.20: Wave profiles from three separate runs (shown as different colors) of Full, $V_b = 0.98$ m/s. One run (blue) develops a plunging breaker while the other two runs (green and red) develop spilling breakers.

Chapter 4

Plunging Jet Characteristics

4.1 Plunging Wave Shape

Several geometric characteristics of the wave were examined at the moment of jet impact (see Figure 4.1). The first characteristic, hereby referred to as “plunging length” (L_{plunge}), is defined as the horizontal distance between the jet impact location and the wave crest at the moment of impact. Figure 4.2 plots plunging length versus wave board Froude number. A wide range of lengths is observed but no functional relationship ship between L_{plunge} and F_b is discernible. However, when the points are plotted against wave board acceleration (Figure 4.3), a linear trend appears among the majority of the points. The jets from the Slap, Mix and Full cases show a monotonically increasing plunging length with wave board acceleration. The jets from the Fixed cases also have increasing length with increasing acceleration but appear to be very dependent on angle of attack as well. The plunging length was also measured for the cases with varied accelerations and plotted in Figure 4.4. A similar trend is observed. The data from these two figures (4.3 & 4.4) form nearly the same curve - note that the middle point for each case on Figure 4.4 is also on Figure 4.2. Thus it appears that the plunging length is strongly correlated with wave board acceleration.

A second shape characteristic analyzed was plunging slope, which is defined

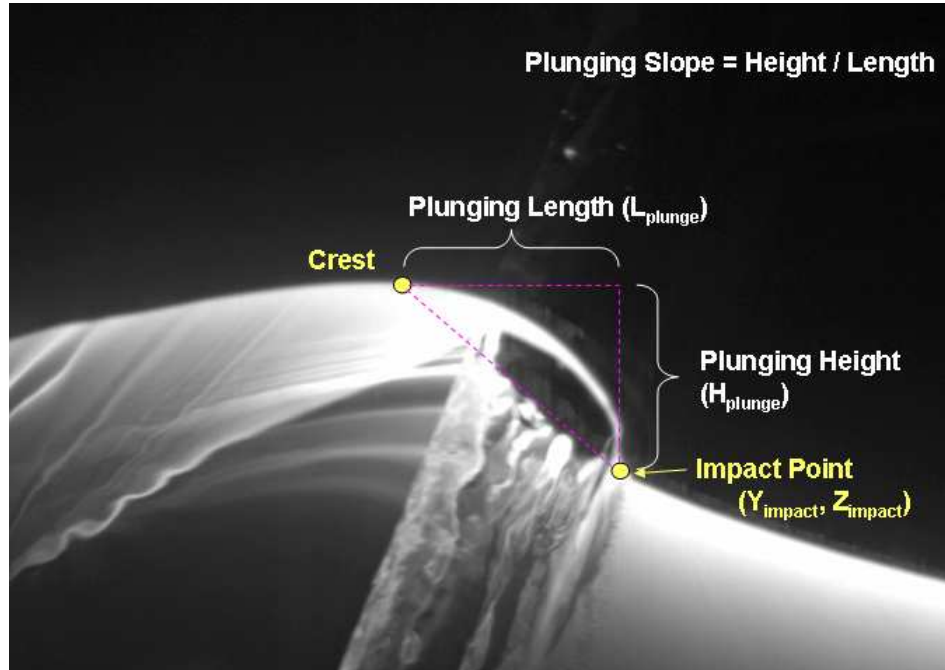


Figure 4.1: Measured geometric characteristics of a plunging breaker.

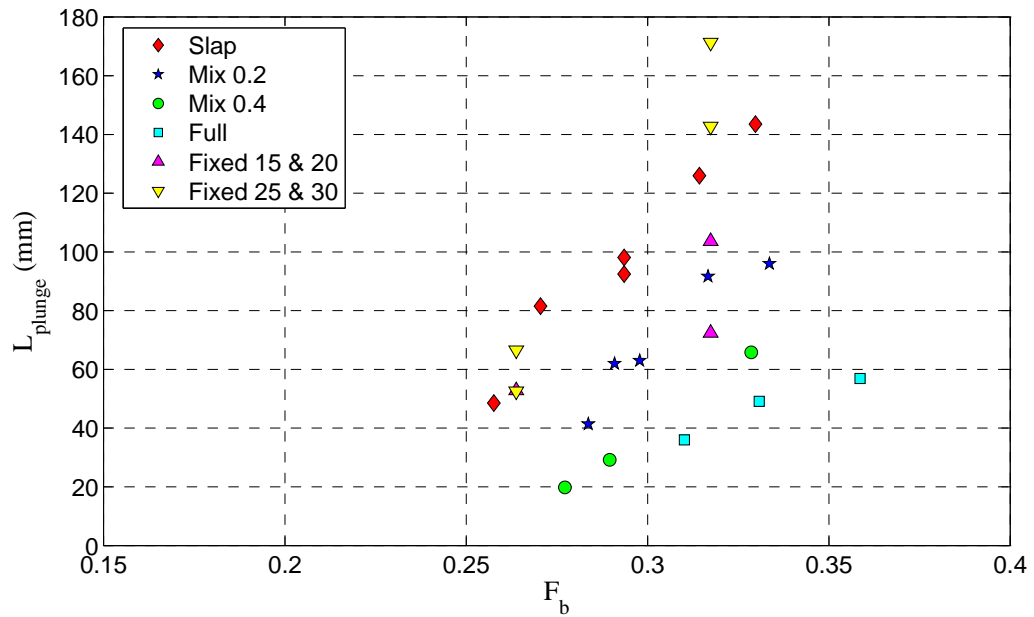


Figure 4.2: Plunging length versus wave board Froude number.

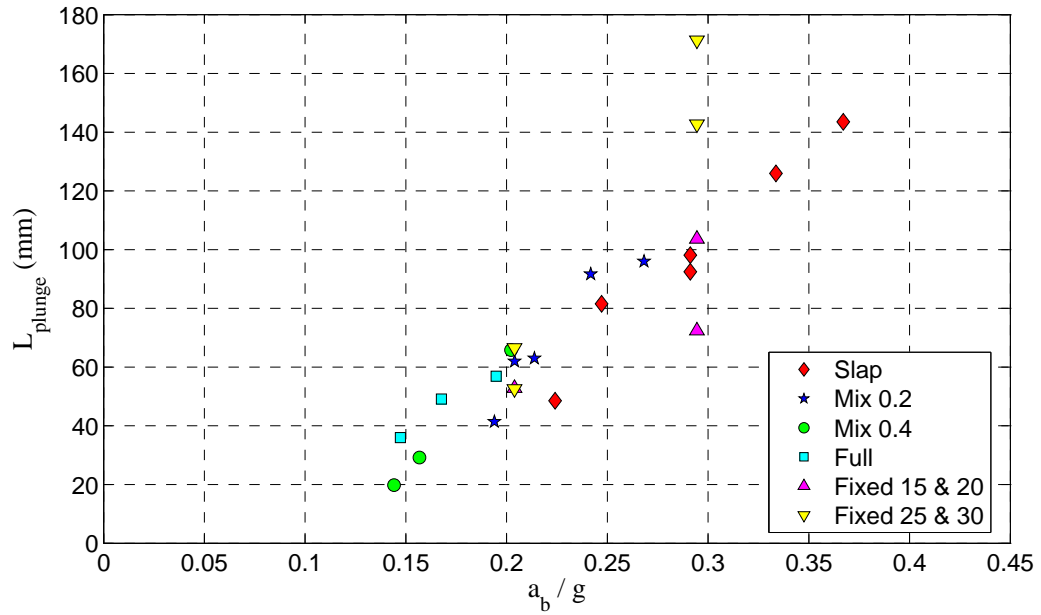


Figure 4.3: Plunging length versus wave board acceleration.

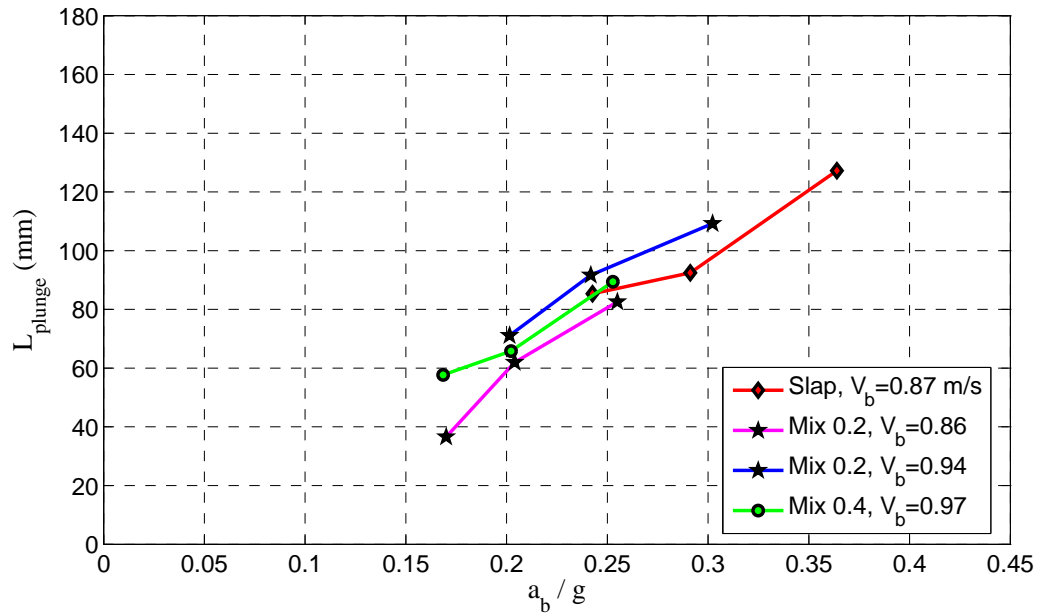


Figure 4.4: Plunging length versus wave board acceleration for varied acceleration cases.

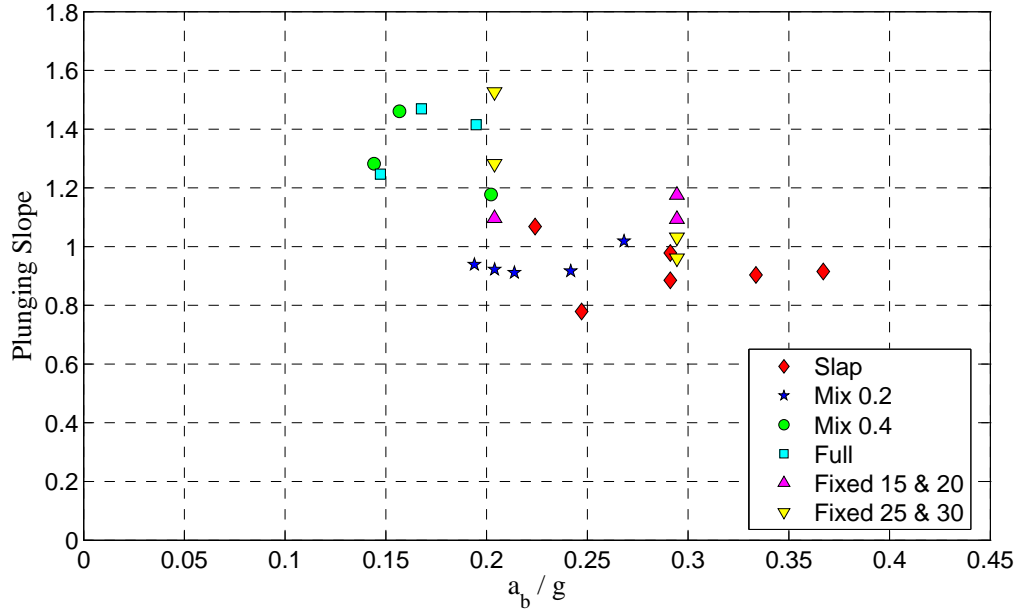


Figure 4.5: Plunging slope versus wave board acceleration.

as the slope (rise/run) of the straight line between the impact location and the wave crest at the moment of impact (see Figure 4.1). A large slope (>1) indicates a steep jet and a small slope (<1) indicates a flat, horizontal jet. Plunging slope is plotted against wave board acceleration in Figure 4.5). While there does not appear to be the obvious linear trends like there were for plunging length, there does appear to be a demarcation between the cases at a value of about 1.1. The jets from the Slap and Mix 0.2 cases all have slopes < 1.1 and the Mix 0.4 and Full cases have slopes > 1.1 . The Fixed cases appear to have a wide range of slopes, similar to what was seen in the plunging length data. Table 4.1 lists the maximum, minimum and average slope values for each motion category. Comparing the average slope values further illustrates the aforementioned groupings.

Category	Maximum	Minimum	Average
Slap	1.07	0.89	0.92
Mix 0.2	1.02	0.91	0.94
Mix 0.4	1.46	1.18	1.31
Full	1.47	1.25	1.38
Fixed	1.53	0.96	1.17

Table 4.1: Table of plunging slope values. Slopes >1 indicate a steeper jet while slopes <1 indicate a flatter jet.

4.2 Jet Tip Trajectory

The trajectory of the jet tip (see Figure 2.9) was examined for all plunging breakers. However, accurately identifying the trajectory proved to be quite difficult as the exact location of the jet tip often was not obvious in the wave images. The jet would sometimes change shape as it plunged and thus a consistent tip could not always be identified. There were many cases where these measurements could not be made reliably. As a result, specific correlations between jet trajectories and wave maker characteristics could not be made although a few several general trends that could be observed.

For the cases in which the jet tip could be identified accurately, the trajectories were determined and appear to be parabolic in nature. Figure 4.6 shows the jet tip trajectories for two Slap cases ($V_b = 0.98$ & 0.87 m/s). From the measured trajectory points, a vertical acceleration of the jet tip can be calculated from the curvature of a fitted second order curve. Figure 4.7 plots the average jet tip vertical acceleration, normalized by gravity, versus wave board Froude number. There was significant

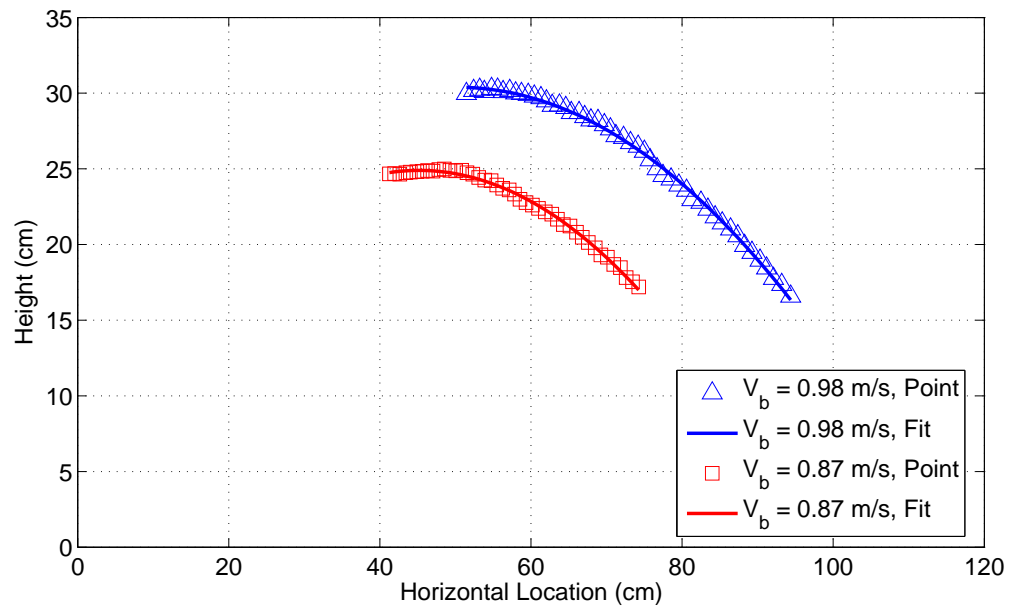


Figure 4.6: Jet tip tracking for two Slap cases, $V_b = 0.98$ m/s and 0.87 m/s. The symbols represent measured jet tip locations and the solid lines are second order curve fits.

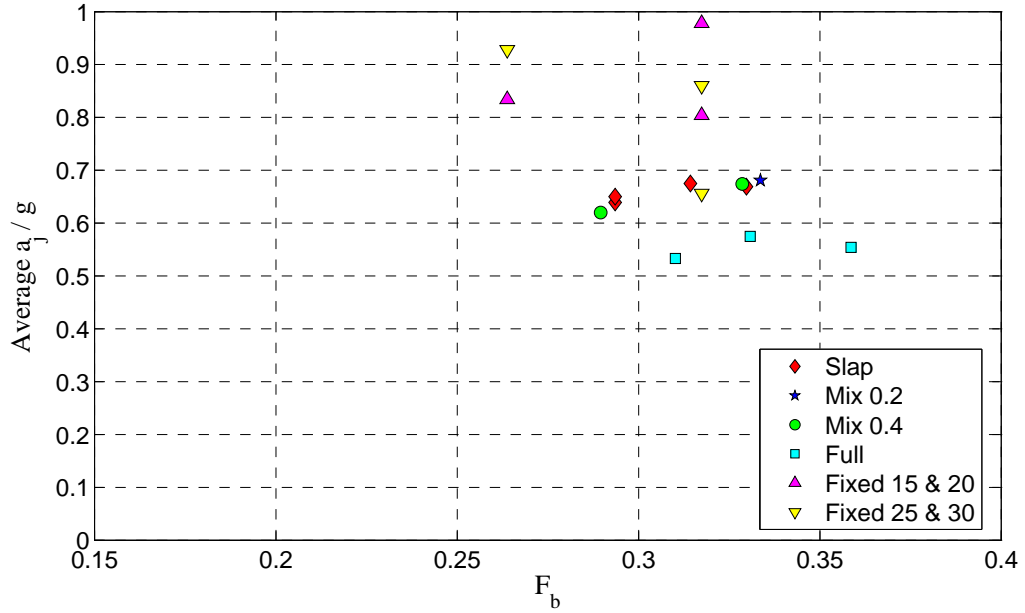


Figure 4.7: Average jet tip vertical acceleration (normalized by gravity) versus wave board Froude number.

variability in the calculated vertical acceleration values so the data was averaged over several runs. The Fixed cases typically had the highest jet acceleration values (average of $0.84g$) and the greatest scatter. The Full cases tended to have the lowest values (average $0.55g$) while the remaining cases were clustered between $0.62g$ and $0.68g$. This range is similar to the results of Shakeri et al. (2009a), which observed a_{jet}/g values of 0.6 to 0.8. Two possible factors resulting in all jet tip accelerations being less than gravity are presented. First, the jet is constantly changing shape and the jet tip is not a center of mass, so it should not be expected to fall exactly with gravity. Second, the jet tip has a tightly curved surface and thus will have surface tension acting as a restoring force serving to pull the tip back into the wave and counteract gravity. These effects will be discussed further in the following chapter.

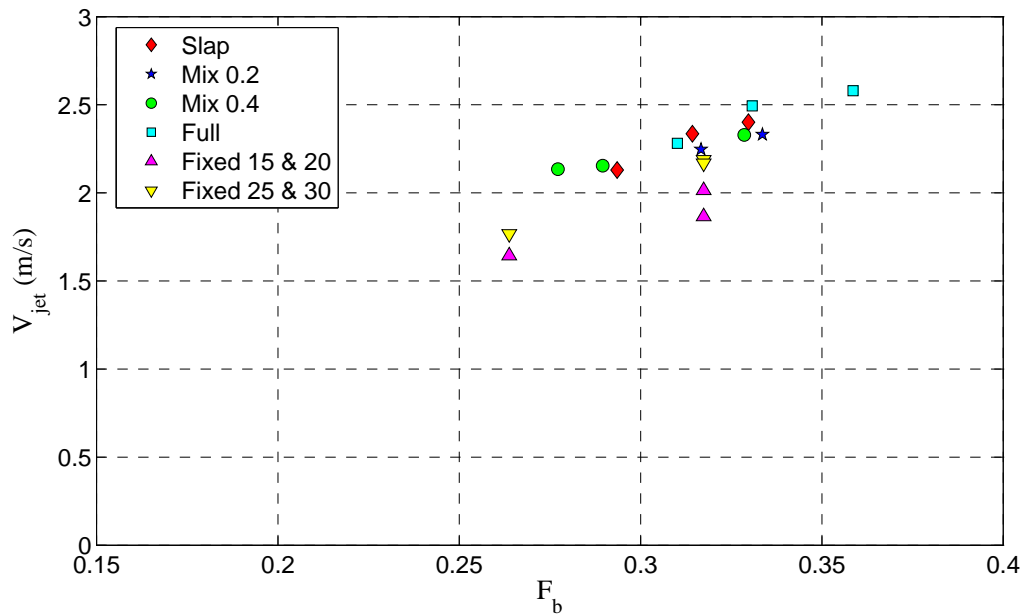


Figure 4.8: Average horizontal jet tip velocity versus wave board Froude number.

The horizontal velocity of the jet tip (V_{jet}) was also determined from the tip trajectories. Figure 4.8 plots the average jet tip horizontal velocity versus wave board Froude number. A monotonically increasing trend is seen for all cases, with the rotating cases forming a noticeable band. A plot of the horizontal jet velocities minus the wave crest speed is shown in Figure 4.9

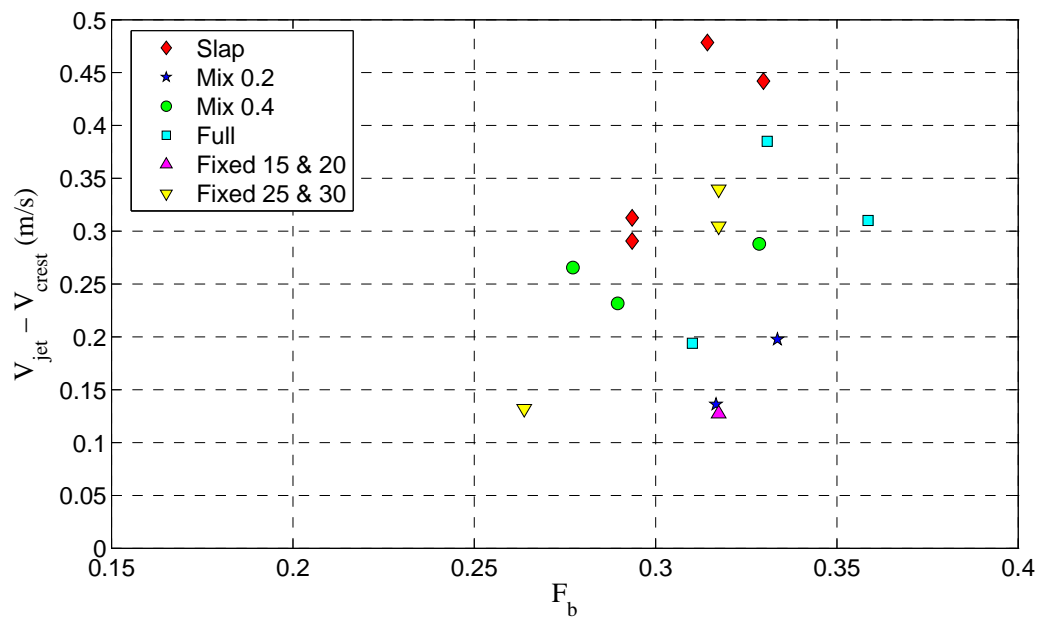


Figure 4.9: Average horizontal jet tip velocity minus crest speed versus wave board Froude number.

Chapter 5

Jet Thickness Measurements

5.1 Measurement Techniques

The defining feature of a plunging breaker is the thin sheet of water that is ejected forward of the wave crest. Despite considerable interest in plunging breakers from coastal engineers, marine engineers and naval architects, very little attention has been paid to the shape and thickness of the jet, especially in the case of ship waves. This is partially due to the difficulty in observing and measuring the jet. In typical towing tank tests, it is virtually impossible to measure the surface profile of the underside of the jet due to limited optical and physical access. However, the views made available through the experimental 2D+T techniques presented in this study offer a unique measurement opportunity.

Figure 2.9 highlights both top and bottom sides of the jet sheet. The intersection of the laser sheet and the upper surface of the jet is viewed entirely through air and thus its profile can be obtained using the techniques already discussed. The intersection of the laser sheet and the underside of the jet, however, must be viewed through the jet and thus its location is distorted due to the refraction of looking through a sheet of water at an oblique angle. To calculate the effect of refraction, Snell's law must be applied. A simplified illustration of this application is shown Figure 5.1 in which a camera is viewing a 2-dimensional slab of transparent material.

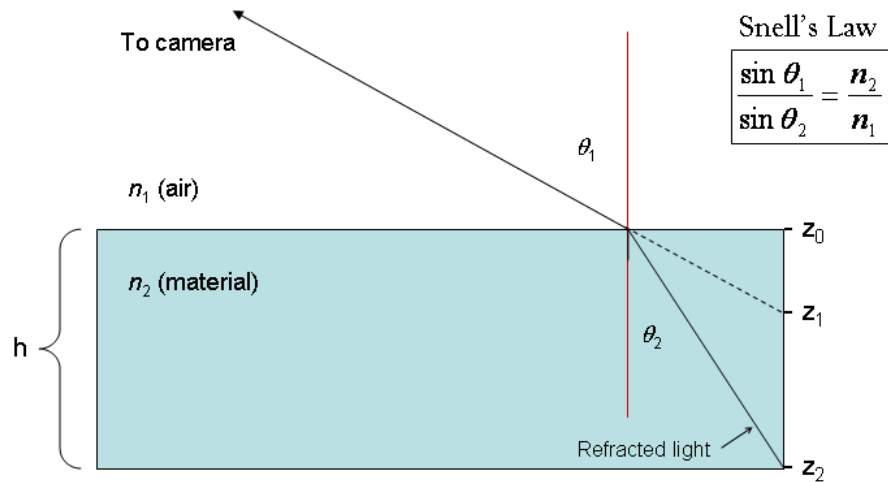


Figure 5.1: Example application of Snell's law of refraction to measure the thickness of a 2-dimensional slab of transparent material. Locations of Z_0 and Z_1 can be measured from the camera image and used to calculate the location of Z_2 .

The underside of the slab is viewed by the camera via a refracted ray of light. This ray of light originates at the bottom edge (z_2) and travels through the material to the upper surface. As it exits the material into air, the ray of light gets refracted according to Snell's law and connects to the camera. If there was no refraction, the ray of light that connects with the camera would connect with z_1 instead and therefore that is where the bottom edge is perceived to be by the camera. The distance between the upper edge (z_0) and z_1 is therefore the perceived thickness. The actual thickness (h) can be calculated, however, with knowledge using only Snell's Law, the index of refraction of the material (1.33 for water) and the locations of the camera, z_0 and z_1 .

If the sheet of water that comprises a plunging jet is thought of as the slab

of material in the preceding example, we can see that its application requires additional consideration of the 3-dimensional geometry involved. Not only does the camera view the plunging jet at an oblique angle, but the jet is a curved sheet of water. In this sense, the plunging jet is similar in shape to a transparent cylinder whose wall thickness represents the thickness of the water sheet. This is illustrated in Figure 5.2. A ray of light originates from a point on the inside edge of the cylinder (P_{in}) and refracts as it pass through a point on the outside edge (P_{out}). The light then continues towards the camera lens. The normal vector (\hat{n}) of the outer surface at P_{out} is used to determine the angle of incidence.

In order to account for refraction through a curved surface, it must be assumed that the surface is perfectly 2-dimensional in the transverse direction. This way, knowledge of the edge profile at any cross-section of the sheet can be used to determine normal angle of the surface at any point on the surface. It is likely that plunging jets are not perfectly 2-dimensional surfaces as disturbances are sometimes observed on the liquid sheet (this will be further discussed in Section 5.8). However, the calculations are not possible without this assumption and thus will be considered as part of the overall uncertainty in the measurements.

A second source of uncertainty comes from the location of the camera relative to the wave. It is desirable to be able to determine this without having to rely on hand measurements in the tank. The crowded space around the camera and the use of a flat mirror on the carriage make this a difficult measurement to make accurately. However, the Matlab software that was used to assist with calibration (Camera Calibration Toolbox for Matlab, www.vision.caltech.edu/bouguetj/calib_doc/),

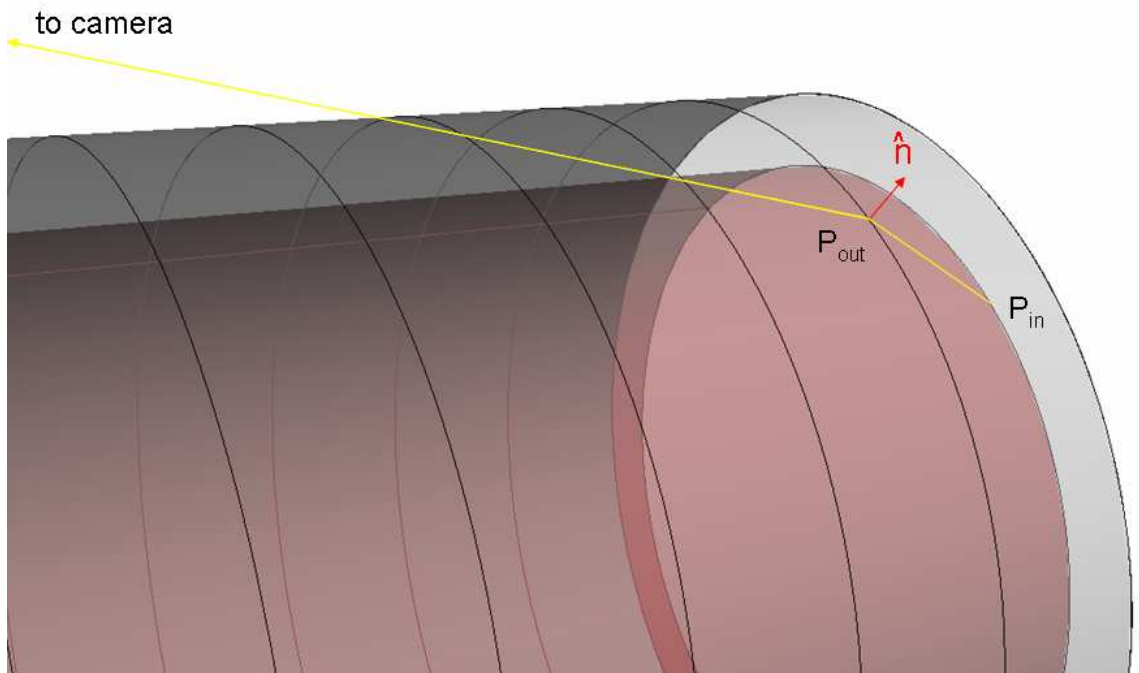


Figure 5.2: Representation of refraction through a cylinder. A ray of light (yellow line) originates at a point on the inside edge (P_{in}), refracts as it passes through a point on the outside edge (P_{out}) and continues to the camera.

includes a function that calculates the camera coordinates relative to the test origin (intersection of undisturbed water surface and initial position of wave board). This method was tested by placing the camera on a table, pointed at a calibration grid, and taking careful measurements of its location relative to the grid. It was found that the software function could determine the camera location to accuracy of about 8% (total location error distance divided by distance between camera and grid origin) for typical configurations. This error in location results in a maximum angular error of about 4 degrees.

In order to assess the accuracy of the imaging system and algorithms, measurements were taken using a pair of lexan cylinders, each with an outside diameter of 6 inches (15.24 cm). The wall thicknesses are 0.25 and 0.5 inches (6.35 and 12.7 mm, respectively). As will be shown later, the thickness of the cylinders is on the same order as the plunging jets, in addition to having similar radii of curvature. The cylinders were placed on a table with various orientations to the camera, and also in the wave tank with a similar orientation to the camera that was used in the imaging of plunging jet. Photographs were taken of the cylinders in all positions (see Figure 5.3) and both the inside and outside edges of the cylinder were traced in the images using the same edge detection algorithm used for the wave images. The actual inside edge location was then calculated using the refraction algorithm (index of refraction for lexan is 1.49). Calculated thickness was determined by taking a calculated inside edge point and finding the distance to the nearest outside edge point. Representative results are shown in Figure 5.4 which shows the edge locations and the corresponding thickness values. The maximum thickness error at any one point

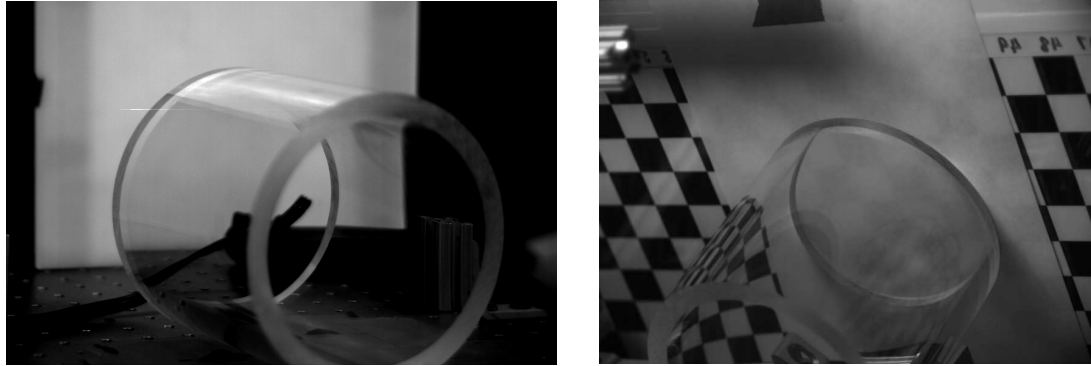


Figure 5.3: Glass cylinder setups used for development and validation of jet thickness measurement techniques.

was about 1.6 mm and the largest average thickness error was 1.4 mm. The largest percentage errors (error/actual thickness) were 25% (maximum) and 17% (average). In some cases, however, average errors were as low 0.1 mm. The magnitude of the error was not significantly different for the two cylinder thicknesses and thus the percentage error typically was less for the larger cylinder thickness. The edge location in the image likely contributes an inherent uncertainty of about 1 pixel due to image pixelation, which equates to about 0.5 mm (recall typical resolution of 2 pix/mm). Based on the tests of the cylinders, it is estimated that if the plunging jets are assumed to be perfectly two-dimensional, the jet thickness measurement procedure should be accurate to about ± 2 mm. This is on the same order of accuracy expected for the surface profile measurements, which will have greater sensitivity to carriage and calibration errors.

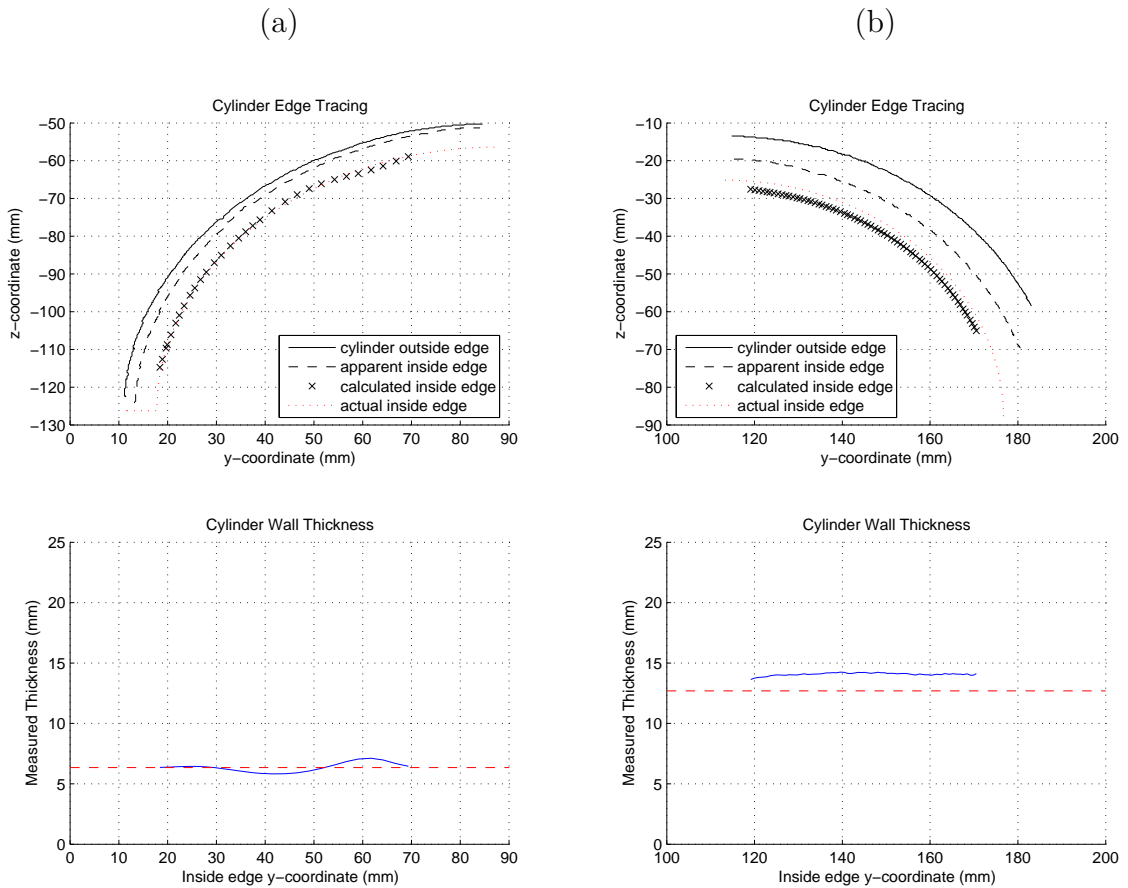


Figure 5.4: Cylinder thickness results for (a) table setup, 0.25 inch wall thickness and (b) in-tank setup, 0.50 inch wall thickness. The upper plots show the measured and calculated edge locations and the bottom row shows the calculated thickness values. Red dashed line on thickness plots indicates the known thickness of the cylinder. The x and y coordinates are with respect to an arbitrary origin.

5.2 Thickness Results

The thickness algorithms were applied to the plunging waves produced in this study. For consistency, jet thickness measurements were always performed at the time of jet impact. Results of these calculations for two cases are shown in Figure 5.5. For each case, a plot is given of the surface profile of the top edge (blue), apparent bottom edge (black) and calculated bottom edge (red). Once the bottom edge is calculated, the thickness (bottom row) is determined by taking a calculated inside edge point and finding the distance to the nearest outside edge point. For the cases presented in this figure, there is a relatively linear tapering of the jet toward the jet tip, which was the general observation for all cases.

5.3 Relations with Wave Maker Parameters

In order to be able to make comparisons among the different cases, the average thickness was computed for each thickness profile. For the cases shown in Figure 5.5, the average thickness values are 9.8 mm (a) and 15.8 mm (b). The average value is not an ideal number in that it is computed from a highly tapered profile and thus the average is quite dependent on the endpoints. The endpoints in this study are determined by what is visible from the image and thus may not necessarily be consistent among the cases or even between runs of the same case. This is not entirely arbitrary, however, in that the lack of visibility beyond the endpoints is due to physical components of the wave (tight curvature at the jet tip and blockage of the rest of the wave near the base of the jet). This was judged to be the most

(a) Full

(b) Fixed

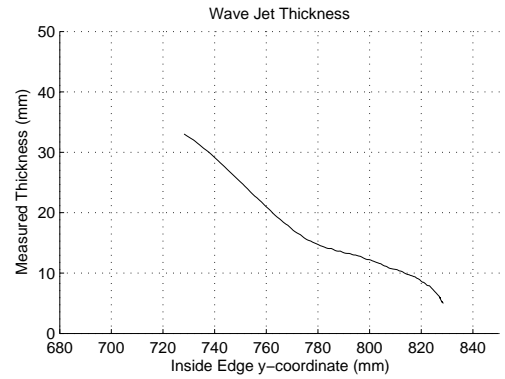
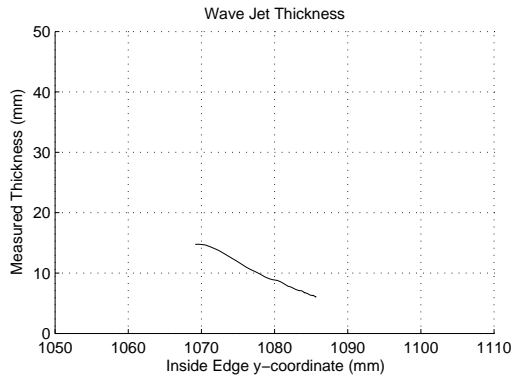
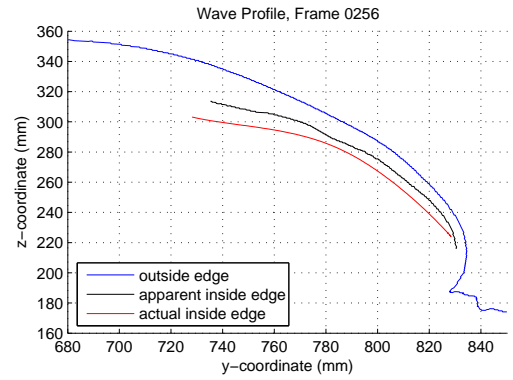
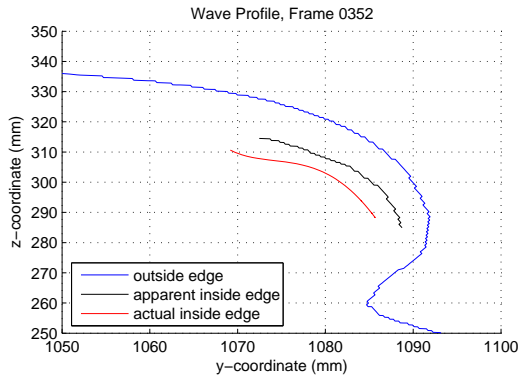


Figure 5.5: Wave thickness measurements results for two cases: (a) Full, $V_b = 1.05$ m/s and (b) Fixed, 30° , $V_b = 0.94$ m/s. The upper plots show the measured and calculated edge locations and the bottom row shows the calculated thickness values. The x and y coordinates are with respect to the test origin.

consistent and objective way of calculating the average thickness. Generally, three different runs were used for each case to obtain three average thickness values which were, in turn, also averaged. Despite the lack of quantifiable consistency among the different cases, it is believed that the jet thickness values obtained will still be useful in identifying wave maker parameters that are important for jet development.

A wide range of average jet thickness values were obtained, ranging from 5.8 to 26.2 mm. The average jet thickness values are plotted against wave board Froude number in Figure 5.6. No particular trends are apparent from this plot so the data were replotted against wave board acceleration in Figure 5.7. When shown in this manner, a strong linear relationship between the jet thickness and wave board acceleration is revealed. The data from the Fixed cases show a strong dependence on angle of attack but still demonstrate an increased jet thickness with increased wave board acceleration.

To further investigate the relationship between jet thickness and wave board acceleration, the thickness values were calculated for the cases of varying acceleration. Figure 5.11 plots these points against the data from Figure 5.7. All cases show a positive slope with increasing wave board acceleration, though the slope of the Slap case data is only slightly positive. The Mix 0.4 varied acceleration points are very similar to the standard acceleration points in both magnitude and slope while the Mix 0.2 varied acceleration points have a slightly flatter slope. The Slap varied acceleration points are too flat to be thought of as demonstrating the same trend as the standard acceleration points, even accounting for ± 2 mm of uncertainty. Thus, the Slap case jet thickness appears to be less dominated by the variations in wave

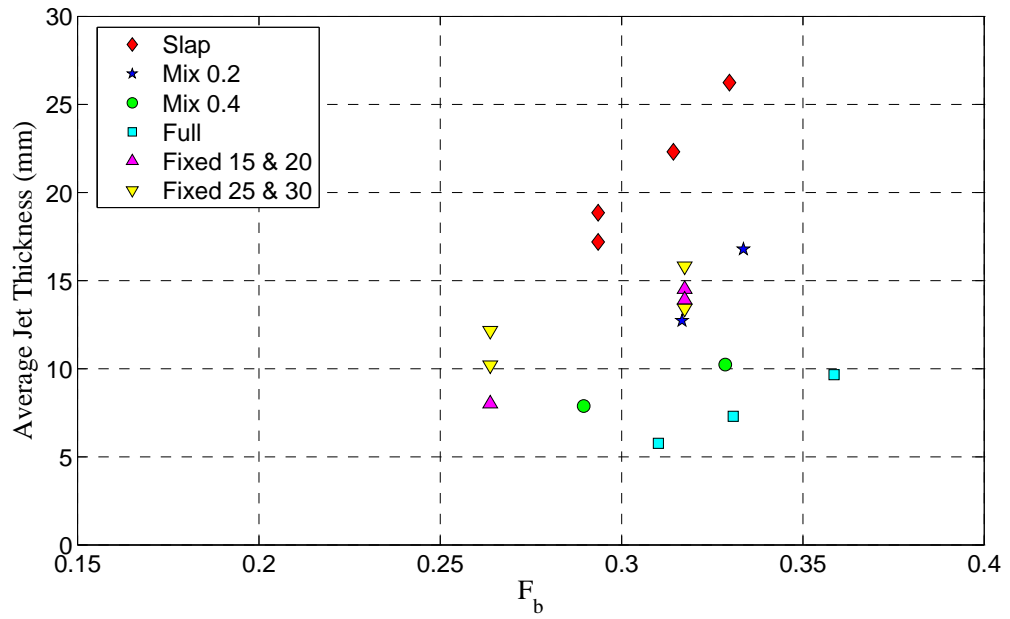


Figure 5.6: Average jet thickness versus wave board Froude number.

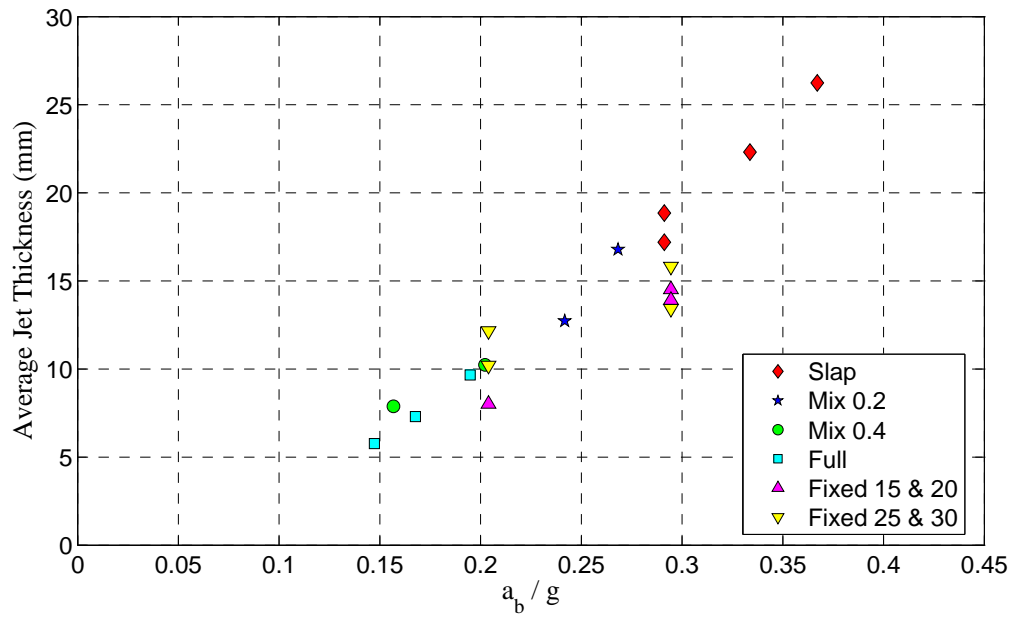


Figure 5.7: Average jet thickness versus wave board acceleration.

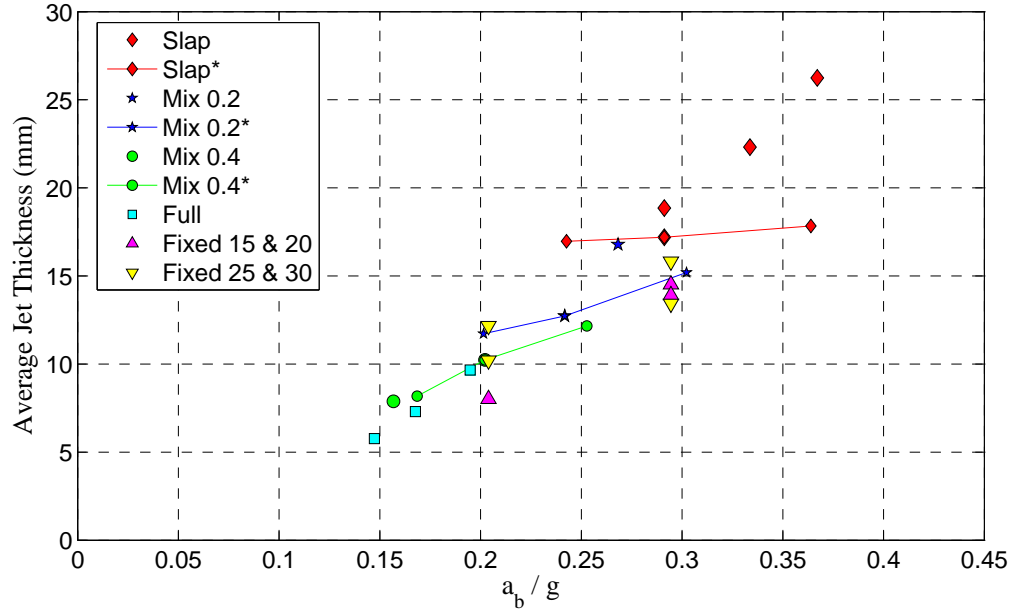


Figure 5.8: Average jet thickness versus wave board acceleration. Note: (*) indicates cases with varied wave board accelerations.

board acceleration as the other rotating cases.

When examining the relationship between jet thickness and wave board acceleration, it is worth considering the effect of the time to peak contact point height, t_{cp} , which was discussed in §3.3. Referring back to Figure 3.6, it is observed that in the Slap cases, contact point reaches its peak height later in the motion i.e. has a greater t_{cp}/t_{wm} , than in the Mix or the Full cases. The Slap case examined in Figure 5.11 ($V_b = 0.87$ m/s) has a contact peak occurring at $t_{cp}/t_{wm} = 0.55$. The Mix 0.2 and Mix 0.4 cases in question from that figure have lower t_{cp}/t_{wm} values of 0.46 and 0.39, respectively. This means that for the Slap cases, the wave continues to develop for a longer portion of wave maker motion after the acceleration ceases ($t = 0.25t_{wm}$ for the standard acceleration cases) before detaching at $t = t_{cp}$, as compared to the

Mix cases. Thus, for the Slap cases, a greater portion of wave development occurs when the wave board is at constant speed and thus the jet thickness appears to be less strongly influenced by wave board acceleration.

5.4 Comparison with Other 2D+T Waves

A separate set of tests were run using the 5415 hull wave maker motions (see Shakeri et al. 2009a) and corresponding test conditions. The two highest speeds were used to produce strong plungers which were photographed in order to calculate jet thickness values. Figure 5.9 adds the resulting data points for two test speeds to what was shown in Figure 5.7. Because these tests used a very different wave maker motion, the wave board acceleration values for the 5415 data were approximated to be as equivalent possible to the values of a_b from the present study. This was a subjective approximation, however, and the two sets of a_b values are probably not identically defined. Nonetheless, the thickness values from the 5415 data are similar in magnitude as the Slap case waves and the two points form a slope similar to that for the rotating cases.

5.5 Comparison with Shoaling Waves

Miller (1976) examined a set of plunging breakers created in a laboratory tank that simulated waves breaking on the surf zone. The study produced several excellent photographs of the breaker in which both sides of the plunging jet are clearly visible through the glass sidewalls of the tank. Using images from that

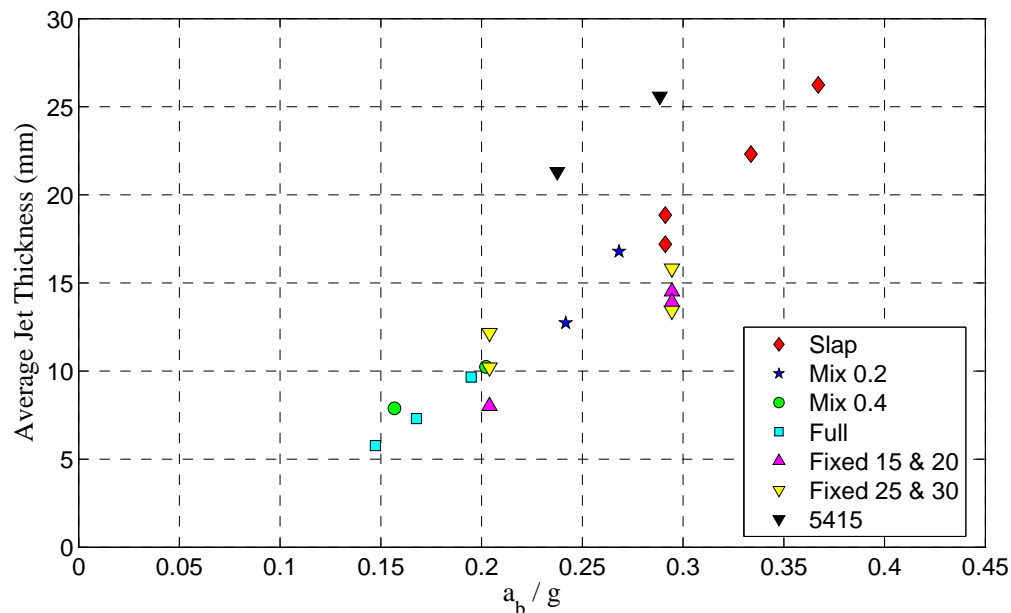
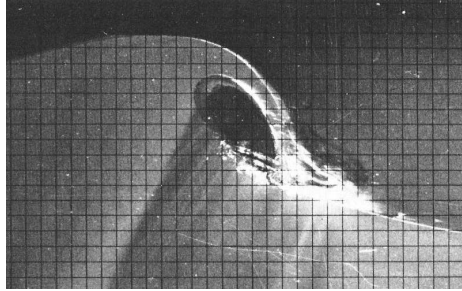


Figure 5.9: Average jet thickness versus wave board acceleration, including data from 5415 hull wave maker motion.

study, surface profiles were traced by the present author and the jet thickness was determined for this wave (Figure 5.10). The most similar wave from the present study in terms of size and shape is the Full case with $V_b = 1.05$ m/s, which is also shown for comparison. The Miller wave, which is slightly larger, has a slightly thicker jet and more gradual taper. Because the 2D+T setup does not allow for tracing of the entire inside edge of the jet, it was estimated that the equivalent edge tracing on the Miller wave would likely start around $x = 80$ mm in the middle plot of Figure 5.10a. Using this as the starting point, the average jet thickness is 11 mm, compared with 9.7 mm for the 2D+T wave. Thus, the two waves appear to have similar jet thickness characteristics.

(a) Shoaling



(b) 2D+T

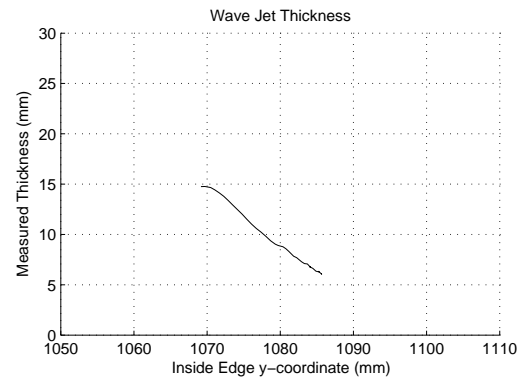
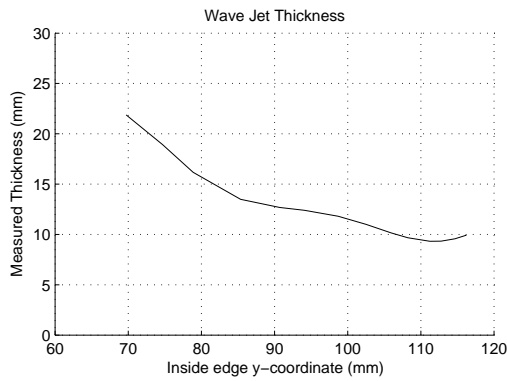
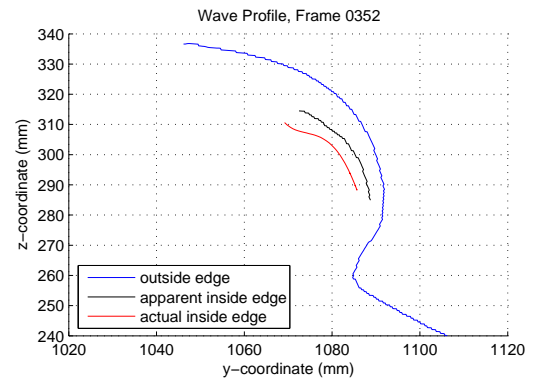
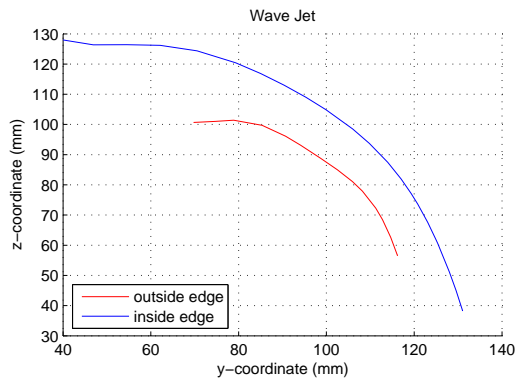
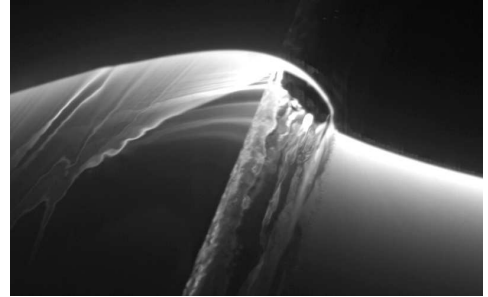


Figure 5.10: Comparison of jet thickness calculations for (a) shoaling wave (from Miller 1976) and (b) the present study (Full, $V_b = 1.05$ m/s). The x and y coordinates are with respect to an arbitrary origin for (a) and to the test origin for (b).

5.6 Relationship with Jet Tip Acceleration

In §4.2, it was observed that the vertical acceleration of the jet tip was consistently less than gravity. One possible explanation for this is that the surface tension forces in the region of high curvature in the jet tip acting as a restoring force and trying to pull the jet back into the rest of the wave. The thinner jets would presumably have greater curvature at the tip and also have less momentum in the jet fluid to overcome any surface tensions, so it might be expected that the thinner jets would also demonstrate lower vertical tip accelerations. As a means of exploring this, jet tip acceleration values were plotted as functions of average jet thickness in Figure 5.11. Among the rotating cases (Slap, Mix and Full), there does appear to be a slightly positive relationship between tip acceleration and jet thickness. However, as previously discussed, there was considerable difficulty measuring the jet tip accelerations reliably. As such, it is difficult to draw conclusions from Figure 5.11 at this time.

5.7 Sheet Tapering

The tapering of the plunging jet is something that seems to be taken for granted in most wave studies and is generally not studied in great detail. Because the plunging jet is an accelerating sheet of fluid, an obvious flow to compare the measured thickness profiles with is that of a steady vertical sheet falling due to gravity. Using a simple inviscid analysis where a fluid falls through a vacuum at the acceleration of gravity and using time (t) as the independent variable, the thickness

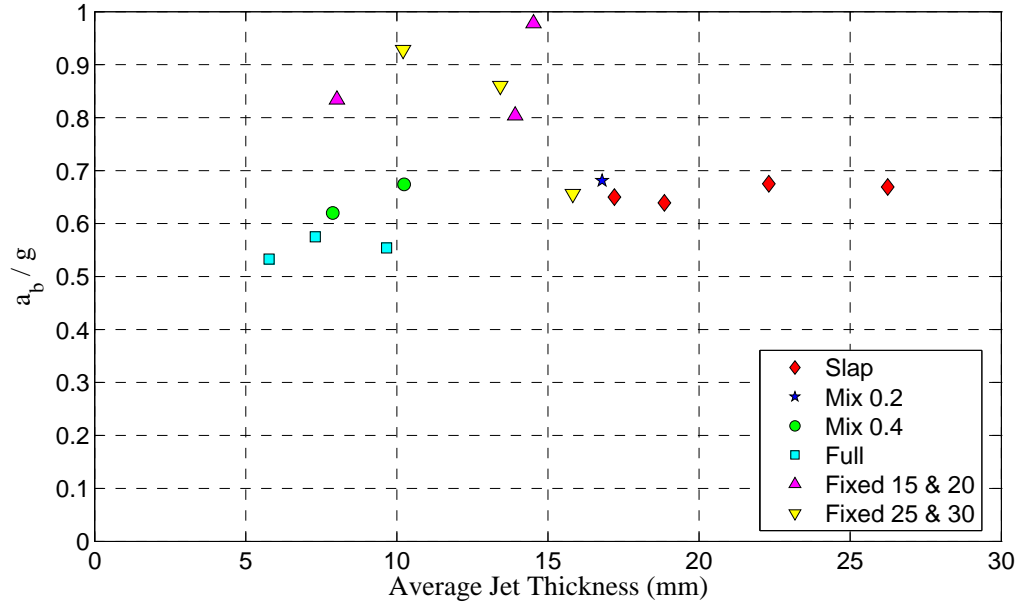


Figure 5.11: Average vertical jet tip acceleration versus average jet thickness.

profile behaves as such:

$$\begin{aligned}
 U(t) &= gt + U_0, \\
 z(t) &= \frac{1}{2}gt^2 + U_0t, \\
 h(t) &= \frac{h_0U_0}{U(t)},
 \end{aligned} \tag{5.1}$$

where U is the sheet velocity, z is the vertical distance from origin, h is the sheet thickness and U_0 and h_0 are the initial values of velocity and thickness, respectively. In order to compare a falling sheet with a plunging jet, corresponding values of U_0 and h_0 and must be determined. For this analysis, the crest of the wave shall be considered the source of the jet and thus the horizontal jet tip velocity (V_{jet}) minus the crest speed (V_{crest}) is used for U_0 (recall Figure 4.9). The jet thickness value closest to the base of the jet (nearest to the crest) is used for h_0 .

Figure 5.12 plots the thickness profiles versus the jet tip vertical coordinate for three cases: Slap ($V_b = 0.98$ m/s), Full ($V_b = 1.05$ m/s) and Fixed ($V_b = 0.94$ m/s). Images of each of these waves at the moment of jet impact are shown in Figure 5.13. The thickness profiles from corresponding vertical sheets are shown in this plot as dashed lines of the same color. There are definite similarities in the two sets of thickness profiles. The rate of tapering and the curvature are all of similar magnitudes. This is especially interesting because of the obvious differences between the systems. The falling vertical sheet is a steady state system whereas the wave jet is a very non-steady flow and has varying input conditions as the part of the wave which is feeding the jet is changing. Both the assumed values of U_0 and h_0 are therefore likely to not be constant. Even with all these obvious differences between the two systems, the tapering of the thickness profiles are still similar enough to suggest the same mechanism may be dominant.

5.8 Sheet Instability

As noted in §4.2, the Fixed cases produced the largest vertical acceleration values in the jet tip, often approaching that of gravity. Looking back at Figure 3.2 and comparing the Fixed, 30° , wave (image f) with the other waves, one can see that the Fixed wave has a very elongated jet. When this jet is examined closer, evidence of “fingering” becomes visible (see Figure 5.14. According to Longuet-Higgins (1995), perturbations in the form of transverse waves on the top surface of the jet develop into capillary waves that increase in amplitude relative to the stretching and thinning

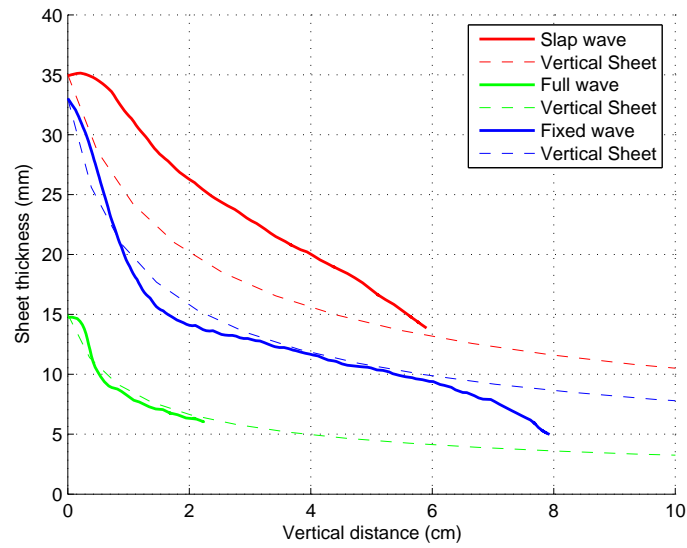
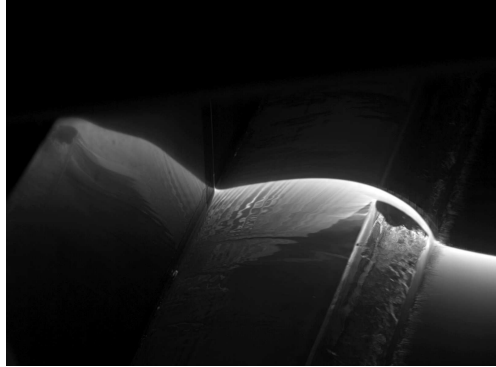
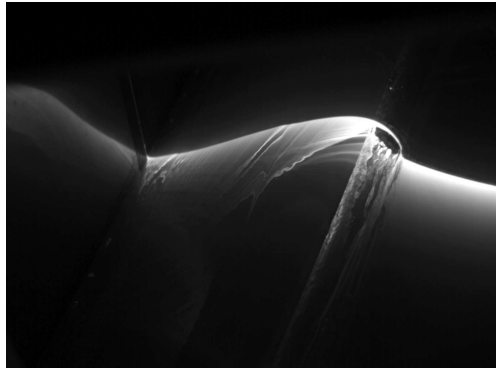


Figure 5.12: Thickness profiles for Slap ($V_b = 0.98$ m/s), Full ($V_b = 1.05$ m/s) and Fixed ($V_b = 0.94$ m/s) compared with corresponding vertical falling sheet (dashed lines of same color). For the 2D+T wave curves, the vertical distance is taken as the vertical coordinate of the bottom edge of the jet.

(a) Slap, $V_b = 0.98\text{m/s}$



(b) Full, $V_b = 1.05\text{ m/s}$



(c) Fixed, $V_b = 0.94\text{ m/s}$

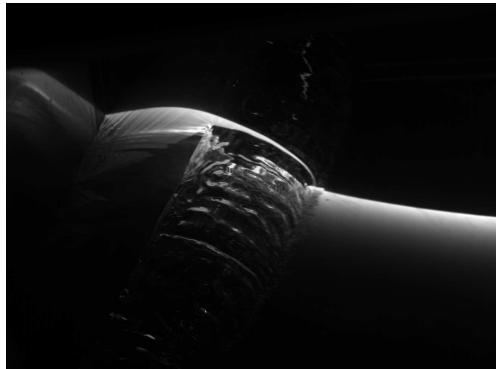


Figure 5.13: Wave images at moment of jet impact for waves analyzed in Figure 5.12. (a) Slap ($V_b = 0.98\text{ m/s}$), (b) Full ($V_b = 1.05\text{ m/s}$) and (c) Fixed ($V_b = 0.94\text{ m/s}$).

of the sheet. The amplitude of the transverse waves eventually becomes large enough to pinch off the sheet into drops and result in sheet breakup. It is reasonable to hypothesize that as the wave jet approaches breakup and the wave structure becomes compromised that the restoring force at the jet tip due to surface tension is lessened because the jet is unable to maintain a hold of the fluid at the tip. As the tip breaks into drops, the fluid is able to fall according to gravity. Because the fingering is a three-dimensional phenomena, the sheet would not be uniform and thus different transverse locations of the sheet would yield different tip acceleration values, which would help to explain the greater variability of the Fixed case acceleration values seen in Figure 4.7. The fingering was occasionally observed in other cases but it was never as prominent as in the Fixed cases.

Waves that develop on a liquid sheet were described by Taylor (1959) as being symmetric or antisymmetric (Figure 5.15). It is unclear if the disturbances visible in Figure 5.14 are waves (capillary or gravity) or if they are even regular because of the angle of view and the orientation of the laser light sheet. Previous studies on liquid sheets that have investigated sheet instabilities (see Lin 2003) have typically done so on expanding liquid sheets and low Weber number flows (≈ 1). The Weber number:

$$We = \frac{\rho U^2 H}{S}, \quad (5.2)$$

where H is the jet thickness and S is the surface tension, is on the order of 300 - 2,000 for the plunging jets in this study (using average jet thickness as H).

Huang (1970) studied the phenomena of sheet break-up of axisymmetric sheets

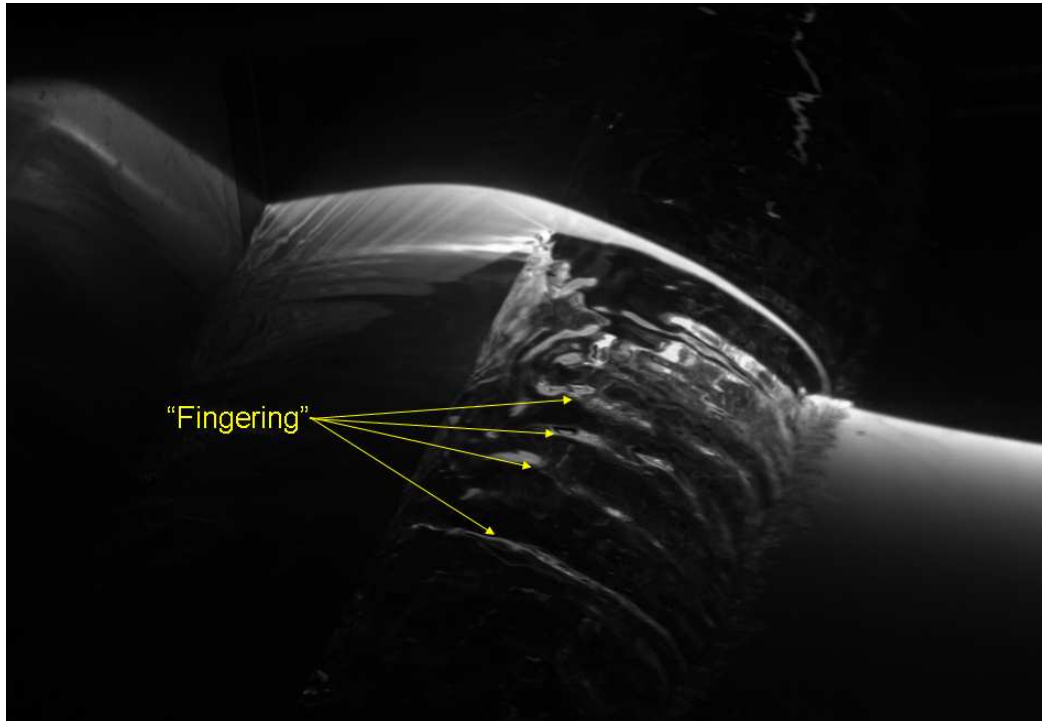


Figure 5.14: Wave image of Fixed case (30° , $F_b=0.317$) showing transverse striations.

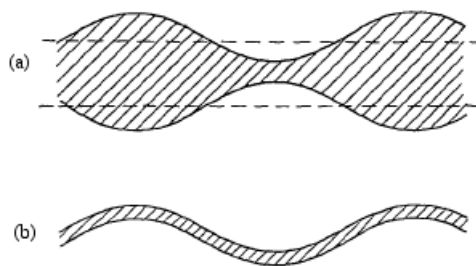


Figure 5.15: Sketch of (a) symmetric and (b) antisymmetric waves on a sheet of thin fluid (from Taylor, 1959).

and looked at Weber numbers ranging from 100 to 30,000. That study found distinct instability and break-up regimes as a function of Weber number. Interestingly, a transition region between the two primary break-up regimes exists for Weber numbers of about 500 to 2,000. The first region ($We < 500$) is dominated liquid beads along the edge or developing a cusp-shaped edge but is otherwise relatively stable. The second region ($We > 2,000$) is marked by large amplitude antisymmetric waves. The Fixed case waves, with relatively thin jets, tend to have Weber numbers below 1,000 and thus do not enter the region where antisymmetric waves are expected. As such, it appears as though the disturbances of the plunging waves are of a different mechanism. Nonetheless, a different experimental setup would be required to properly measure the shape and pattern of the observed disturbances and relate them to both jet break-up and other characteristics of the plunging jet.

Chapter 6

Breaking Modes

6.1 Observation of Breaking Modes

The aim of this study has been to find relationships between a series of parametric flat-plate wave maker motions and various characteristics of the resulting waves. The wave maker motions were designed to be as simple and quantifiable as possible. However, even with all the simplifications used, there is still considerable complexity in the flow problem. As discussed in §2.1.3, the wave maker motions in this study can be completely described by six independent variables. Although various combinations are possible, one set is: wave maker run time (t_{wm}), rounding period for the acceleration/deceleration (T_R), waterline translation (B_w), bottom translation (B_k), initial wave board angle (α_0) and wave maker draft (d). In order to fully define the physics of wave generation for this system, gravity (g) will also be needed, and possibly other variables such as viscosity and surface elasticity. Therefore, to describe a simple problem like peak water surface height (Z_p), for example, there are at least eight variables and two dimensions (length and time) which, according to Buckingham pi theory, requires six different dimensionless variables to fully describe the resulting surface heights from this set of wave maker motions. Thus, a seemingly simple and parametric set of wave maker motions quickly becomes a very complex problem.

In reality, there are infinite combinations of possible wave maker parameters and wave characteristics. Much of the analysis of this study has involved relating various wave characteristics to particular wave parameters in hopes of learning more about the relative influence of such parameters on the wave shape. Often, a linear relationship was observed between a wave characteristic and a single wave parameter. This indicates a strong influence by that parameter, even though it is highly unlikely that any one single parameter is solely responsible for an entire aspect of the wave shape. This section seeks to step away from the quantitative relationships with wave maker parameters and explore more qualitative descriptions of the waves observed. It is believed that many of the phenomena observed in the waves from this study are indicative of universal water wave behavior that would be found in many other wave systems.

Throughout this study, analysis of a number of wave characteristics have indicated fundamentally different behavior among the waves generated by the various wave maker motion categories. This was seen in the analyses involving contact point tracking, crest time histories, impact location, plunging length and plunging slope. It is proposed that there are a range of breaking behaviors ranging between two extreme distinct modes, hereby referred to as “overdriven” and “developing”. Purely overdriven behavior is characterized by wave breaking occurring adjacent to the wave board before the peak contact height has been attained. Purely developing behavior is characterized by wave breaking occurring farther away from the wave board, after the contact point has dropped well below the wave crest height. The developing wave takes on the appearance of a freely propagating wave in that a fully

developed crest and trough (behind the wave) are present whereas the overdriven wave breaks before the wave is able to form such features. This section will further describe the identifying characteristics of the two modes and what are believed to be the underlying mechanisms that create these modes.

In the present study, the overdriven mode was observed in the Slap, Mix 0.2 and Fixed cases while the developing mode was observed in the Full and Mix 0.4 cases, with the two Mix cases tending to be closer to intermediary points between the two modes. To illustrate the behavior of the modes, contour plots of a Slap case and Full case are presented in Figure 6.1. Surface profiles taken at 1/16 second intervals were plotted at uniformly offset intervals along the y-axis (vertical offsets on the plot), similar to the way Figure 1.5 was constructed, and filled to create contour plots that simulates an overhead view of the wave field created by a passing ship. The solid white line indicates the transverse location of the contact point at any given longitudinal location. The red line indicates the waterline displacement of the wave maker at any given longitudinal location. Both of these lines are representations of the notional hull form. The jagged appearance of the wave pattern edges is due to the relatively large time intervals between wave profiles. The Slap case, (a), which is strongly overdriven, has peak water surface heights located very close to the notional hull, which is shown by the dark red contours being clustered in an area adjacent to the hull. The Full case, (b), creates a developing wave that reaches its peak height further way from the hull, which is shown by the dark red contours being located away from the hull. In this case, the wave has detached from the hull before it reaches its peak height. As seen in both cases from the movies, the wave

breaks around the time the wave reaches its peak height.

6.2 Mechanics of Breaking Modes

Figure 6.2 illustrates the proposed mechanics of the two modes. A series of surface profiles are plotted at 1/8 second time intervals for two cases: (a) Slap, $V_b = 0.94$ m/s and (b) Full, $V_b = 0.98$ m/s. The normalized time is defined by $t^* = t/t_{wm}$. In the overdriven mode, which is observed in the Slap case (Figure 6.2a), the water surface quickly develops vertically at the contact point due to the relatively high wave board acceleration ($t^* = 0.21$). The contact point continues to climb upward ($t^* = 0.44$) and becomes a thin sheet of fluid with a very steep orientation, hereby referred to as the vertical jet. All acceleration of the wave board has ended by this time and the forward inertia of the vertical jet causes it to start to detach from the wave board and a bulge is formed near its peak ($t^* = 0.68$). The fluid that formed the vertical jet is now directed through the bulge and becomes a horizontal jet. The horizontal jet extends forward of the bulge, effectively stretching and flattening out the deflected surface, which was previously oriented vertically along the wave board, ($t^* = 0.91$). This flattening of the surface causes the peak surface height to drop slightly. Thus, in the overdriven mode, the plunging jet is the redirection of the vertical jet, formed in the initial stages of the wave board motion, into a horizontal jet. Therefore, increasing the wave board acceleration (a_b) will increase both the height of the vertical jet, i.e. the contact point height, as was seen Figure 3.16 and the length of the plunging jet, as was seen in Figures 4.3 & 4.4.

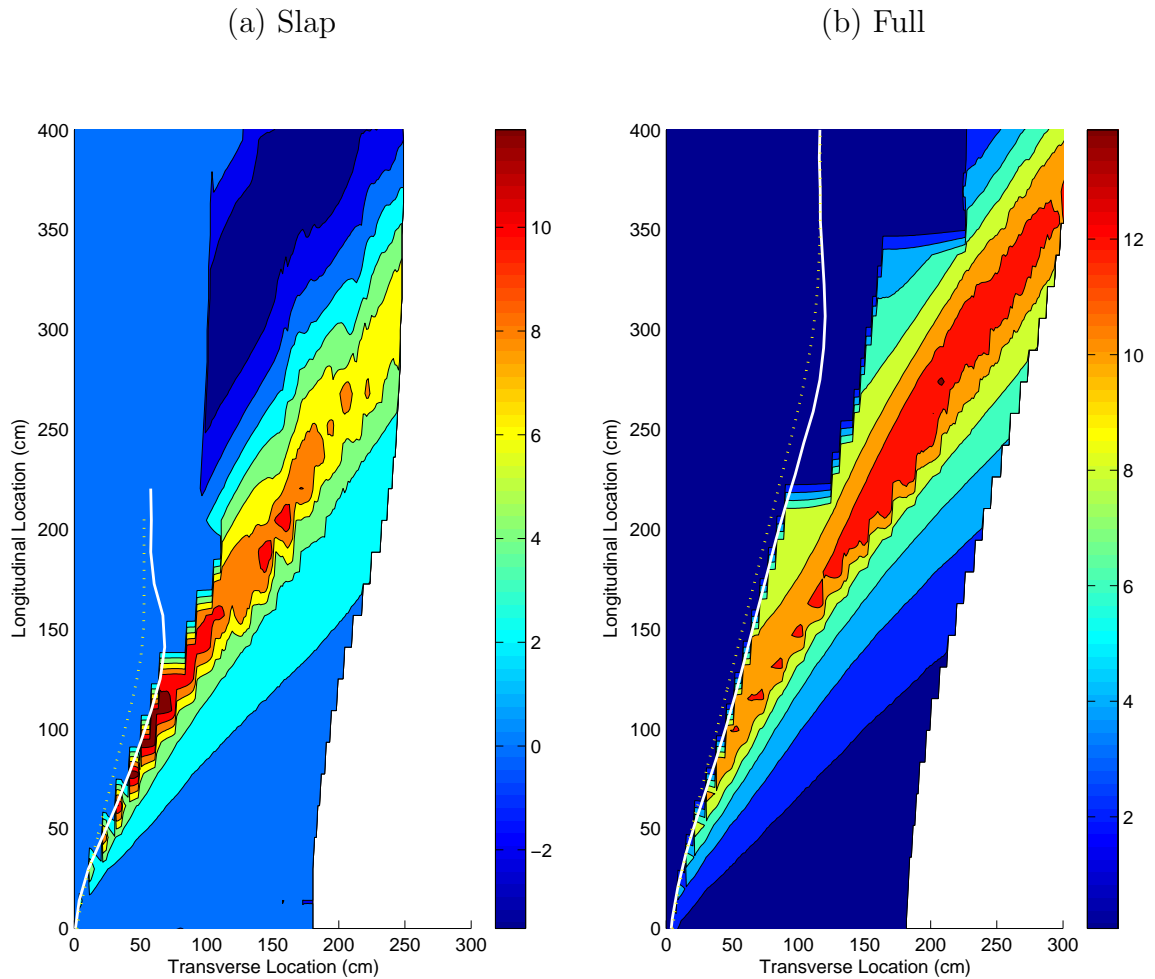


Figure 6.1: Contour plots of water surface: (a) Slap, $V_b = 0.98$ m/s, (b) Full, $V_b = 0.98$ m/s. Contour lines are in units of cm (vertical elevation). Solid white line represents the transverse location of the contact point and the yellow dashed line represents the location of the waterline translation of the wave maker. The vertical axis has been transformed into a dimensional value by using an arbitrary forward velocity of 100 in/s (recall: $x = x_0 + Ut$).

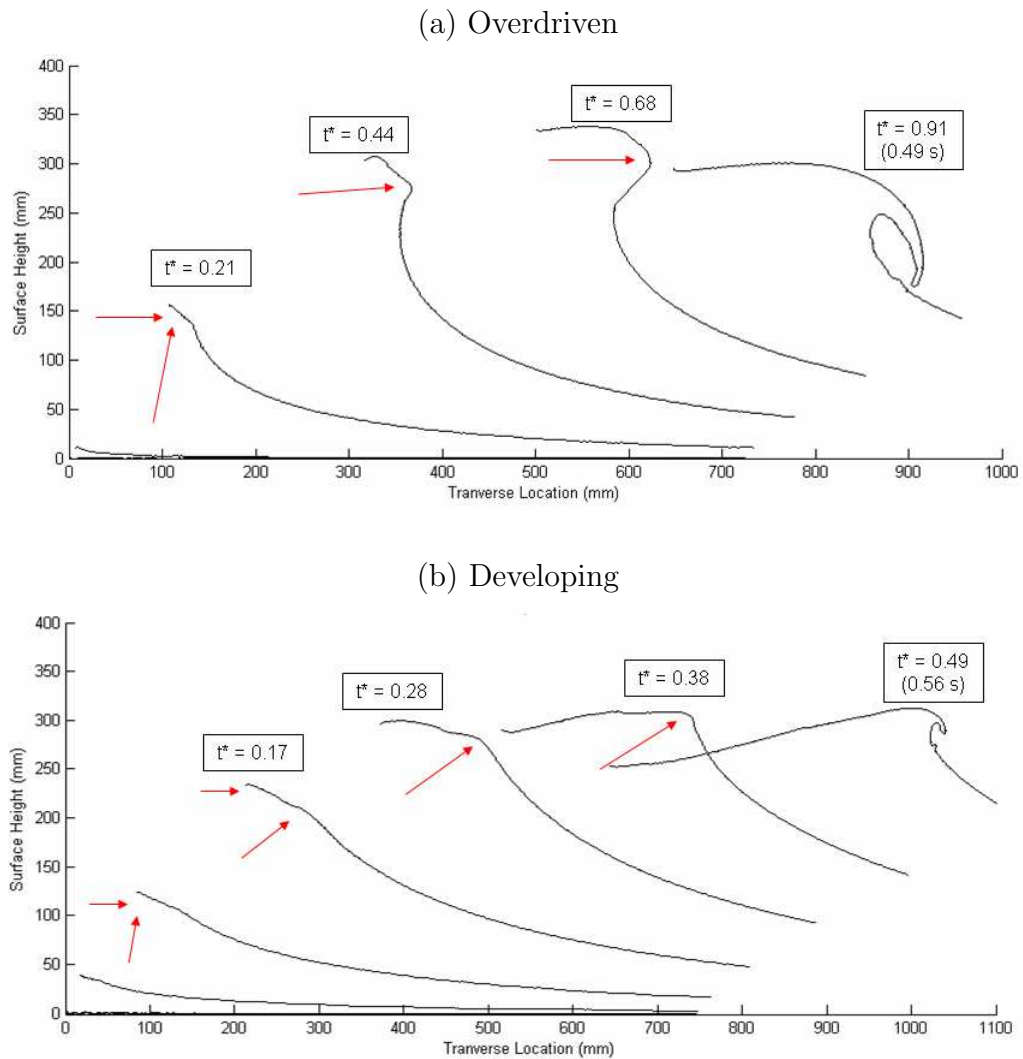


Figure 6.2: Illustration of breaking modes: (a) overdriven (Slap, $V_b = 0.94$ m/s) and (b) developing (Full, $V_b = 0.98$ m/s). $t^* = t/t_{wm}$. Red arrows indicate dominant flow directions.

In the developing mode, which is observed in the Full case, a much less pronounced vertical jet forms along the wave board. In Figure 6.2b, the surface deflection for the Full case can be seen as more of a rounded half-bump ($t^* = 0.17$) which is noticeably flatter than the early stages of the Slap case. Once the surface deflection in the Full case has increased to a sufficient height, it detaches and moves away from the wave board ($t^* = 0.28$). Because the peak contact point height has occurred relatively early in the wave maker motion profile ($t_{cp} = 0.31t_{wm}$ for this case), the wave board motion continues to raise the local surface elevation and push the wave crest upward after it has detached ($t^* = 0.38$), causing the forward face to continue to steepen. The steepening continues until a plunging jet is formed ($t^* = 0.49$).

A key difference between the Slap and Full cases is the bottom translation (B_k). The early stages of the Full case are similar to that of a translating vertical plate. This creates a much greater amount of upwelling during the acceleration phase than in the Slap case where most of the displacement is near the water line or above. This upwelling in the early stages of the wave maker motion raises the local water level around the wave board and likely dampens the vertical jet that is formed and prevents it from becoming as steep as in the Slap case.

The developing wave appears similar to freely propagating breakers where a rapid steepening of the wave results in breaking. One type of freely propagating breaker is a dispersively focused wave, in which the confluence of various wavelengths causes a rapid steepening of a wave. A series of surface profiles from a dispersively focused wave is shown in Figure 6.3. At the beginning of the profiles, the slope of

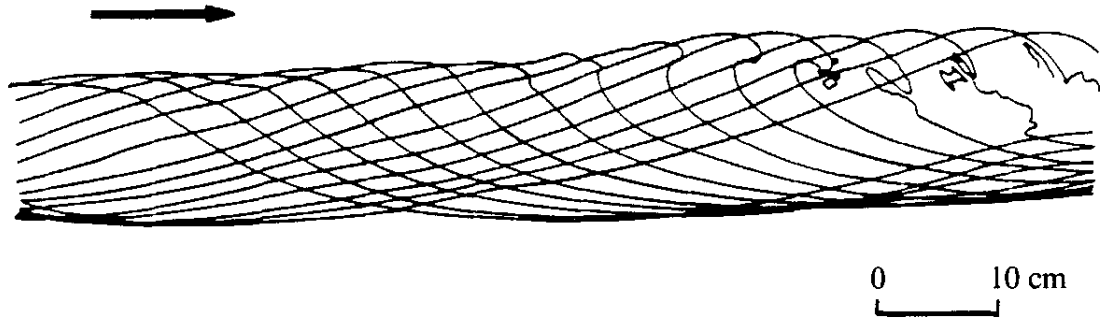


Figure 6.3: Surface profiles of a dispersively focused plunging breaker at intervals of ≈ 0.04 seconds (taken from Bonmarin 1989)

the front wave face is not particularly steep. However, as the various wavelengths converge, the wave steepens rapidly which creates a forward ejection of fluid. For the developing wave, increasing the rate of upwelling, i.e. increasing the speed of the wave maker, results in an increase of the rate of steepening. This causes the wave to break sooner, as observed in the behavior of the impact point location (Figure 3.12).

Because the developing wave breaks closer to the wave board with increasing wave maker speed, it is believed that the wave will eventually become overdriven with sufficient wave board speed and acceleration. Because of mechanical limitations, it was not possible to run the Full cases at speeds high enough to observe this. However, this would be an appropriate application for future computational studies.

The Fixed case waves are also overdriven, especially at high angles of attack. Because the angle of attack is present at the beginning of the motion, the vertical jet that is formed is immediately deflected forward which, at high enough speeds,

Fixed, 30° (overdriven)

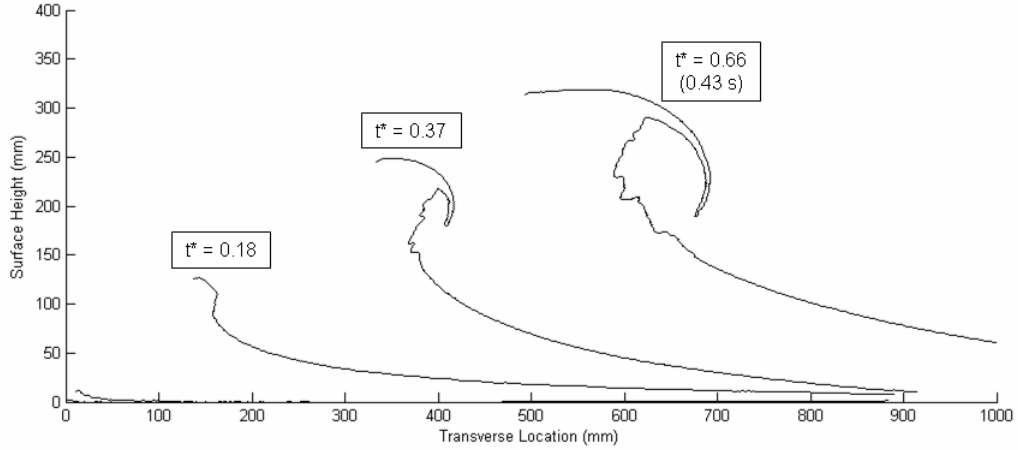


Figure 6.4: Illustration of overdriven breaking mode with Fixed, 30° ($V_b = 0.97$ m/s). $t^* = t/t_{wm}$.

develops into a plunging jet directly off the wave board. The steeper angles of attack (30°) formed stronger plungers and did so at lower board speeds (first plunger seen at $F_b = 0.26$ for 30° versus $F_b = 0.32$ for 15°).

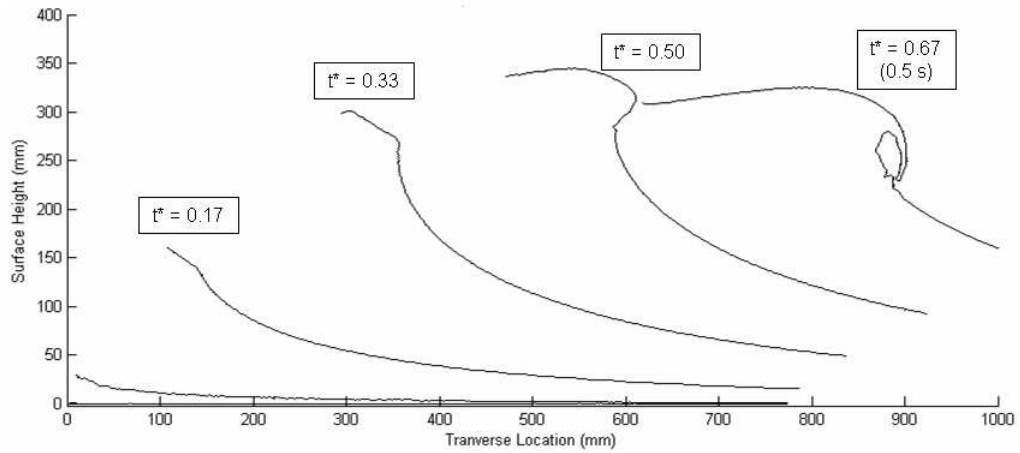
The two Mix cases also break according to the two modes, though they behave more as intermediary cases than purely overdriven or developing cases. Surface profiles for the two cases are shown in Figure 6.5. The key differences can be seen near the contact peaks. Comparing $t^* = 0.33$ (Mix 0.2) and $t^* = 0.26$ (Mix 0.4), it is apparent that the wave face is clearly steeper in the Mix 0.2 case. This leads to earlier development of a horizontal jet ($t^* = 0.50$, Mix 0.2), which is characteristic of the overdriven wave. The Mix 0.4 case behaves like a developing wave though the profile shape near impact ($t^* = 0.52$) appears somewhat similar to the Mix 0.2 case (at $t^* = 0.67$). The Mix cases, as the name implies, are in between the slap and full cases in terms of translation. Based on the profiles of Figures 6.2 & 6.5 and

the trends observed in Figure 3.12 and Table 4.1, it appears that the Mix 0.4 case is probably close to the threshold between overdriven and developing, albeit more in the developing region.

6.3 Identification of Breaking Mode

One of the most strongly identifying features of a developing wave is the detachment of the wave and subsequent drop in contact point height before the wave has broken. One way of quantifying this feature is hereby referred to as the back face drop, which is defined as $\frac{Z_p - Z_c}{Z_p}$. Overdriven waves break when the contact point height is close to the peak height of the wave and thus will have a low value for back face drop. Developing waves, conversely, should have a high value for back face drop because the contact point is able to drop far below the crest height. With a quantifiable indicator of breaking mode selected, it is desired to relate back face drop with the steepness of the vertical jet that is formed in the initial stages of the wave maker motion, as this appears to be critical in determining the breaking mode. The back face drop is plotted against the slope of the vertical jet in Figure 6.6. The slope of the vertical jet is defined as the slope of the peak contact point and a point on the surface (of the same profile) at half the height of the peak contact point. A larger slope indicates a steeper surface local to the vertical jet. In the figure, it is observed that as the vertical jet slope increases, the back drop value decreases for all cases. The developing mode cases (Full and Mix 0.4) produce waves with a back face drop > 0.1 but appear to be decreasing rapidly with increased vertical jet

(a) Mix 0.2 (slightly overdriven)



(b) Mix 0.4 (slightly developing)

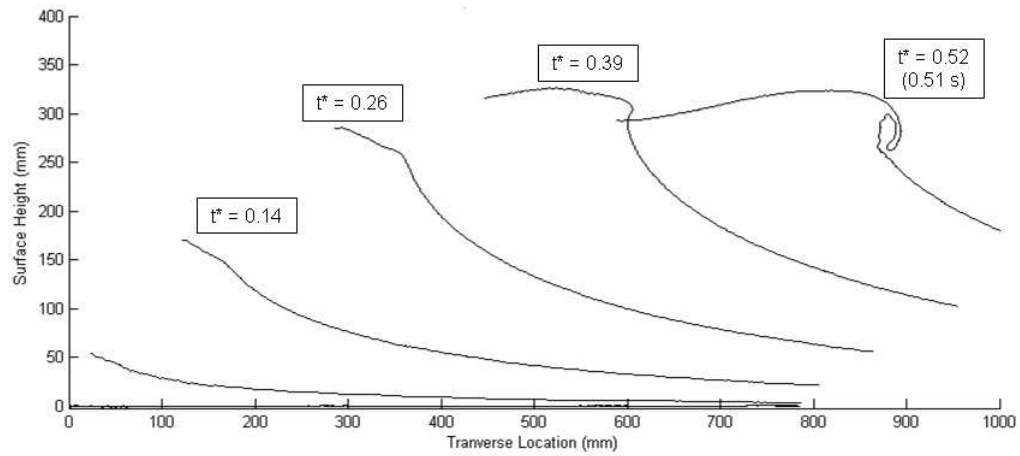


Figure 6.5: Illustration of breaking modes with mix cases: (a) Mix 0.2, overdriven ($V_b = 0.99$ m/s) and (b) Mix 0.4, developing ($V_b = 0.97$ m/s). $t^* = t/t_{wm}$.

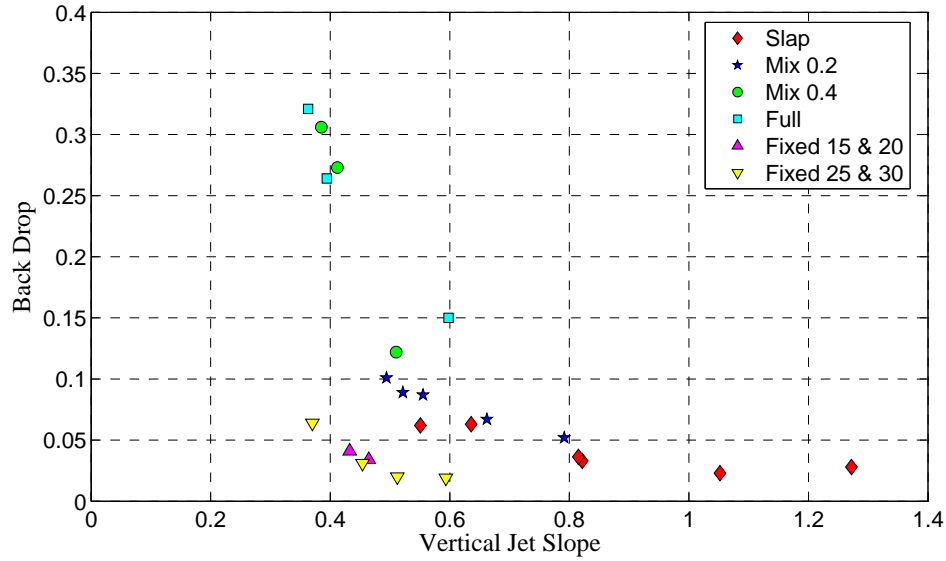


Figure 6.6: Back drop ($\frac{Z_p - Z_c}{Z_p}$) versus vertical jet slope.

slope. This is consistent with the notion that if a Full case were run at a sufficiently high speed it would produce an overdriven wave. Increasing the steepness of the vertical jet beyond a critical value would, it is hypothesized, result in a consistently low back face drop indicative of an overdriven wave.

6.4 Role of Breaking Mode in Wave Variability

The observed wave variability in some of the cases was discussed in §3.7. The variability was only observed in select speeds of the Full and Mix 0.4 cases, both of which produce developing waves. It is believed that this variability is a characteristic of developing waves which are near the transition between spilling and plunging breakers. For any wave to develop a plunging jet, the forward wave face must be able to achieve a very steep slope. Because the steepening of the

wave is significantly slower for the developing wave, any disturbances on the water surface that may induce turbulence will have a longer time to grow and a greater opportunity to inhibit the process of steepening of the forward face. The developing waves therefore appear to be more sensitive to the flow field than overdriven waves.

Chapter 7

Conclusions

7.1 Summary

A parametric set of motions using a 2D+T wave maker has produced a set of waves that are highly varied in shape. A number of characteristics have been successfully measured and related to various wave maker parameters. The key findings of this study are as follows:

- There is a linear relationship between peak water surface heights (contact point and crest) and wave board speed (V_b). Plots of wave heights versus wave board speed suggest zero wave height when the wave board moves at the minimum phase speed for a linear gravity-capillary wave in clean water.
- The wave board Froude number (or speed) is a surprisingly accurate predictor of breaker type with plungers only observed for $F_b > 0.29$ and only spillers observed for $F_b < 0.26$.
- The time to reach the peak contact point height was remarkably consistent (≈ 0.37 seconds, ± 0.06 seconds) in all tests.
- Independent variation of the wave board acceleration affects the contact peak height and plunging length but has little effect on most other aspects of the wave, including crest height (after the wave has detached).

- The vertical acceleration of the plunging jet tip was consistently less than gravity, with a typical value around 0.6g.
- The thickness of a plunging has a linear relationship with wave board acceleration, a_b , but shows little correlation with wave board speed.
- The tapered thickness profile observed in the plunging jet appears to be related to the tapering of a steady vertical liquid sheet falling under gravity.
- Two distinct breaking modes, overdriven and developing, are observed:
 - The overdriven mode is identified by a prominent vertical jet that forms at the contact point. This vertical jet is then deflected forward by the wave board and becomes a plunging breaker at high speeds.
 - The developing mode does not break adjacent to the wave board but rather "detaches" and continues to steepen as water being moved by the wave board creates an upwelling beneath the wave. The rapid steepening of the wave leads to breaking and, at sufficient speeds, a plunging jet is formed. The breaking mechanism of the developing mode appears to be similar to freely propagating waves.

7.2 Applications and Future Work

Ultimately, it is desired that this work be of use to ship designers. By being able to relate a given bow profile with the predicted size and shape of bow wave, designers can have the ability to adjust the hull to create a desired wave train. The

parameter of wave board speed translates to hull shape as a combination of entrance angle and forward speed. Angle of attack and angular rotation is a combination of flare angle (as a function of longitudinal location) and forward speed. Wave board acceleration, unfortunately, does not correspond to a ship parameter as well. Ship bows generally have a blunt leading edge that is, in effect, infinite wave board acceleration. This also creates a pressure source and upstream water rise, which is not simulated in these experiments. The wave board acceleration, seen to be very important for many of the breaking characteristics, is largely an experimental approximation. Nonetheless, it is surmised that an equivalent acceleration could be estimated for 3-D model tests by examining the flow characteristics around the bow and closely investigating the vertical sheet that forms along the contact line.

While this study did not investigate energy losses that would result in ship resistance, it would be interesting to explore relationship between the different breaking modes and ship resistance. This could be done with model tests or through numerical simulations. While not directly being related to ship resistance, it should be noted that the Full and Slap cases, when run at similar wave board speeds, produced similar wave heights despite a 350% difference in volume displaced by the wave maker. There may also be value (vibrations, motions, hull wear) in creating waves that break further away from the hull as they do in the developing mode.

As discussed in §5.8, there are disturbances that sometimes develop on the plunging sheet. These disturbances sometimes appear to be organized into a regular pattern but it is impossible to draw conclusions from the images produced by this experimental setup. If transverse views and measurements of the sheet surface were

obtained, it would be very interesting to study these disturbances as they relate to the overall stability of the plunging sheet.

As with any experiment, there were several parameters that were not varied in this study but could likely provide further insight. One promising parameter is the surface tension. Surface tension forces likely become high in the plunging jet where there are regions with high surface curvature. Surface tension has also been shown to be critical in the breaking process of short wavelength spilling breakers (Duncan 2001). It has been noted by Liu and Duncan (2006) that at surfactant concentrations above the critical micelle concentration, the surface behaves like that of a pure liquid with a lower surface tension than water. Thus, these conditions may be helpful in exploring surface tension effects in the wave tank.

Appendix A

Matlab Codes

A.1 Edge Detection

```
% Step 1. Be sure that the following .m files are in the same folder as
% your .bmp files:
% wave_edge_11.m
% wave_spline_fitting.m
% wave_nighbor_search.m
% For example, all of my .bmp files are in C:\AMostafa\2D+T\Mo5415\2006_01(Jan)
% \w_060119_20p0knot_02p800sec\w_060119_20p0knot_02p800sec_zone1_01a;
% therefore I should have those .m files in that folder as well.
% Step 2. Make sure that the current directory in Matlab is the same path as where
% the .m and the .bmp files are located; this way the .txt files will be written in
% the same folder as the .bmp files.
% Step 3. Change the prefix to match the name of your .bmp files, leaving
% off the numbers and extension type. For example, my .bmp are named
% w_060119_20poknot_02p800sec_zone1_01a_0300.bmp; therefore I use prefix =
% 'w_060119_20poknot_02p800sec_zone1_01a_';
%-----
close all; clear all; clc;
% filename
prefix = 'mw_slap_w_070831_30d_0p542s_z1_1_';
```

```

dt = 16;          %increment of images

extr = '.bmp'; extw = '.txt';

x_axis = [0 1000];
y_axis = [500 1000];

FirstImage = input('Please enter the number of the wave image (FirstIm =?): ');
go_on = 'Y'; i= 0;

thresh = 0.05;
ni = 1200; nj = 1632;
while(go_on == 'Y' | go_on == 'y')
    ii = FirstImage + i;
    disp(['The present image number: ',num2str(ii)])
    redo = 'Y';
    while redo == 'Y' | redo == 'y'
        filename = strcat(prefix, num2str(ii,'%04g'),extr);
        a = imread(filename, 'bmp');
        ap = a;
        bw = edge(a,'canny',thresh);
        for jp = 1:nj
            for ip = 1:ni
                if (bw(ip,jp) == 1)
                    ap(ip,jp) = 255;
                end
            end
        end
    end
end
end
end

```

```

imshow(ap)

xlim([x_axis(1) x_axis(2)])

ylim([y_axis(1) y_axis(2)])

[xi yi] = ginput(1);

x1 = fix(xi);

y1 = fix(yi);

while ~bw(y1,x1)

    y1 = y1+1;

end

hold on

plot(x1,y1, '.r');

hold off;

profile_x(1) = x1;

profile_y(1) = y1;

j = 2;

nim5 = ni - 5;

njm5 = nj - 5;

%     [xni yni] = ginput(1);

%     xn = fix(xni);

%     yn = fix(yni);

%     while ~bw(yn,xn)

%         yn = yn+1;

%     end

%     hold on

%     plot(xn,yn, '.r');

%     hold off;

```

```

while(j<10000 & x1<njm5 & y1<nim5)

    nighbr_x = [x1 x1+1 x1+1 x1+1 x1 x1-1 x1-1 x1-1];
    nighbr_y = [y1-1 y1-1 y1 y1+1 y1+1 y1+1 y1 y1-1];

    for k=1:8,

        if bw(nighbr_y(k), nighbr_x(k))

            x1 = nighbr_x(k);

            y1 = nighbr_y(k);

            profile_x(j) = x1;

            profile_y(j) = y1;

            break;

        end

    end

    if(j>3 & x1 == profile_x(j-2) & y1 == profile_y(j-2))

        dx = profile_x(j-1)-profile_x(j-2);

        dy = profile_y(j-2)-profile_y(j-1);

        [x1, y1] = wave_neighbor_search(profile_x(j-1), profile_y(j-1), dx, dy, bw);

        profile_x(j) = x1;

        profile_y(j) = y1;

    end

    for k1=1:j-1

        if x1 == profile_x(k1) & y1 == profile_y(k1)

            hold on

            plot(x1,y1,'r+');

            plot(profile_x, profile_y,'r');

            [xys, k1]= wave_spline_fitting(profile_x, profile_y);

            % add the repeated point profile1 check here

            %k1= overlap_point(k1, profile_x, profile_y, xys);

```

```

        for jj=1:length(xys)

            profile_x(k1+jj-1) = round(xys(1,jj));

            profile_y(k1+jj-1) = round(xys(2,jj));

        end

        j=k1 + length(xys) - 1;

        clear xys;

        break;

    end

end

x1 = profile_x(j);

y1 = profile_y(j);

j = j + 1;

end

imshow(a); hold on;

plot(profile_x, profile_y,'r'); hold off;

redo = input('Mend the curve? Y/N [N]: ', 's');

if isempty(redo)

    redo = 'N';

end

if redo == 'Y' | redo == 'y'

    clear profile_x profile_y

end

end

filename_out = strcat(prefix,num2str(ii,'%04g'),extw); fid = fopen(filename_out,'w');

fprintf(fid,'%8.4f \t %8.4f\n',[profile_x;(ni+1)-profile_y]); fclose(fid);

clear profile_x profile_y;

go_on = input('Continue to process NEXT image? Y/N [Y]: ', 's');

```



```
if isempty(go_on)

    go_on = 'Y';

end

% *****

    i = i + dt;

% *****

end
```

A.2 Inverse Transformation

```
close all; clear all; clc;

t1 = 95; dt = 16; tn = 303;

tz = 95;

% -----

dirname = 'E:\UMD\Research\2D+T\ModelWedge\Processing\';

gridname = 'Slap\grid\calib_data_090326_zone1_1_grid';

ext = '.txt';

output_name = [dirname,gridname,ext];

fidc = fopen(output_name);

xc = fscanf(fidc,'%g %g',[2 inf]);

fclose(fidc);

nh = xc(1,1);

nv = xc(2,1);

num_pts = (nv+1)*(nh+1)+1;

cbd = (xc(:,2:num_pts))';

cbdx = cbd(:,1);  cbdy = cbd(:,2);

for i=1:(nv+1)

    for j=1:(nh+1)

        countxy = j+((i-1)*(nh+1));

        ii=nv+2-i;

        jj=nh+2-j;

        sx(jj,ii) = cbdx(countxy);
```

```

        sy(jj,ii) = cbdy(countxy);

    end

end

% -----

npoly = 1;

Xi = 0:1:nv-1;

Yi = nh-1:-1:0;

for i = 1:nh

    xh = sx(i,:);

    yh = 1201-sy(i,:);

    fx(i,:) = polyfit(xh,yh,npoly);

    yhint = polyval(fx(i,:),xh);

end

for j = 1:nv

    xv = sx(:,j);

    yv = 1201-sy(:,j);

    fy(j,:) = polyfit(yv,xv,npoly);

    xvint = polyval(fy(j,:),yv);

end

% -----

ext = '.txt';

foldername = 'pix2\0p608s_w_z1_1\';

prefixname = 'mw_slap_w_090326_30d_0p608s_z1_1_';

prefix_w = 'in_';

carfolder = 'Slap\carriage\';

```

```

car_ext = 'car.txt';

filec = [dirname,carfolder,prefixname,car_ext];

fidc = fopen(filec);

xc = fscanf(fidc,'%g',inf); fclose(fidc);

xcar = smooth(xc,0.05,'rloess');

istart = 64; zone1 = 0; % = 0 (zone1), 21.12 (zone2), 42.54 (zone3)

for num = tz,

    number = num2str(num,'%04g');

    filea = [foldername,prefixname,number,ext]; fida = fopen(filea);

    [input,count] = fscanf(fida,'%g',[2 inf]); fclose(fida);

    xi = input(1,:);

    yi = input(2,:);

    nxi = length(xi);

    nyi = nxi;

    for ik = 1:nv

        xiint(:,ik) = polyval(fy(ik,:),yi);

    end

    for jk = 1:nh

        yiint(:,jk) = polyval(fx(jk,:),xi);

    end

    Xiint = zeros(1,nxi);

    for mk = 1:nyi

        fXx = polyfit(xiint(mk,:),Xi,npoly+1);

```

```

        Xiint(1,mk) = polyval(fXx,xi(mk));

    end

    Yiint = zeros(1,nyi);

    for nk = 1:nxi

        fYy = polyfit(yiint(nk,:),Yi,npoly+1);

        Yiint(1,nk) = polyval(fYy,yi(nk));

    end

    xx = xcar(num-istart) + Xiint;

    yy = Yiint;

    xx0 = xx(1)

    yy0 = mean(yy)

    clear xiint yiint Xiint Yiint xi yi xx yy input;

end

for num = t1:dt:tn,

    number = num2str(num,'%04g');

    disp(number)

    filea = [foldername,prefixname,number,ext]; fida = fopen(filea);

    [input,count] = fscanf(fida,'%g',[2 inf]); fclose(fida);

    xi = input(1,:);

    yi = input(2,:);

    nxi = length(xi);

    nyi = nxi;

    for ik = 1:nv

```

```

        xiint(:,ik) = polyval(fy(ik,:),yi);
    end

    for jk = 1:nh
        yiint(:,jk) = polyval(fx(jk,:),xi);
    end

    Xiint = zeros(1,nxi);

    for mk = 1:nyi
        fXx = polyfit(xiint(mk,:),Xi,npoly+1);
        Xiint(1,mk) = polyval(fXx,xi(mk));
    end

    Yiint = zeros(1,nyi);

    for nk = 1:nxi
        fYy = polyfit(yiint(nk,:),Yi,npoly+1);
        Yiint(1,nk) = polyval(fYy,yi(nk));
    end

    end

    xx = xcar(num-istart) + Xiint + zone1;
    yy = Yiint;

    plot((xx-xx0),(yy0-yy),'-k'); hold on;

    filew = [foldername,prefixname,prefix_w,number,ext];
    fidw = fopen(filew,'w');
    fprintf(fidw,'%8.4f \t %8.4f \n',[(xx-xx0);(yy0-yy)]); fclose(fidw);

    clear xiint yiint Xiint Yiint xi yi xx yy input;
end

```

A.3 Jet Thickness Calculation

```
%This code determines jet thickness using Snell's Law of Refraction

%(x,y,z) = (longitudinal,vertical,transverse)

clear all; clc; %close all;

%file info

prefix_r = 'mw_slap_070831_30d_0p542s_z1_1_in_';

frame='0262';

ext_in = '_in.txt';

ext_out = '_out.txt';

curve_order=5;      %polynomial order for edge fits

curve_order_in=3;   %polynomial order for real inside edge fit

xl=870;  xr=950;    %plot extents

camera_location=[52.358 -38.949 40.134]; %[X Y Z]

car_loc = 9.9493;    %x-value for carriage location

origin_pt = [-6.08 13.91];

out_trim_beginning=100; %trim beginning of outside profile

out_trim_end=115;      %trim end of outside profile

in_trim_beginning=1;   %trim beginning of inside profile

in_trim_end=125;      %trim end of inside profile

%%%%%%%%%%%%%%%%%%%%%%%%%%%%%%%%%%%%%%%%%%%%%%%%%%%%%%%%%%%%%%%%%%%%%%%%

%%%%%%%%%%%%%%%%%%%%%%%%%%%%%%%%%%%%%%%%%%%%%%%%%%%%%%%%%%%%%%%%%%%%%%%%

% read files

file_in = [prefix_r,frame,ext_in]; fida = fopen(file_in);
```

```

[input_in,count] = fscanf(fid_a,'%g',[2 inf]); fclose(fid_a);

file_out = [prefix_r,frame,ext_out]; fid_b = fopen(file_out);

[input_out,count] = fscanf(fid_b,'%g',[2 inf]); fclose(fid_b);

input_in=input_in*25.4;

input_out=input_out*25.4;

camera_location=camera_location*25.4;

car_loc=car_loc*25.4;

origin_pt=origin_pt*25.4;

%organize data

Lin=length(input_in);

Lout=length(input_out);

xin = input_in(1,1+in_trim_beginning:Lin-in_trim_end);

yin = input_in(2,1+in_trim_beginning:Lin-in_trim_end);

xout = input_out(1,1+out_trim_beginning:Lout-out_trim_end);

yout = input_out(2,1+out_trim_beginning:Lout-out_trim_end);

%reduce # of points to analyze (smoother slopes)

numpts_out=length(xout); numpts_in=length(xin);

step=2;          % adjusts number of points used

buffer=10;      % curve fit used to find local slope

count_out=(1:step:numpts_out-buffer);

xoutc=xout(count_out); youtc=yout(count_out);

count_in=(1:step:numpts_in);

xinc=xin(count_in); yinc=yin(count_in);

```



```

numptsc=length(xoutc);

%global curve fitting, outside
pc_out=polyfit(xoutc,youtc,curve_order);
yc_out=polyval(pc_out,xoutc);
pdc_out=polyder(pc_out);
slope_out=polyval(pdc_out,xoutc);
normal_out=-1./(slope_out);
normal_b=youtc-(normal_out.*xoutc);

px_in(1)=xinc(1); px_in(2)=xinc(length(xinc));
py_in(1)=yinc(1); py_in(2)=yinc(length(yinc));

%global curve fitting, inside only using all points and new endpoints
xinc_red=xinc(xinc>px_in(1)); % using only data within endpoints
xinc_red=xinc_red(xinc_red<px_in(2)); % using only data within endpoints
pc_in=polyfit(xinc,yinc,curve_order_in);
yc_in=polyval(pc_in,xinc);
yc_in_red=polyval(pc_in,xinc_red);

% camera parameters
camera_x=camera_location(1)+car_loc-origin_pt(1);
camera_y=-camera_location(2)+origin_pt(2);
camera_z=camera_location(3);

% wave/camera vector intersection routine
for i=1:length(xinc_red)

```

```

x_slope = (xinc_red(i)-camera_x)/camera_z; % camera vector
y_slope = (yc_in_red(i)-camera_y)/camera_z; % camera vector
y_diff=0.1; y_diff2=0;

z=0;          % z coordinate, used for line equations

while y_diff>0.000001

    z=z+(y_diff2/4);

    camera_end(1)=xinc_red(i)-(x_slope*z);

    camera_end(2)=yc_in_red(i)-(y_slope*z);

    wave_y=polyval(pc_out,camera_end(1));

    y_diff=abs(wave_y-camera_end(2));

    y_diff2=wave_y-camera_end(2);

end

wave_camera_int(i,1)=camera_end(1);

wave_camera_int(i,2)=wave_y;

wave_camera_int(i,3)=z;

length_horiz(i)=sqrt(((camera_end(1)-xinc_red(i))^2)+(z^2));

end

wave_slope=polyval(pdc_out,wave_camera_int(:,1));

wave_normal=-1./(wave_slope);

delx=camera_x-wave_camera_int(:,1);

dely=camera_y-wave_camera_int(:,2);

delz=camera_z-wave_camera_int(:,3);

length_total=sqrt((delx.^2)+(dely.^2)+(delz.^2)); %total distance

%camera vector

```

```

vector_in(:,1)=delx;

vector_in(:,2)=dely;

vector_in(:,3)=delz;

xz_slope=delx./delz; %delta z over delta y for incoming ray
yz_slope=dely./delz; %delta z over delta x for incoming ray

%wave normal vector
normalphi=atan(wave_normal);

vector_cyl(:,1)=cos(normalphi); % negative for left breaking wave
vector_cyl(:,2)=sin(normalphi); % negative for left breaking wave
vector_cyl(:,3)=xinc_red*0;

for k=1:(length(xinc_red))

    dp=dot(vector_in(k,:),vector_cyl(k,:));

    total_angle(k)=acos(dp/length_total(k));

end

%snell's law application

n1=1; %air

n2=1.33; %index of refraction for water (1.33) and glass (1.49)

theta3=(pi/2)-(total_angle');

theta1=(pi/2)-theta3;

theta2=asin((n1/n2)*sin(theta1));

t2=(length_horiz')./tan(theta2);

t1=(length_horiz').*tan(theta3); % unaffected ray

```

```

x_in_real=wave_camera_int(:,1)-(xz_slope.*wave_camera_int(:,3)+((t2-t1).*vector_cyl(:,1)));
y_in_real=wave_camera_int(:,2)-(yz_slope.*wave_camera_int(:,3)+((t2-t1).*vector_cyl(:,2)));
x_in_orig=wave_camera_int(:,1)-(xz_slope.*wave_camera_int(:,3)); % unaffected ray
y_in_orig=wave_camera_int(:,2)-(yz_slope.*wave_camera_int(:,3)); % unaffected ray

% calculate thickness from inside points
for i=1:length(x_in_real)
    for k=1:length(xout)
        dist(k)=sqrt(((x_in_real(i)-xout(k))^2)+((y_in_real(i)-yout(k))^2));
    end
    mindist=min(dist);
    mindist_num=find(dist==mindist);
    thick(i)=dist(mindist_num(1));
    thickx(i)=x_in_real(i);
    thicky(i)=y_in_real(i);
    mt=num2str(mean(thick));
    maxt=num2str(max(thick));
    mint=num2str(min(thick));
end

%%%%%% Plotting %%%%%%%%%%%%%%%

% calculate normal angles
angle=atan(normal_out);
px_in_nor=0.1*cos(angle)+xoutc;
py_in_nor=0.1*sin(angle)+youtc;

```

```

%plots

scrsz = get(0,'screensize');

figure('Position',[scrsz(3)/3 scrsz(4)/2 scrsz(3)/2.5 scrsz(4)/1.2])

subplot(2,1,1)

% figure

hold on

plot(input_out(1,:),input_out(2:,:), 'b') % raw outside profile

plot(xin,yin,'k') % raw inside edge

plot(x_in_real,y_in_real,'r') %refracted inside points

% plot(input_in(1,:),input_in(2:,:), 'b--') % raw inside profile

% plot(xin,yin,'g') % raw inside edge

% plot(xout,yout,'g') % raw outside edge

% plot(xoutc,yc_out,'k.') % curve fit outside

% plot(xinc,yc_in,'ro') % curve fit inside

%scatter(px_in,py_in,'gd') % fit normal inside points

%plot thickness lines

% for i=1:length(x_in_real)

% xline(1)=thickx(i); xline(2)=x_in_real(i);

% yline(1)=thicky(i); yline(2)=y_in_real(i);

% line(xline, yline)

% end

xlabel('x-coordinate (mm)')

ylabel('y-coordinate (mm)')

title1=['Wave Profile, Frame ',frame];

title(title1)

```

```

xlim([850 1000])

ylim([150 300])

legend('outside edge','apparent inside edge','actual inside edge',3)

grid on

hold off

subplot(2,1,2)

hold on

plot(thickx,thick,'k')

%plot(xinc_red,thick,'b')

xlim([xl xr])

ylim([0 50])

xlabel('Inside Edge x-coordinate (mm)')

ylabel('Measured Thickness (mm)')

title('Wave Jet Thickness')

grid on

hold off

%figure

%hold on

%plot(input_out(1,:),input_out(2,:),'b')

%plot(xout,yout,'r')           % raw outside edge

%plot(x_in_real,y_in_real,'g') %refracted inside points

%grid on

%hold off

strt=['Average Thickness = ',mt,' mm'];

```

```

disp(strt)

strt=['Maximum Thickness = ',maxt,' mm'];

disp(strt)

strt=['Minimum Thickness = ',mint,' mm'];

disp(strt)

%plot w/ ellipse

figure

hold on

plot(input_out(1,:),input_out(2:),'b') % raw outside profile

plot(xin,yin,'k') % raw inside edge

plot(x_in_real,y_in_real,'r') %refracted inside points

xlim([850 1000])

ylim([120 270])

scale=22;

origin=[899 198 0];

xc=origin(1); yc=origin(2); zc=origin(3);

xr=scale; yr=scale*sqrt(3); zr=0;

[x,y,z]=ellipsoid(xc,yc,zc,xr,yr,zr);

h=surf(x,y,z);

zdir=[0 0 1];

rotate(h,zdir,30,origin)

hold off

```

Appendix B

Spreadsheets

B.1 Wave Maker Parameters

The following page lists the test matrix used for this study. All pertinent wave maker parameters are included for each case. Note: Mix1 refers to Mix 0.2 cases and Mix2 refers to Mix 0.4 cases.

Case	Category	Angle	Run Time (s)	Ch. #1 Speed (ft/s)	Ch. #2 Speed (ft/s)	Ch. #2 Speed (m/s)	Ch. #2 Transition (ft)	Keel Transition (ft)	Keel Velocity (ft/s)	Keel Velocity (ft/s)	Angular Velocity (rad/s)	Volume (ft ³)	Volume Rate (ft ³ /s)	Ch. #2 Accel (m/s ²)	Profile Start time (s)	Motion Start time (s)
1	Sld	30	0.933	2.40	1.80	0.55	1.732	0	0	0	0.544	2.473	2.568	1.139	187	126
2	Sld	30	0.940	2.46	1.84	0.562	1.732	0	0	0	0.544	2.473	2.631	1.195	184	124
3	Sld	30	0.806	2.86	2.15	0.655	1.732	0	0	0	0.649	2.473	3.068	1.625	167	108
4	Sld	30	0.693	3.33	2.50	0.761	1.732	0	0	0	0.755	2.473	3.567	2.196	153	116
5	Sld	30	0.638	3.80	2.85	0.868	1.732	0	0	0	0.861	2.473	4.068	2.856	142	103
6	Sld	30	0.592	4.26	3.20	0.975	1.732	0	0	0	0.967	2.473	4.566	3.599	133	99
7	Full	30	1.350	3.26	2.83	0.864	3.625	2.050	1.548	1.548	0.988	8.591	6.394	1.279	237	150
8	Full	30	1.270	3.46	3.01	0.918	3.625	2.050	1.646	1.646	0.412	8.591	6.765	1.446	227	145
9	Full	30	1.190	3.70	3.21	0.980	3.625	2.050	1.756	1.756	0.440	8.591	7.219	1.647	216	140
10	Full	30	1.110	3.96	3.45	1.050	3.625	2.050	1.883	1.883	0.472	8.591	7.740	1.892	206	135
11	Fixed	15	1.17	1.71	1.71	0.521	2.0	2.0	1.709	1.709	0	5.854	5.004	0.176	0.891	214
12	Fixed	15	1.04	1.92	1.92	0.586	2.0	2.0	1.923	1.923	0	5.854	5.629	0.198	0.770	131
13	Fixed	15	0.91	2.20	2.20	0.670	2.0	2.0	2.188	2.188	0	5.854	6.433	1.472	180	122
14	Fixed	15	0.78	2.56	2.56	0.782	2.0	2.0	2.584	2.584	0	5.854	7.505	2.004	164	114
15	Fixed	15	0.65	3.08	3.08	0.938	2.0	2.0	3.077	3.077	0	5.854	9.006	2.886	147	106
16	Fixed	20	1.17	1.71	1.71	0.521	2.0	2.0	1.709	1.709	0	5.854	5.004	0.176	0.891	214
18	Fixed	20	1.04	1.92	1.92	0.586	2.0	2.0	1.923	1.923	0	5.854	5.629	0.198	0.770	131
19	Fixed	20	0.91	2.20	2.20	0.670	2.0	2.0	2.188	2.188	0	5.854	6.433	1.472	180	122
20	Fixed	20	0.78	2.56	2.56	0.782	2.0	2.0	2.584	2.584	0	5.854	7.505	2.004	164	114
21	Fixed	20	0.65	3.08	3.08	0.938	2.0	2.0	3.077	3.077	0	5.854	9.006	2.886	147	106
22	Fixed	25	1.17	1.71	1.71	0.521	2.0	2.0	1.709	1.709	0	5.854	5.004	0.176	0.891	214
23	Fixed	25	1.04	1.92	1.92	0.586	2.0	2.0	1.923	1.923	0	5.854	5.629	0.198	0.770	131
24	Fixed	25	0.91	2.20	2.20	0.670	2.0	2.0	2.188	2.188	0	5.854	6.433	1.472	180	122
25	Fixed	25	0.78	2.56	2.56	0.782	2.0	2.0	2.584	2.584	0	5.854	7.505	2.004	164	114
26	Fixed	25	0.65	3.08	3.08	0.938	2.0	2.0	3.077	3.077	0	5.854	9.006	2.886	147	106
27	Fixed	30	1.17	1.71	1.71	0.521	2.0	2.0	1.709	1.709	0	5.854	5.004	0.176	0.891	214
28	Fixed	30	1.04	1.92	1.92	0.586	2.0	2.0	1.923	1.923	0	5.854	5.629	0.198	0.770	131
29	Fixed	30	0.91	2.20	2.20	0.670	2.0	2.0	2.188	2.188	0	5.854	6.433	1.472	180	122
30	Fixed	30	0.78	2.56	2.56	0.782	2.0	2.0	2.584	2.584	0	5.854	7.505	2.004	164	114
31	Fixed	30	0.65	3.08	3.08	0.938	2.0	2.0	3.077	3.077	0	5.854	9.006	2.886	147	106
32	Sld	30	0.660	3.50	2.62	0.800	1.732	0.0	0.000	0.000	0.793	2.473	3.747	2.424	148	106
33	Sld	30	0.608	3.80	2.85	0.868	1.732	0.0	0.000	0.000	0.861	2.473	4.068	2.856	142	103
34	Sld 0.2	30	0.608	3.80	2.85	0.868	1.732	0.0	0.000	0.000	0.861	2.473	4.068	3.570	126	95
35	Sld 0.3	30	0.608	3.80	2.85	0.868	1.732	0.0	0.000	0.000	0.861	2.473	4.068	2.380	157	111
36	Sld	30	0.588	4.07	3.05	0.829	1.732	0.0	0.000	0.000	0.822	2.473	4.384	0.314	137	100
37	Mix1	30	1.100	2.73	2.21	0.673	2.428	0.696	0.633	0.476	0.277	4.511	4.101	1.223	205	134
38	Mix1	30	0.892	3.41	2.75	0.839	2.428	0.696	0.789	0.594	0.284	4.511	5.114	1.903	177	120
39	Mix1	30	0.860	3.50	2.82	0.861	2.428	0.696	0.809	0.609	0.291	4.511	5.245	2.001	174	119
40	Mix1 0.2	30	0.860	3.50	2.82	0.861	2.428	0.696	0.809	0.609	0.291	4.511	5.245	2.502	152	108
41	Mix1 0.3	30	0.860	3.50	2.82	0.861	2.428	0.696	0.809	0.609	0.291	4.511	5.245	1.668	196	130
42	Mix1	30	0.840	3.58	2.89	0.881	2.428	0.696	0.829	0.623	0.298	4.511	5.370	2.088	172	118
43	Mix1	30	0.790	3.81	3.07	0.937	2.428	0.696	0.881	0.663	0.317	4.511	5.710	2.372	165	115
44	Mix1 0.2	30	0.790	3.81	3.07	0.937	2.428	0.696	0.881	0.663	0.317	4.511	5.710	2.964	145	104
45	Mix1 0.3	30	0.790	3.81	3.07	0.937	2.428	0.696	0.881	0.663	0.317	4.511	5.710	1.976	185	125
46	Mix1	30	0.750	4.01	3.24	0.987	2.428	0.696	0.928	0.688	0.333	4.511	6.014	2.631	160	112
47	Mix2	30	1.245	2.97	2.51	0.765	3.125	1.393	1.119	0.421	0.421	6.551	5.262	1.229	223	144
48	Mix2	30	1.160	3.19	2.69	0.821	3.125	1.393	1.201	0.451	0.451	6.551	5.647	1.416	212	138
49	Mix2	30	1.114	3.32	2.81	0.855	3.125	1.393	1.250	0.470	0.470	6.551	5.880	1.535	207	135
50	Mix2 0.2	30	0.980	3.78	3.19	0.972	3.125	1.393	1.420	0.534	0.534	6.551	6.684	1.984	189	127
51	Mix2 0.3	30	0.980	3.78	3.19	0.972	3.125	1.393	1.421	0.534	0.534	6.551	6.684	2.479	164	114
52	Mix2 0.3	30	1.360	3.78	3.19	0.972	3.125	1.393	1.421	0.534	0.534	6.551	6.684	1.653	215	139
53	Full	30	1.360	3.26	2.83	0.863	3.622	2.050	1.548	1.548	0.988	8.591	6.394	1.278	237	150
54	Full	30	1.270	3.46	3.01	0.917	3.622	2.050	1.646	1.646	0.412	8.591	6.765	1.445	227	145
55	Full	30	1.190	3.70	3.21	0.979	3.622	2.050	1.756	1.756	0.440	8.591	7.219	1.645	216	140
56	Full	30	1.110	3.96	3.44	1.050	3.622	2.050	1.883	1.883	0.472	8.591	7.740	1.891	206	135
57	Full	30	1.309	3.36	2.92	0.890	3.622	2.050	1.597	1.597	0.400	8.591	6.563	1.360	232	148

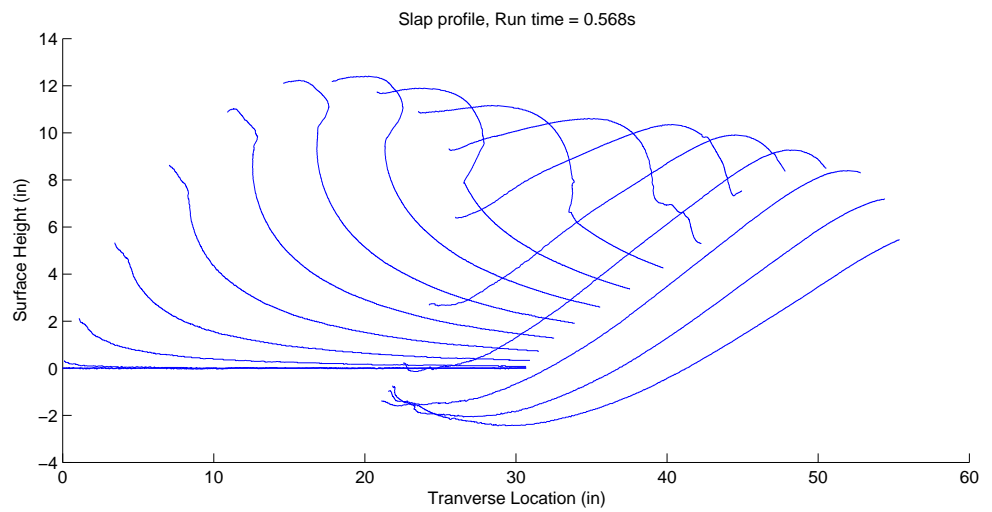
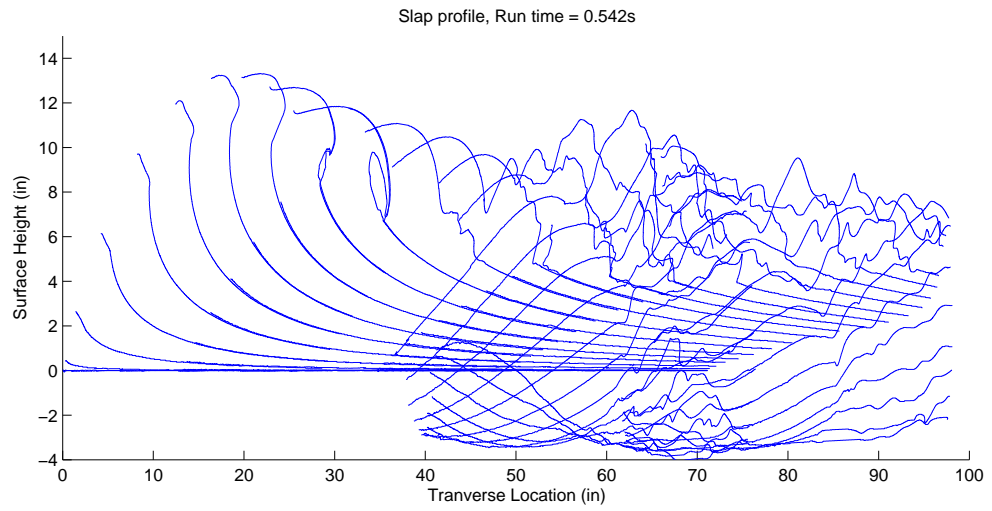
B.2 Data for Plots

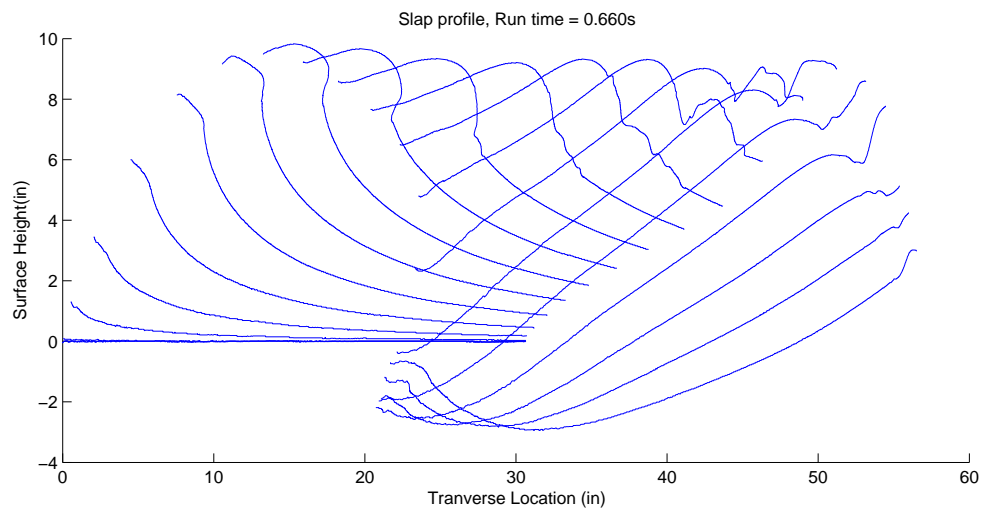
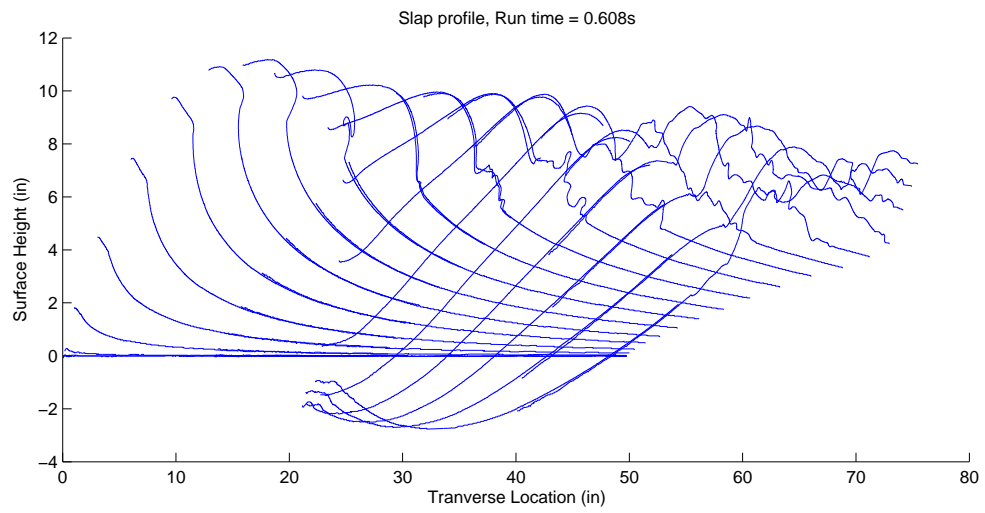
The following pages include both raw and processed experimental data used for most of the plots in this study. Note: Mix1 refers to Mix 0.2 cases and Mix2 refers to Mix 0.4 cases.

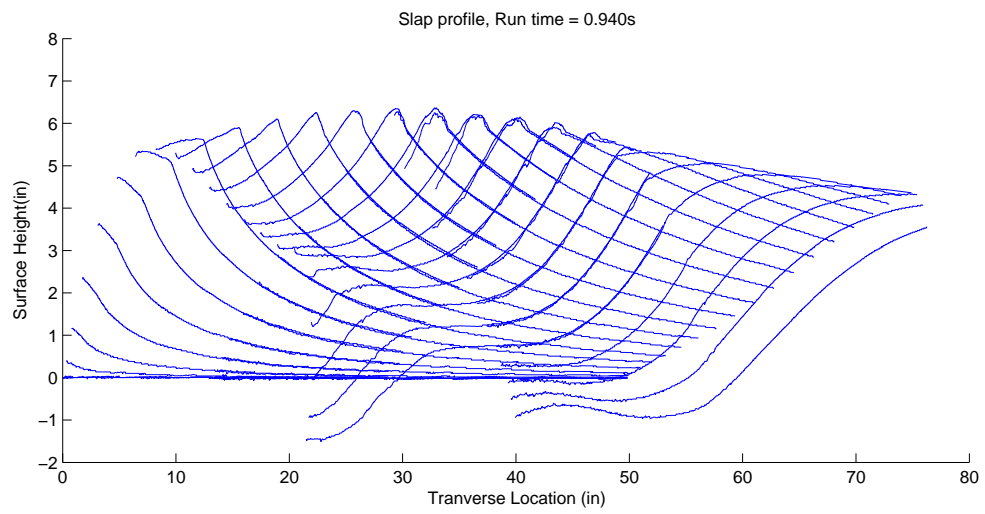
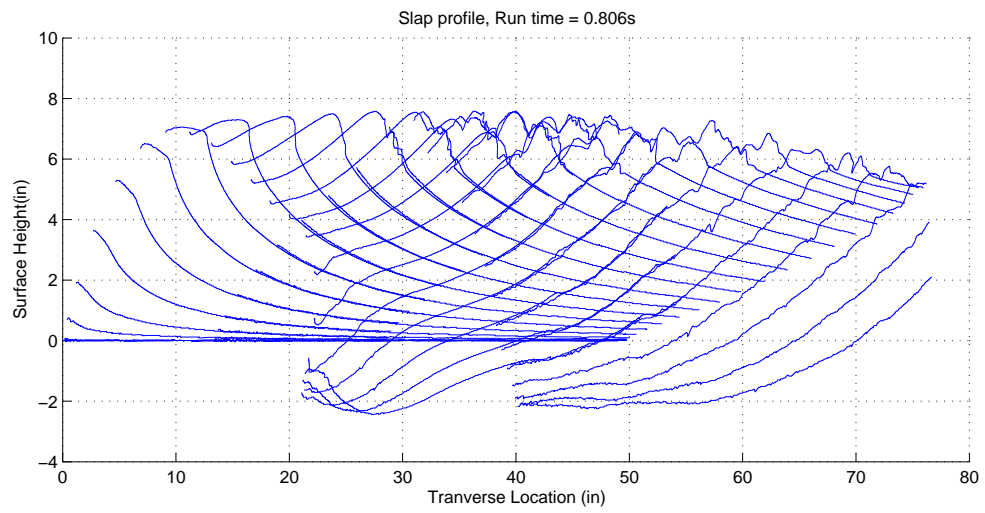
Appendix C

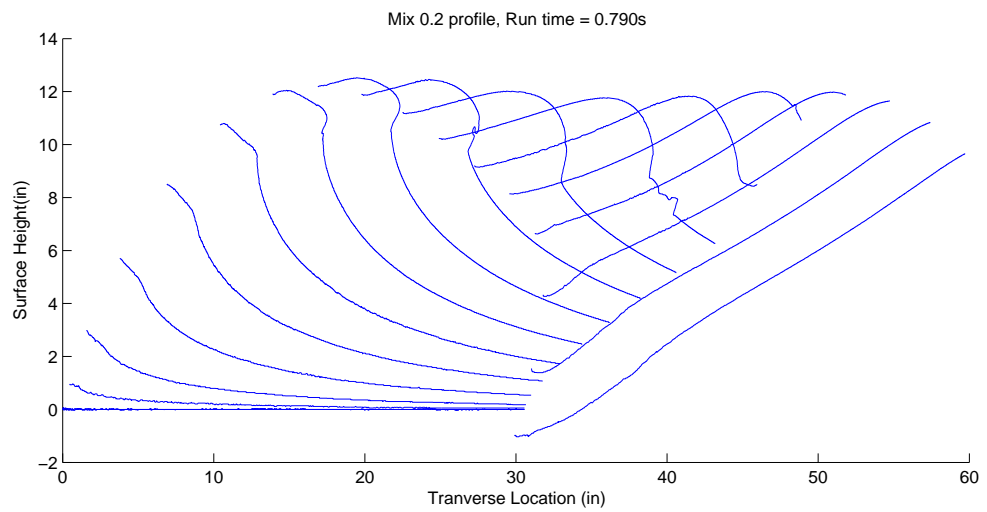
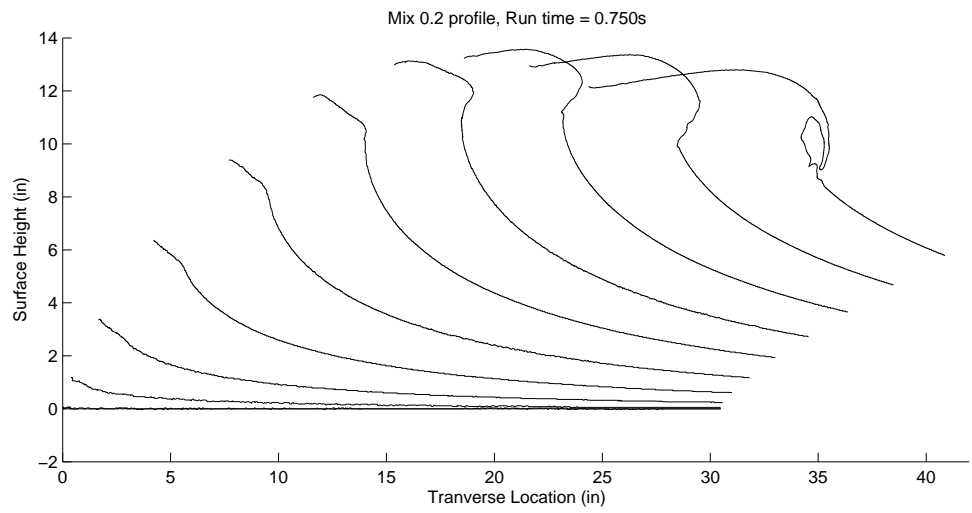
Wave Profiles

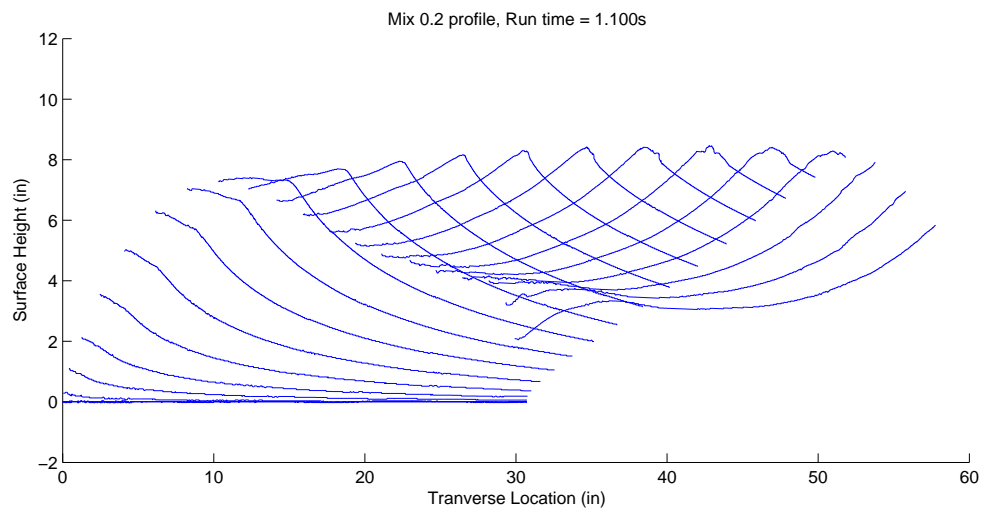
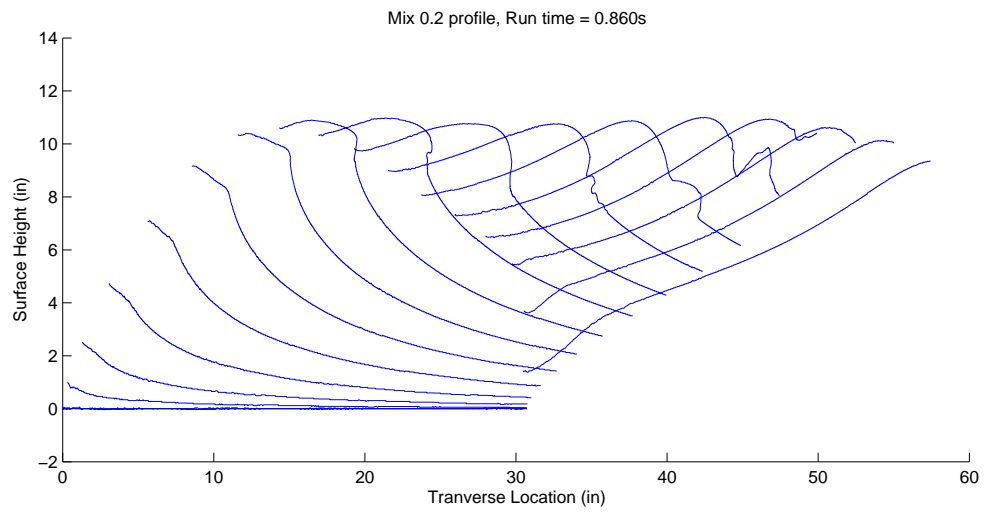
C.1 All Profiles

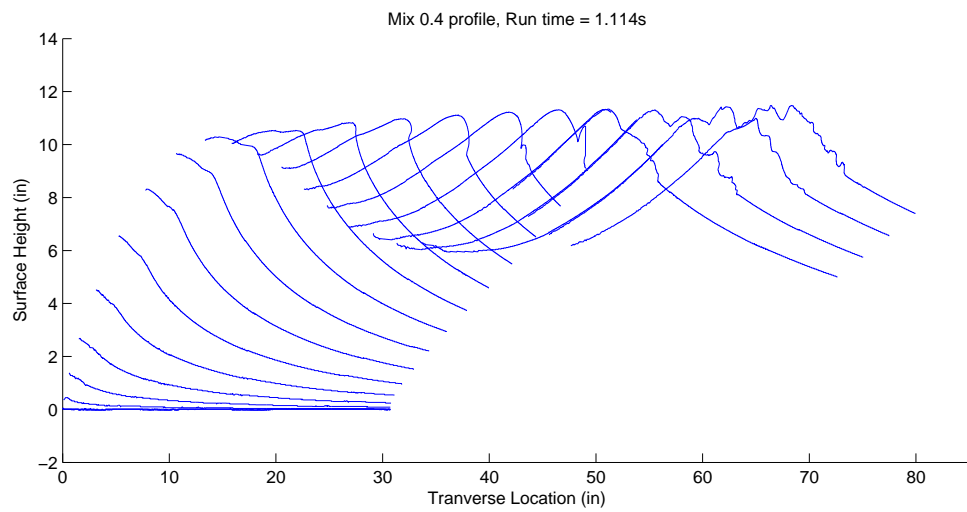
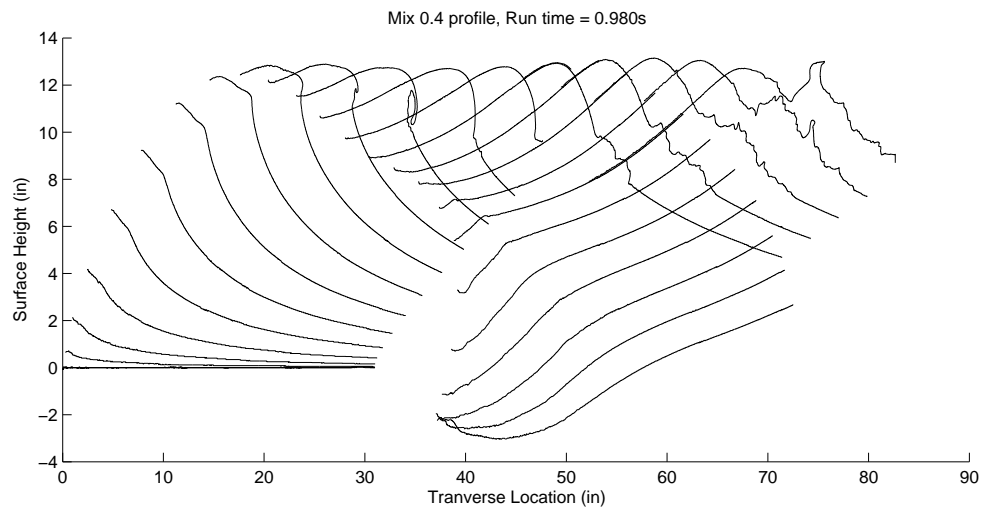


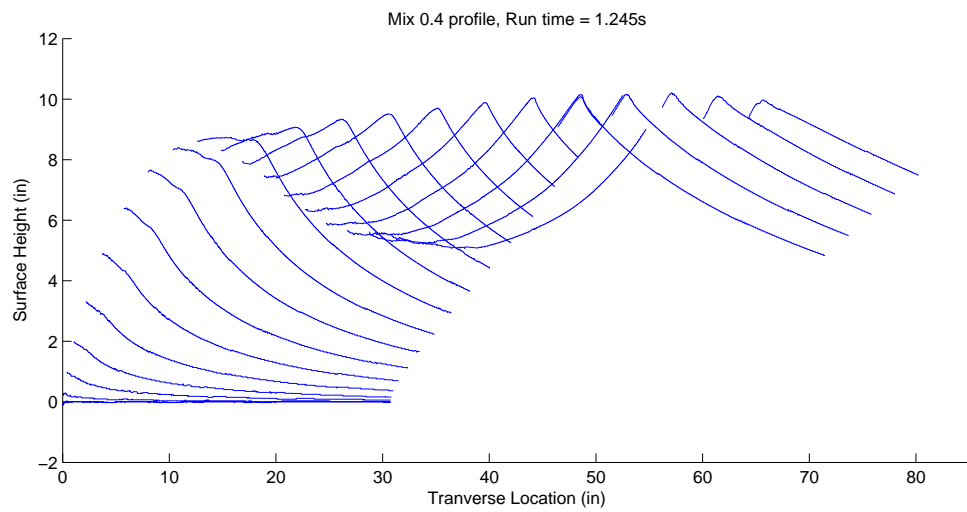
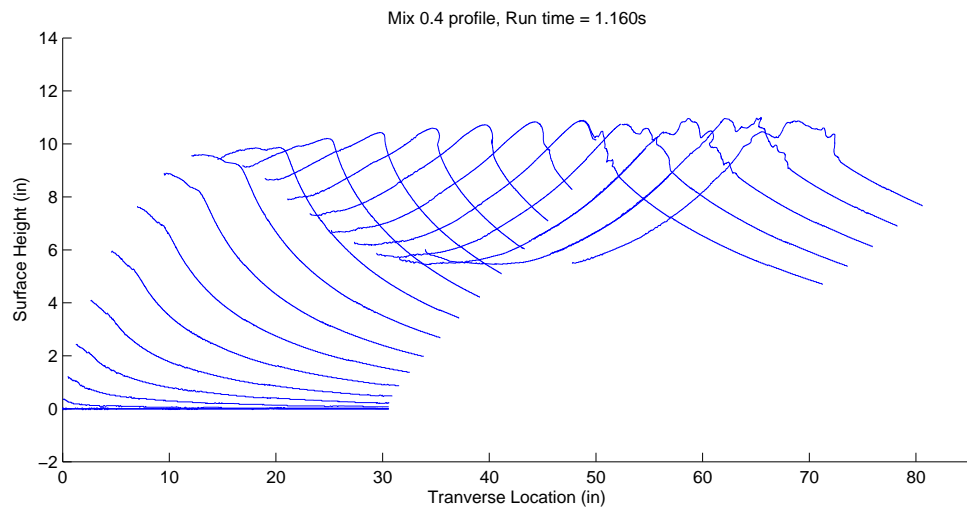


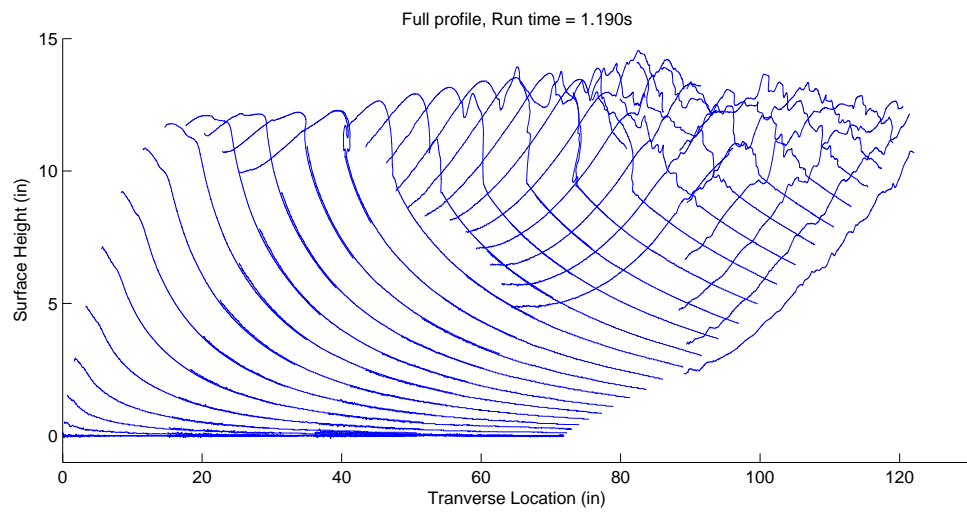
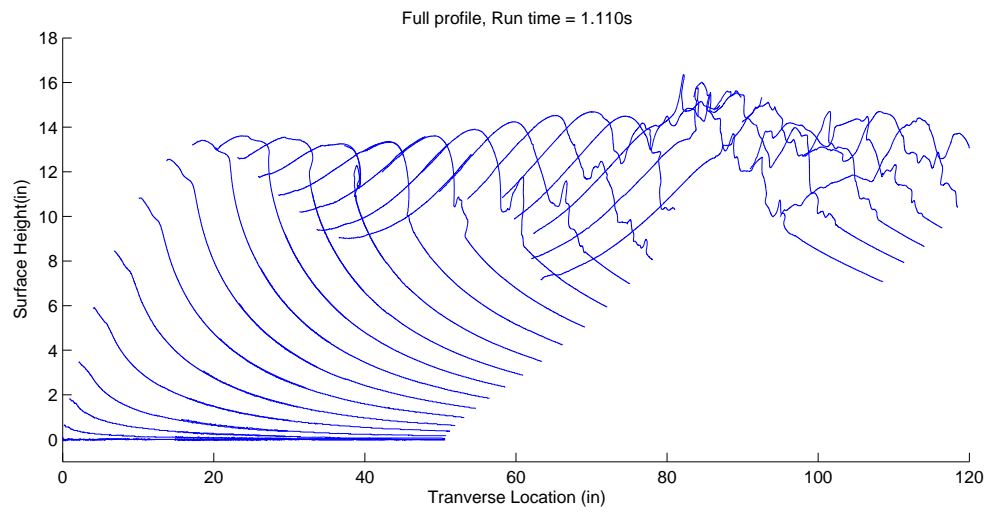


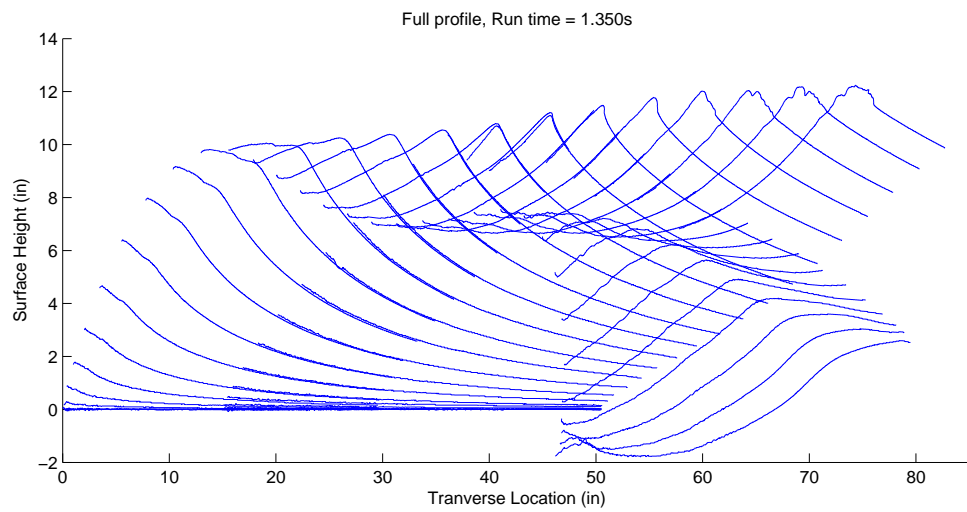
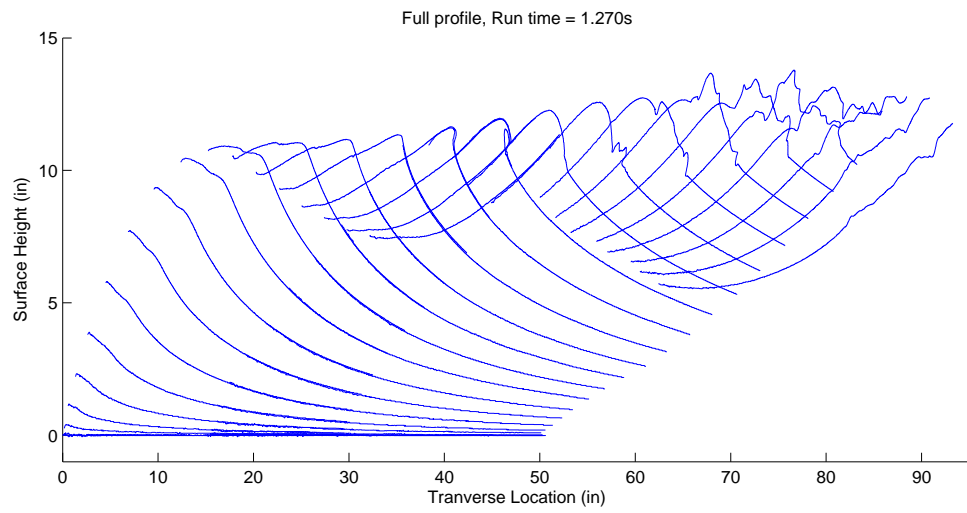


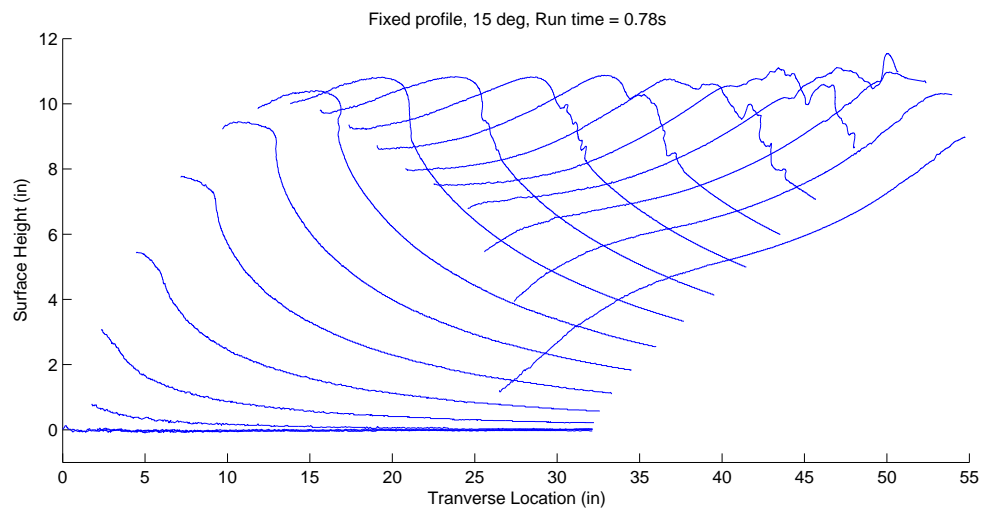
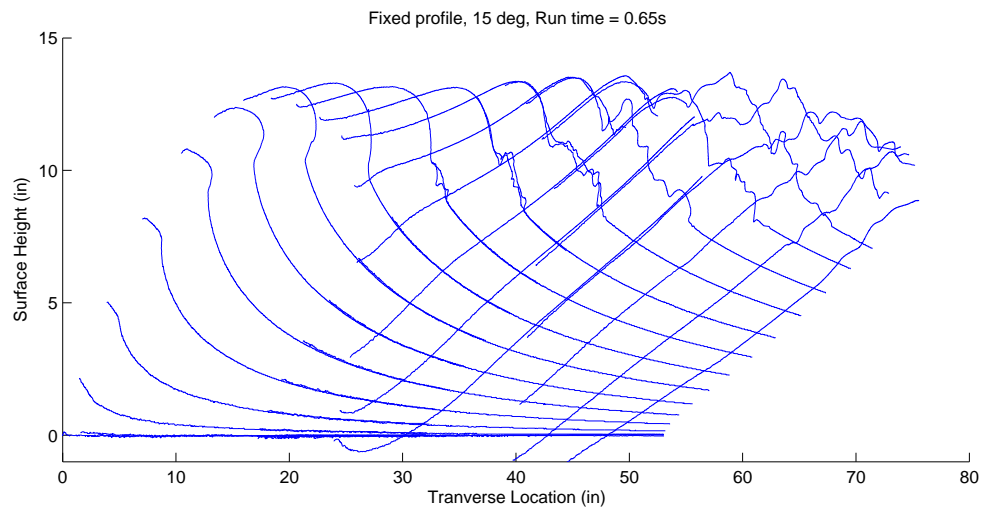


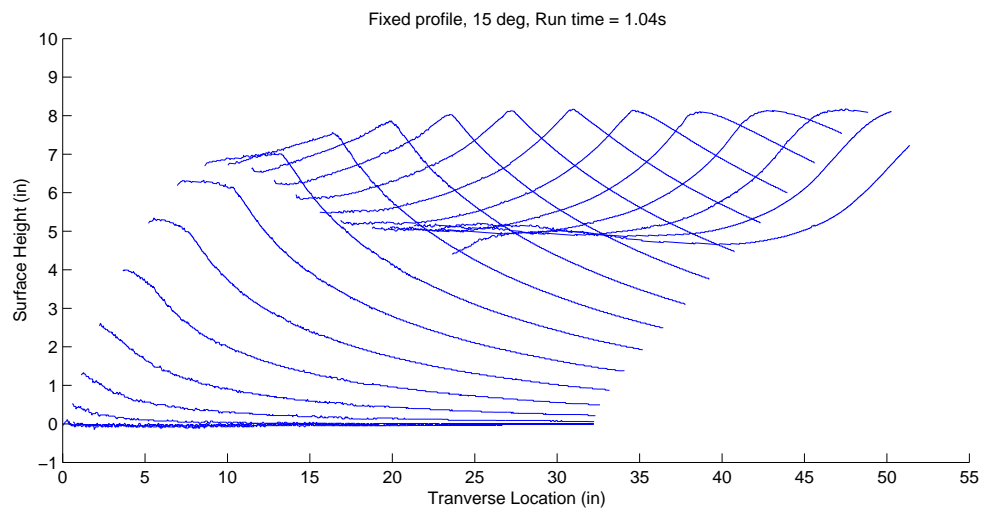
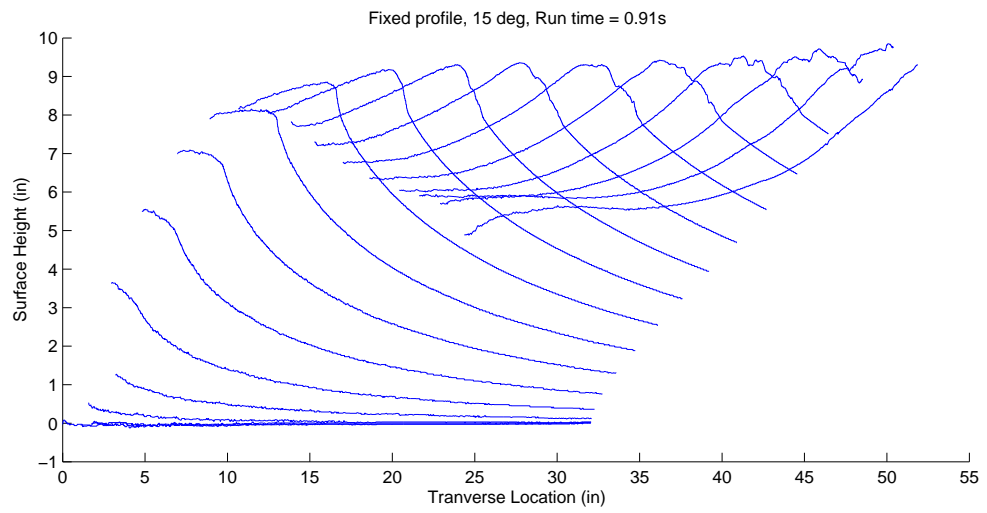


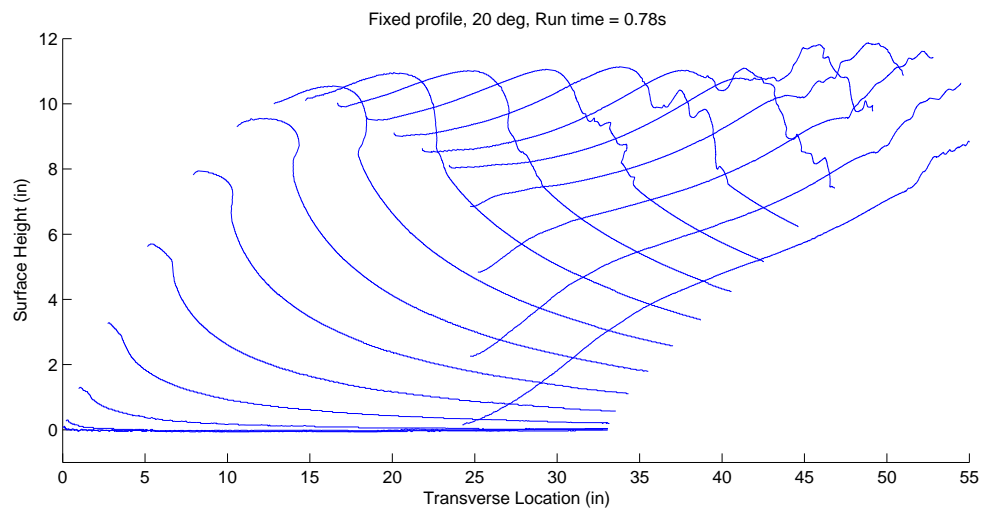
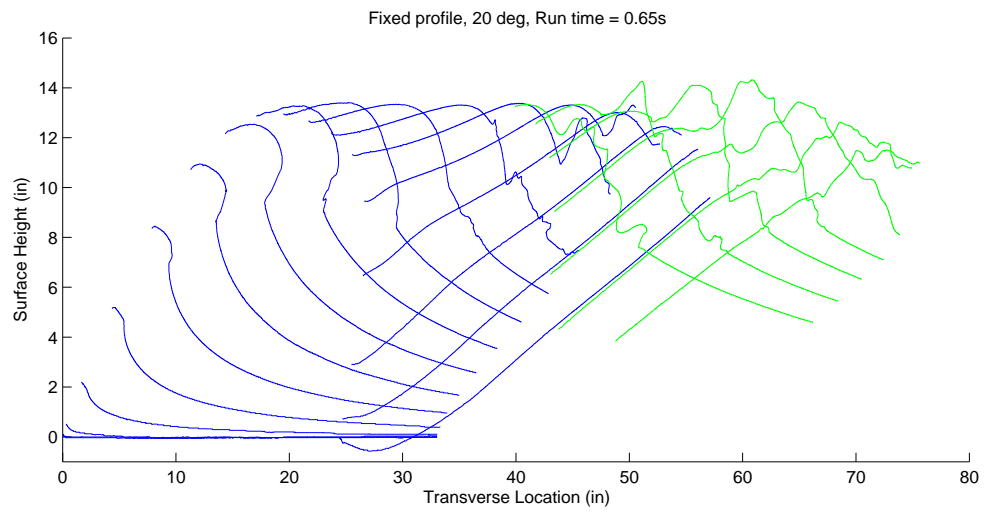


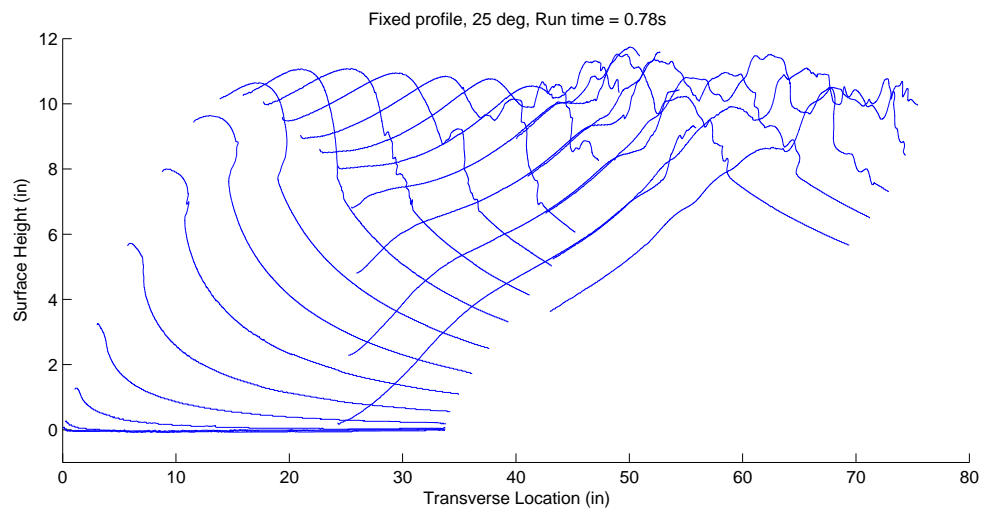
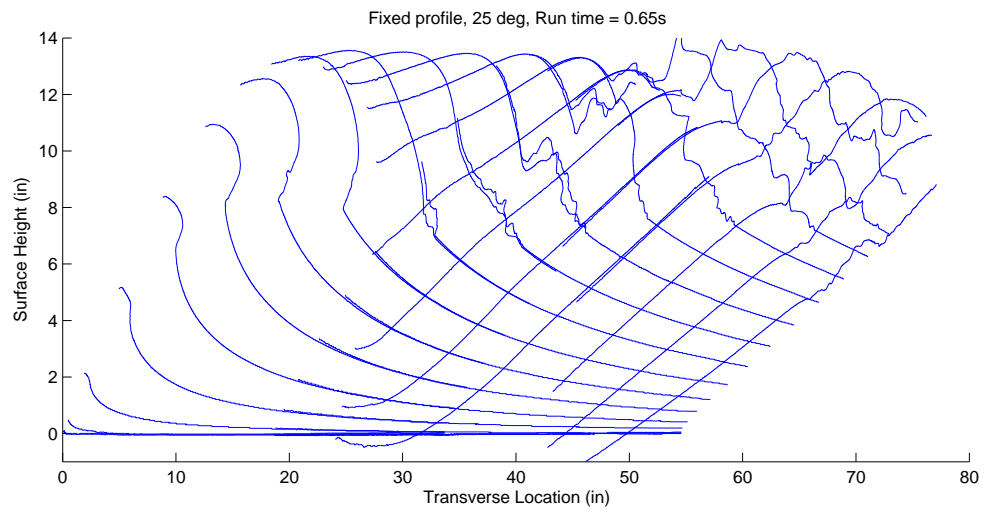


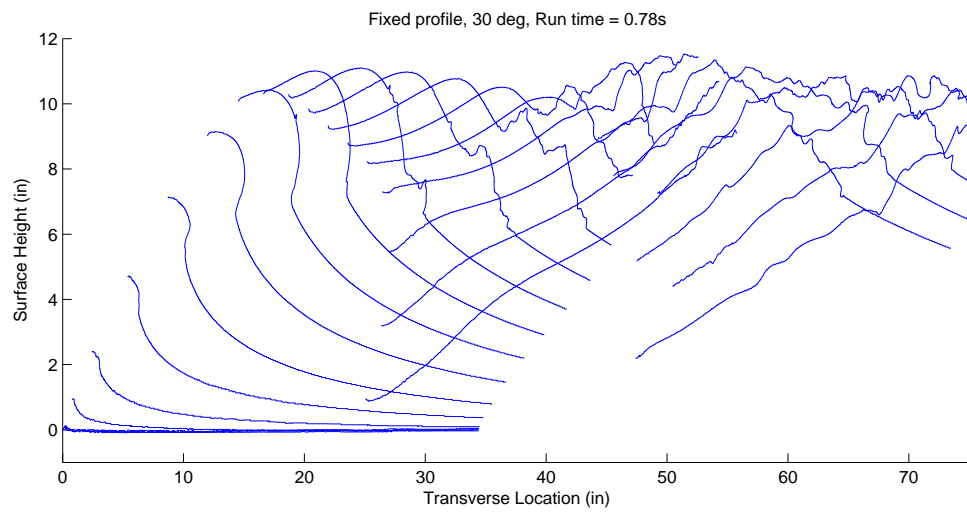
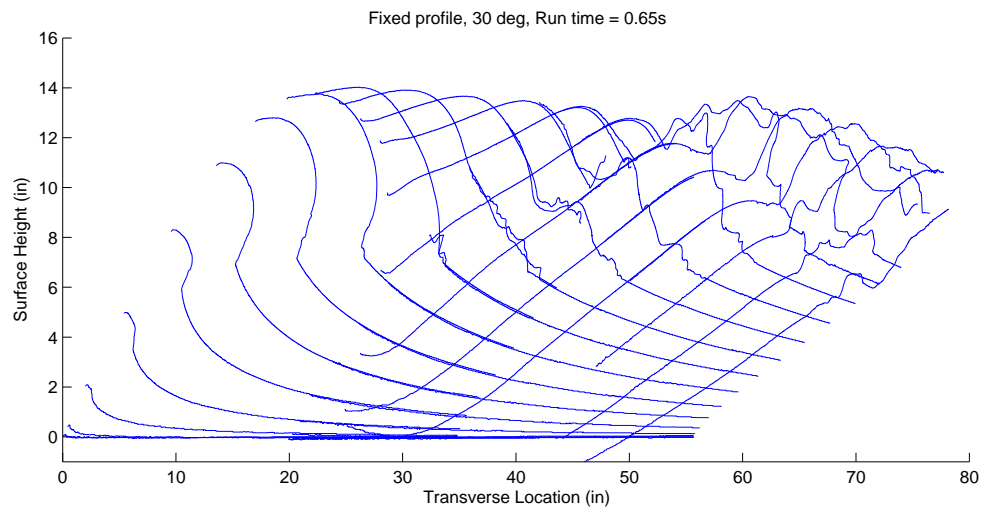


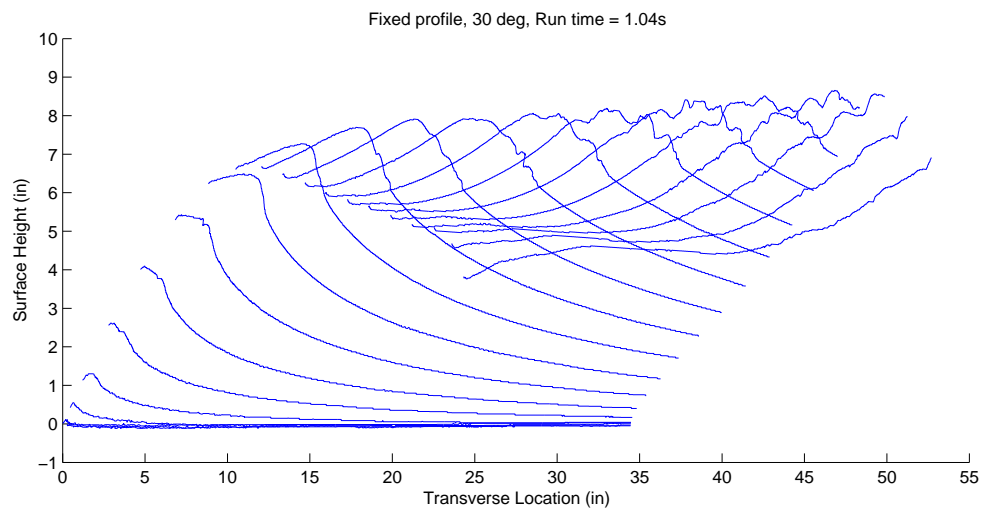
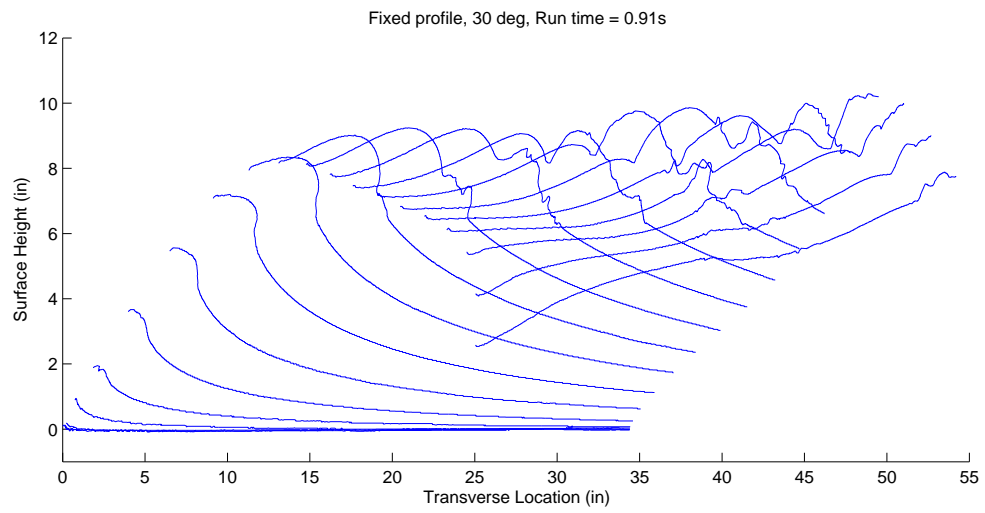












Appendix D

Fixed Case Comparison

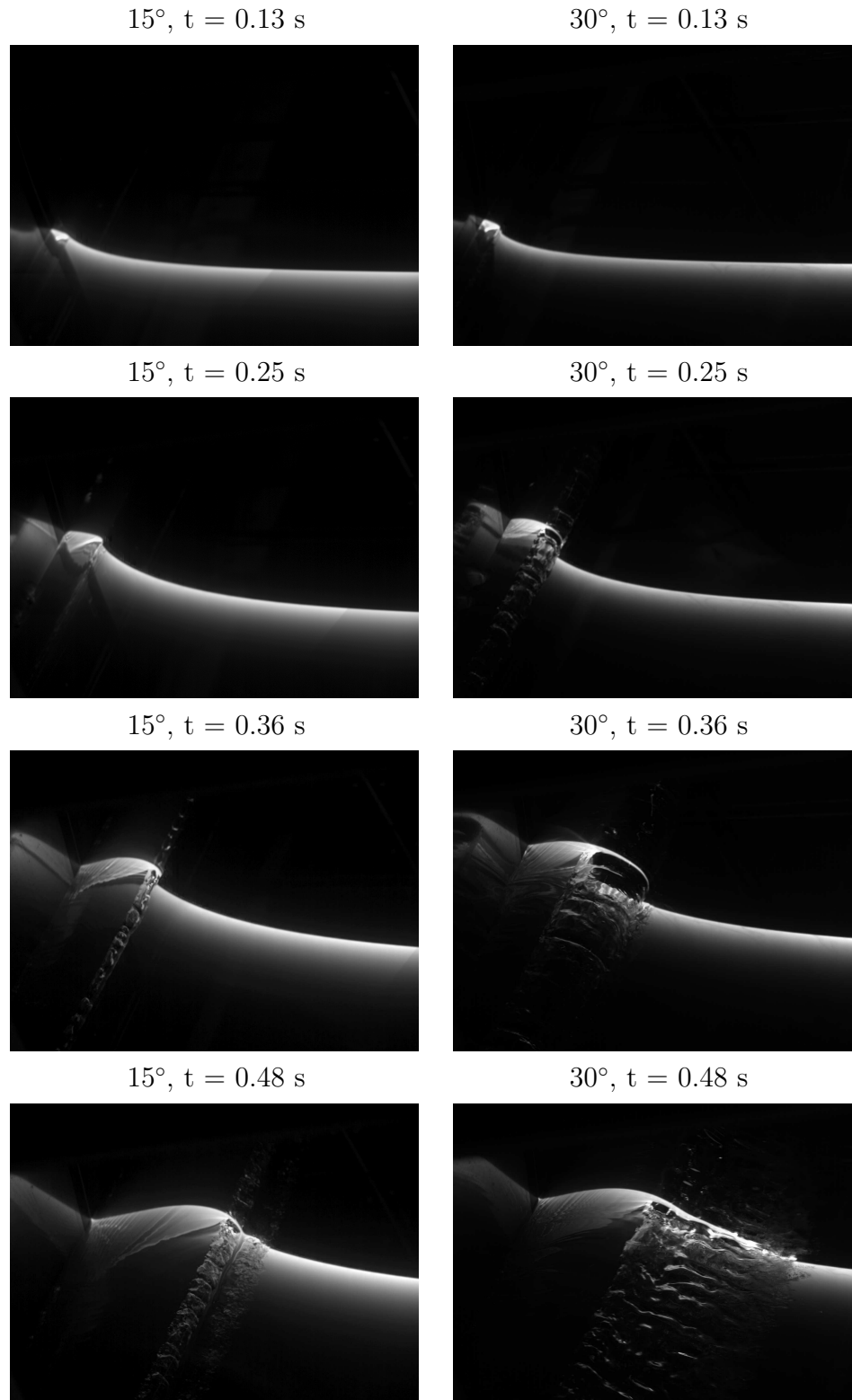


Figure D.1: Comparison of Fixed cases at different angles of attack. Both cases tested at $V_b = 0.94$ m/s ($t_{wm} = 0.65$ s).

Bibliography

- [1] Battjes, J. A. and T. Sakai, 1981, Velocity field in a steady breaker, *Journal of Fluid Mechanics*, **111**: 421-437.
- [2] Bonmarin, P., 1989, Geometric properties of deep-water breaking waves, *Journal of Fluid Mechanics*, **209**: 405-433.
- [3] Chan, R. K. and R. L. Street, 1970, A numerical model for water waves, Technical Report, Department of Civil Engineering, Stanford University, 135.
- [4] Crapper, G. D. 1957 An exact solution for progressive capillary waves of arbitrary amplitude, *Journal of Fluid Mechanics*, **2**: 532-540.
- [5] Cointe, R. and M. P. Tulin, 1994, A theory of steady breakers, *Journal of Fluid Mechanics*, **276**: 1-20.
- [6] Delhommeau, G., F. Noblesse, H. Y. Kim and C. Yang, 2009, Bow waves of a family of fine ruled ship hulls with rake and flare, *Journal of Ship Research*, in review.
- [7] Dias, F. and E. O. Tuck, 1993, A steady breaking wave, *Physics of Fluids*, **5**(1): 1993.
- [8] Dommermuth, D. G., D. K. P. Yue, R. H. Rapp, E. S. Chen and M. K. Melville, 1988, Deep-water breaking waves: a comparison between potential theory and experiments, *Journal of Fluid Mechanics*, **89**: 432-442.
- [9] Dong, R. R., J. Katz, T. T. Huang, 1997, On the structure of bow waves on a ship model, *Journal of Fluid Mechanics*, **346**: 77-115.
- [10] Duncan, J. H., 1981, An experimental investigation of breaking waves produced by a towed hydrofoil, *Proceedings of the Royal Society of London, Series A*, **377**: 331-348.
- [11] Duncan, J. H., 1983, The breaking and nonbreaking resistance of a twodimensional hydrofoil, *Journal of Fluid Mechanics*, **126**: 507-520.
- [12] Duncan, J. H., H. Qiao, H. Behres and J. Kimmel, 1994, The formation of a spilling breaker, *Physics of Fluids*, **6** (8): 2558-2560.
- [13] Duncan, J. H., H. Qiao, V. Philomin and A. Wenz, 1999, Gentle spilling breakers: crest profile evolution, *Journal of Fluid Mechanics*, **379**: 191-222.
- [14] Duncan, J. H., 2001, Spilling Breakers, *Annual Review of Fluid Mechanics*, **33**: 519-547.

- [15] Huang, J. C. P., 1970, The break-up of axisymmetric liquid sheets, *Journal of Fluid Mechanics*, **43**: 305-319.
- [16] Inui, T., 1981, From bulbous bow to free-surface shock wave - trends of 20 years' research on ship waves at the Tokyo University Tank, *Journal of Ship Research*, **25**(3): 147-180.
- [17] Jenkins, A. D., 1994, A stationary potential-flow approximation for a breaking wave crest, *Journal of Fluid Mechanics*, **280**: 335-347.
- [18] King, A. C. and D. J. Needham, 1994, The initial development of a jet caused by fluid, body and free-surface interaction. Part 1. A uniformly accelerating plate, *Journal of Fluid Mechanics*, **268**: 89-101.
- [19] Lamb, H., 1932, *Hydrodynamics*, Dover Publications, New York, USA.
- [20] Larsson, L. and E. Baba, 1996, Ship resistance and flow computations, *Advances in Marine Hydrodynamics*, Edited by M. Ohkusu, p. 1-75.
- [21] Lin, J. C. and D. Rockwell, 1994, Instantaneous structure of a breaking waves, *Physics of Fluids*, **6**(9): 2877-2879.
- [22] Lin, S. P., 2003, *Breakup of Liquid Sheets and Jets*, Cambridge University Press, Cambridge, UK.
- [23] Lin, J. C. and D. Rockwell, 1995, Evolution of a quasi-steady breaking waves, *Journal of Fluid Mechanics*, **302**: 29-44.
- [24] Liu, X. and J. H. Duncan, 2006, An experimental study of surfactant effects on spilling breakers, *Journal of Fluid Mechanics*, **567**: 1-23.
- [25] Longuet-Higgins M. S. and E. D. Cokelet, 1976, The deformation of steep surface waves on water. I. A numerical method of computation. *Proceedings of the Royal Society of London, Series A*, **358**: 157-184.
- [26] Longuet-Higgins, M. S., 1995, On the disintegration of the jet in a plunging breaker, *Journal of Physical Oceanography*, **25**: 2458-2462
- [27] De Luca, L. and M. Costa, 1997, Instability of a spatially developing liquid sheet, *Journal of Fluid Mechanics*, **331**: 127-144.
- [28] Michell, J. H., 1898, The wave resistance of a ship, *Phil. Mag.*, **45**(5): 106-123.
- [29] Miller, R. L., 1976, Foles of vortices in surf zone prediction: sedimentation and wave forces. In *Beach and Nearshore Sedimentation* (ed.. R. A. Davis and R. I. Ethington), 92-114, Soc. Econ. Paleontologists and Mineralogists Spec. Publ. **24**.
- [30] Miyata, H. and T. Inui, 1984, *Nonlinear ship waves*, *Advances in Applied Mechanics*, **24**: 215-288.

- [31] New, A. L., A class of elliptical free-surface flows, *Journal of Fluid Mechanics*, **130**: 219-239.
- [32] New, A. L., P. McIver and D. H. Peregrine, 1985, computations of overturning waves, *Journal of Fluid Mechanics*, **150**: 233-251.
- [33] Noblesse, F., D. Hendrix, L. Faul and J. Slutsky, 2006, Simple analytical expressions for the height, location and steepness of a ship bow wave, *Journal of Ship Research*, **50**(4): 360-370.
- [34] Noblesse, F., G. Delhommeau, M. Guilbaud, D. Hendrix, L. Faul and C. Yang, 2008, Simple analytical relations for ship bow waves, *Journal of Fluid Mechanics*, **600**: 105-132.
- [35] Peltzer, R., 1984, White-water wake characteristics of surface vessels. NRL Memorandum Report 5335. Naval Research Laboratory, Washington, DC, June.
- [36] Peregrine, D. H. and I. A. Svendsen, 1978, Spilling breakers, bores, and hydraulic jumps, 16th International Conference on Coastal Engineering, Hamburg, New York, Aug. 27-Sep. **3**, pp. 540-550.
- [37] Roth, G. L., D. T. Mascenik and J. Katz, 1999, Measurements of the flow structure and turbulence within a ship bow wave, *Physics of Fluids*, **11**(11): 3512-3523.
- [38] Shakeri, M., 2005, An experimental 2D+T investigation of breaking bow waves, PhD Dissertation, Department of Mechanical Engineering, University of Maryland.
- [39] Shakeri, M., Mayer, M., Tavakolinejad, M., and J. H. Duncan, 2006, Characteristics of Breaking Bow Waves Generated by a 2D+T Wave Maker, Proceedings of FEDSM 2006 (Paper No. FEDSM2006-98534), ASME Joint U.S.-European Fluids Engineering Summer Meeting, July 17-20, Miami, FL.
- [40] Shakeri, M., Tavakolinejad, M., and J. H. Duncan, 2009, An experimental examination of divergent bow waves, *Journal of Fluid Mechanics*, in press.
- [41] Shakeri, M., E. Maxeiner, T. Fu and J. H. Duncan, 2009, An experimental examination of the 2D+T approximation, *Journal of Ship Research*, in press.
- [42] Skyner, D. J., C. Gray, and C. A. Greated, 1990, A comparison of time-stepping numerical predictions with whole-field flow measurement in breaking waves. *Water Wave Kinematics*, edited by A. Torum and O. T. Gudmestad, pp. 491-508.
- [43] Stokes, G. G., 1847, On the theory of oscillatory waves, *Trans. of the Cambridge Philosophical Society*, **8**: 441.

- [44] Taylor, G. I., 1959, The dynamics of thin sheets of fluid II. Waves on fluid sheets, *Proc. Royal Society of London* **A253**: 296-312.
- [45] Thomson, W. (Lord Kelvin), 1887, On the waves produced by a single impulse in water of any depth, or in a dispersive medium, *Proceedings of the Royal Society*, xlii. **80**.
- [46] Tulin, M. and M. Wu, 1997, Divergent Bow Waves, *Proceedings of the 21st Symposium on Naval Hydrodynamics*, Trondheim, Norway, 661-679.
- [47] Waniewski, T., C. Brennan, and F. Raichlen, 1997, Experimental simulation of a bow wave, *Proceedings of FEDSM 2007, ASME Joint U.S.-European Fluids Engineering Summer Meeting*, June 22-26, 2006.
- [48] Waniewski, T., C. Brennan, and F. Raichlen, 2001, Measurements of air entrainment by bow waves, *Journal of Fluids Engineering*, **123**: 57-63.
- [49] Waniewski, T., C. Brennan, and F. Raichlen, 2002, Bow wave dynamics, *Journal of Ship Research*, **46**(1): 1-15.
- [50] Wehausen, J. V., 1973, The wave resistance of ships, *Advances in Applied Mechanics*, Vol 13, Academic Press Inc., p. 93-245.